

---

Wayne State University Dissertations

---

January 2022

## Study Of The Decay $B^{\pm} \rightarrow K^0_s \pi^{\pm} \pi^0$ At The Belle Experiment

Suravinda Janaka Kumara Kospalage  
*Wayne State University*

Follow this and additional works at: [https://digitalcommons.wayne.edu/oa\\_dissertations](https://digitalcommons.wayne.edu/oa_dissertations)

 Part of the [Elementary Particles and Fields and String Theory Commons](#)

---

### Recommended Citation

Kospalage, Suravinda Janaka Kumara, "Study Of The Decay  $B^{\pm} \rightarrow K^0_s \pi^{\pm} \pi^0$  At The Belle Experiment" (2022). *Wayne State University Dissertations*. 3598.  
[https://digitalcommons.wayne.edu/oa\\_dissertations/3598](https://digitalcommons.wayne.edu/oa_dissertations/3598)

This Open Access Dissertation is brought to you for free and open access by DigitalCommons@WayneState. It has been accepted for inclusion in Wayne State University Dissertations by an authorized administrator of DigitalCommons@WayneState.

**STUDY OF THE DECAY  $B^\pm \rightarrow K_S^0 \pi^\pm \pi^0$  AT THE BELLE EXPERIMENT**

by

**SURAVINDA JANAKA KUMARA KOSPALAGE**

**DISSERTATION**

Submitted to the Graduate School

of Wayne State University,

Detroit, Michigan

in partial fulfillment of the requirements

for the degree of

**DOCTOR OF PHILOSOPHY**

2022

MAJOR: PHYSICS

Approved By:

---

Advisor

Date

---

---

---

---

## DEDICATION

*To Vimuththa Arahath Therani and my loving Parents, for their unconditional love and support*

## ACKNOWLEDGMENT

Firstly, I would like to thank my adviser, Prof. David Cinabro, for constant guidance throughout the academic years. Thanks for providing me with the opportunity and freedom to explore and work on challenging projects. Without your support, this would not be possible. I would also like to give special thanks to Dr. Matthew Barrett for unconditional support and teaching programming languages, Sub-detector related maintenance, control room works and guidance for this project.

I would also like to express my sincere gratitude to my committee members Prof. Giovanni Bonvicini, Prof. Robert Harr and, Prof. Loren Schwiebert, for their support during my research. I would also like to thank other faculty members at Wayne State University, Prof. Joern Putschke for teaching the Computational Physics course covering basic C++ and ROOT programming. Prof. Alexey Petrov and Prof. Gil Paz for teaching quantum mechanics and fundamentals of the quantum field theory. Prof Ashis Mukhopadhyay for thermodynamics. Prof Giovanni Bonvicini for electromagnetism.

Thanks to everyone, I met at Wayne State University. To Amit Kumar, Ayesh and Suneth for their support both inside and outside the workplace. To all Srilankan Wayne State community friends for making life in Michigan smooth and enjoyable.

Finally, a big thank you to my family members. To my parents and brother, for their constant unconditional support and special thank goes to Vimuththa Arahath Therani for teaching me what is the science beyond the science.

# TABLE OF CONTENTS

<b>Dedication</b>	<b>ii</b>
<b>Acknowledgments</b>	<b>iii</b>
<b>List of Figures</b>	<b>vii</b>
<b>List of Tables</b>	<b>xi</b>
<b>1 Introduction</b>	<b>1</b>
1.1 The Standard Model	1
1.2 The $C$ , $P$ , and $T$ Symmetries	4
1.3 B Meson	5
1.4 CP Violation	6
1.4.1 Direct CP Violation	7
1.4.2 CP Violation in Mixing	8
1.4.3 CP violation in interference between direct and mixing	10
1.5 CKM Matrix	10
1.6 The Unitary Triangle	12
1.7 Weak phase and Strong Phase	15
1.8 Tree and Penguin diagrams for Charmless Decays	16
1.9 Dalitz analysis	17
1.10 Overview of this Thesis	18
<b>2 Belle Experiment</b>	<b>19</b>
2.1 KEKB Accelerator	19
2.2 Belle Detector	21
2.2.1 Beam Pipe	22
2.2.2 Silicon Vertex Detector (SVD)	23

2.2.3	Central Drift Chamber (CDC)	24
2.2.4	Aerogel Cherenkov Counter (ACC)	27
2.2.5	Time Of Flight counter (TOF)	29
2.2.6	Electromagnetic Calorimeter (ECL)	31
2.2.7	Belle Superconducting Magnet	32
2.2.8	K-Long and Muon Detector (KLM)	34
2.3	Belle Trigger and Data Acquisition System (DAQ)	36
2.4	Belle Analysis Software Framework (BASF) and Monte Carlo (MC)	38
<b>3</b>	<b>Analysis</b>	<b>40</b>
3.1	Particle Identification and Event Reconstruction	40
3.1.1	Data sample	40
3.1.2	Monte Carlo Simulation	43
3.1.3	Data and MC Reconstruction	43
3.1.4	Continuum and B related Backgrounds	44
3.2	Selection Criteria	45
3.2.1	Initial Event Selection	45
3.2.2	Continuum Suppression and Multi Variate Analysis (MVA)	49
3.2.3	Boosted Decision Trees (BDT)	50
3.3	Full MC and Data driven Background estimation	53
3.4	Dalitz analysis using Laura++	59
3.4.1	Kinematics of three body decays	59
3.4.2	Kinematic boundaries of a Dalitz plot	61
3.4.3	Introduction to Laura++	63
3.5	Dalitz plot Efficiency and Self cross feed	65
3.5.1	Efficiency	65
3.5.2	Self Cross Feed (SCF)	67
3.6	Fitting	68

3.6.1	Resonance model . . . . .	68
3.6.2	Background distributions in the DP . . . . .	70
<b>4</b>	<b>Results . . . . .</b>	<b>74</b>
4.1	Performance of selection criteria on Full MC and Data . . . . .	74
4.2	Results of Data driven background estimation . . . . .	79
4.2.1	Background and Error estimation . . . . .	79
4.3	Branching Fraction determination and error calculation . . . . .	81
4.4	Full MC Dalitz plot study . . . . .	85
4.4.1	Determination of resonance model . . . . .	85
4.4.2	Amplitude, Phase, FitFraction and Error study . . . . .	88
<b>5</b>	<b>Summary and Conclusion . . . . .</b>	<b>94</b>
5.1	Summary of Results . . . . .	94
5.2	Comparison of Results with BaBar and PDG . . . . .	96
5.3	Conclusion and Discussion . . . . .	97
5.4	Future analysis . . . . .	98
5.5	Super KEKB and Belle II detector . . . . .	99
	<b>Bibliography . . . . .</b>	<b>101</b>
	<b>Abstract . . . . .</b>	<b>106</b>
	<b>Autobiographical Statement . . . . .</b>	<b>108</b>

## LIST OF FIGURES

Figure 1.1	Particles of the Standard Model [1]. . . . .	2
Figure 1.2	The unitarity triangle representation in the complex plane [2]. Both Belle and Belle II use $\phi_1 \equiv \beta$ , $\phi_2 \equiv \alpha$ , $\phi_3 \equiv \gamma$ . . . . .	13
Figure 1.3	Constraints on the unitarity triangle from the CKM fitter collaboration [3].	14
Figure 1.4	Left side is a tree and the right side is a penguin diagram [4]. . . . .	16
Figure 1.5	Uniformly distributed Dalitz plot [5]. . . . .	17
Figure 2.1	Schematic diagram of the KEKB accelerator [6]. . . . .	20
Figure 2.2	Schematic diagram of the Belle detector [7]. . . . .	21
Figure 2.3	Cross section of the Belle detector [7]. . . . .	22
Figure 2.4	Schematic diagram of the Belle beam pipe [8]. . . . .	23
Figure 2.5	Schematic diagram of Belle SVD1 [8]. . . . .	24
Figure 2.6	Schematic diagram of Belle SVD2 [8]. . . . .	24
Figure 2.7	CDC structure [8]. . . . .	25
Figure 2.8	Rate of energy loss Vs Momentum of charged particles [8]. . . . .	27
Figure 2.9	Configuration of ACC Barrel [9]. . . . .	28
Figure 2.10	Left side Barrel ACC module configuration and Right side Endcap module configuration [9]. . . . .	29
Figure 2.11	Dimensions of TOF and TSC module [8]. . . . .	30
Figure 2.12	The separation of kaon and pions for momentum less than 1.2 $GeV/c$ . Black points represent data and histogram represent MC prediction [10].	31
Figure 2.13	Configuration of ECL [8]. . . . .	32
Figure 2.14	The Belle solenoid magnet and the cross-sectional view of the coil [10]. . .	33

Figure 2.15	Cross-sectional view of KLM detector layers [8]. . . . .	35
Figure 2.16	Belle trigger system from [8]. . . . .	37
Figure 2.17	Belle data acquisition system [10]. . . . .	38
Figure 3.1	Background(Left) and Signal(Right) candidate distributions. . . . .	47
Figure 3.2	Background rejection vs. signal efficiency generated by TMVA for several MVA methods.. . . .	50
Figure 3.3	Example of a decision tree. . . . .	51
Figure 3.4	The left histogram shows the BDT variable for 1000 events of signal and $u\bar{u}$ background samples. The right plot shows BDT cut optimization for expected signal and background events. . . . .	52
Figure 3.5	Full MC: (A) $\Delta E$ vs $M_{BC}$ distribution without $M_{BC}$ and $\Delta E$ selection. (B) 1D projection of $M_{BC}$ distribution without $M_{BC}$ and $\Delta E$ selection. (C) $\Delta E$ vs $M_{BC}$ distribution with $M_{BC}$ and $\Delta E$ Selection. (D) 1D projection of $M_{BC}$ distribution with $M_{BC}$ and $\Delta E$ selection. . . . .	54
Figure 3.6	Unlike Figure 3.5 B, this figure includes the $\Delta E$ cut. . . . .	54
Figure 3.7	Method 1: $M_{BC}$ distribution Fit with ARGUS function . . . . .	55
Figure 3.8	Method 2: $M_{BC}$ distribution Fit with ARGUS and double GAUSSIAN function. . . . .	56
Figure 3.9	Method 3: $M_{BC}$ distribution fit with ARGUS function and combination of ARGUS and double GAUSSIAN function . . . . .	57
Figure 3.10	Signal + SCF $M_{BC}$ events distribution tail in the background region . . .	57
Figure 3.11	Method 4: $M_{BC}$ distribution Fit with two ARGUS functions . . . . .	58
Figure 3.12	Feynman diagrams contributing to $B^\pm \rightarrow K_s^0 \pi^\pm \pi^0$ . (A) and (C) are penguin level diagrams and (B) is tree level diagram . . . . .	59
Figure 3.13	Three Body decay of parent particle to daughter particles [11]. . . . .	60
Figure 3.14	Simulated Dalitz plot for $B^\pm \rightarrow K_s^0 \pi^\pm \pi^0$ with intermediate resonances. .	61
Figure 3.15	Dalitz plot boundaries [11] . . . . .	62

Figure 3.16	Dalitz efficiency plot for 40 by 40 bin size . . . . .	66
Figure 3.17	Dalitz efficiency plot for 200 by 200 bin size. Bin size is too small and plot is dominated by statistical fluctuation particularly near the edges of the plot . . . . .	66
Figure 3.18	Dalitz efficiency plot for 5 by 5 bin size. Bin size is too large and plot does not show enough details . . . . .	67
Figure 3.19	Dalitz SCF plot for 40 by 40 bin size. . . . .	68
Figure 3.20	Dalitz Plot distribution of full MC before (left) and after (right) selection criteria are applied. . . . .	69
Figure 3.21	Invariant mass distribution of $K_S^0\pi^\pm$ (top left), $K_S^0\pi^0$ (top right), and $\pi^\pm\pi^0$ (bottom). . . . .	70
Figure 3.22	Continuum background distribution before and after selection criteria (top left and right plots), B-related background distribution before and after selection criteria (bottom left and right plots). . . . .	71
Figure 3.23	SCF distribution before selection criteria (left) and after selection criteria (right). . . . .	72
Figure 3.24	Signal Dalitz plot combined with continuum, B-related and SCF event distributions . . . . .	72
Figure 4.1	Signal, Continuum and, B-related events distribution in the $M_{BC}$ and $\Delta E$ variables before selections . . . . .	74
Figure 4.2	Signal, continuum and, B-related events $K_S^0\pi^0$ mass distribution before and after the BDT selection. . . . .	75
Figure 4.3	DATA : (A) $\Delta E$ Vs $M_{BC}$ distribution without $M_{BC}$ and $\Delta E$ Selection. (B) 1D projection of $M_{BC}$ distribution without $M_{BC}$ and $\Delta E$ selection. (C) $\Delta E$ Vs $M_{BC}$ distribution with $M_{BC}$ and $\Delta E$ Selection. (D) 1D projection of $M_{BC}$ distribution with $M_{BC}$ and $\Delta E$ selection. . . . .	77
Figure 4.4	Distribution of the number of estimated background events in data after fit using method 4. . . . .	81
Figure 4.5	$M_{BC}$ distribution of data without $M_{BC}$ selection. . . . .	84

Figure 4.6 Number of good, from 3 to 4, and bad, from 1 to 2, fits after 1000 fits in Laura++ . . . . . 86

Figure 4.7 (A) shows NLL distribution and (B) shows after accept good fits. . . . . 87

Figure 4.8 NLL distribution with include/exclude resonances . Excluded resonances shows higher NLL values than included in (C) and (D). Extra included resonances in (B) does not make much difference compare to (A) . . . . . 88

Figure 4.9 NLL distribution with different resonance contributions. . . . . 89

Figure 4.10 Square fit fraction distribution generated by using upper and lower limits of amplitude and phase parameters for  $\rho^+(770)$ . . . . . 91

Figure 4.11 Stack plots of generated toy MC mass distribution compared with the full MC. . . . . 92

Figure 5.1 Belle II detector with new sub detectors [12] . . . . . 100

## LIST OF TABLES

Table 1.1	The Fundamental gauge bosons . . . . .	3
Table 1.2	B meson family [1]. . . . .	6
Table 3.1	Summary of the luminosity and number of events in each experiment [13]	41
Table 3.2	MC stream 0 file Location sample for experiment 31 [13]. . . . .	42
Table 4.1	Summary of the full MC selection criteria corresponding to 571 $fb^{-1}$ of simulated luminosity. . . . .	76
Table 4.2	Number of events after each selection criteria for signal, charged, mixed, charm and, $uds$ for 571 $fb^{-1}$ of luminosity in both full MC and data. . . .	78
Table 4.3	ARGUS function parameter values for full MC and data fit . . . . .	80
Table 4.4	Area under the curve and number of events for Full MC and DATA . . . .	81
Table 4.5	Branching fraction calculation values for full MC. . . . .	83
Table 4.6	Branching fraction calculation values for data . . . . .	84
Table 4.7	Summary of branching fraction for full MC and data . . . . .	85
Table 4.8	Fit parameter values after fitting full MC with Laura++. . . . .	90
Table 4.9	Branching fraction of each resonance contribution . . . . .	93
Table 5.1	Selection criteria summary of both full MC and data corresponding to 571 $fb^{-1}$ of luminosity. . . . .	94
Table 5.2	Summary of the number of events for full MC and data according to different fitting methods . . . . .	95
Table 5.3	Summary of branching fraction for full MC and data . . . . .	96
Table 5.4	Branching Fraction Comparison. . . . .	96
Table 5.5	Intermediate resonance comparison. . . . .	97

## CHAPTER 1 INTRODUCTION

### 1.1 The Standard Model

Our universe encompasses everything we see; nearly everything can be divided into smaller components. Studying the atom leads to the discovery of the nucleus [14], and further study of the nucleus leads to the observation of protons and neutrons. These can even be further divided into smaller particles called quarks, which as of today we consider to be elementary particles, i.e. are not made of smaller parts.

The electron is also a fundamental component of the atom and it belongs to a family called leptons which share similar properties with the electron. The Standard Model (SM) [1] is our best explanation describing the small scale behavior of the fundamental particles and forces. One of the important steps in building the SM was the discovery of sub-structure in the proton and neutron observed in the scattering of electrons off simple nuclei [14].

The SM is a model of the fundamental particles and the forces between them. It includes matter and anti-matter. Anti-Matter is the opposite of normal matter; more specifically, anti-matter particles have the same quantum numbers but with the opposite sign to those of normal matter. For example, the electric charge of particles and anti-particles are reversed. Anti-Matter was created along with matter after the Big Bang [15], but anti-matter is rare in today's universe.

The particles of the Standard Model are shown in Figure 1.1. They can be divided into two main groups called fermions, which are the "matter particles", and bosons, which are the force carriers [16]. Fermions are divided into two sub-groups called quarks and leptons. The main difference between quarks and leptons is that quarks interact with the strong nuclear force but leptons do not. These particles are the fundamental building blocks of matter in the universe. Each quark has a "color," the charge of the strong interaction. There are three colors, which are usually called RED, BLUE, and GREEN. Protons and Neutrons are combinations of these colored fermions, such as two UP (u) quarks and one DOWN (d) quark which build a proton. There have been no observations of free quarks [17], and we assume

quarks can only exist in bound states.

mass →	$\approx 2.3 \text{ MeV}/c^2$	$\approx 1.275 \text{ GeV}/c^2$	$\approx 173.07 \text{ GeV}/c^2$	0	$\approx 126 \text{ GeV}/c^2$
charge →	$2/3$	$2/3$	$2/3$	0	0
spin →	$1/2$	$1/2$	$1/2$	1	0
	<b>u</b> up	<b>c</b> charm	<b>t</b> top	<b>g</b> gluon	<b>H</b> Higgs boson
<b>QUARKS</b>	$\approx 4.8 \text{ MeV}/c^2$	$\approx 95 \text{ MeV}/c^2$	$\approx 4.18 \text{ GeV}/c^2$	0	
	$-1/3$	$-1/3$	$-1/3$	0	
	$1/2$	$1/2$	$1/2$	1	
	<b>d</b> down	<b>s</b> strange	<b>b</b> bottom	<b><math>\gamma</math></b> photon	
	$0.511 \text{ MeV}/c^2$	$105.7 \text{ MeV}/c^2$	$1.777 \text{ GeV}/c^2$	$91.2 \text{ GeV}/c^2$	
	-1	-1	-1	0	
	$1/2$	$1/2$	$1/2$	1	
	<b>e</b> electron	<b><math>\mu</math></b> muon	<b><math>\tau</math></b> tau	<b>Z</b> Z boson	
<b>LEPTONS</b>	$< 2.2 \text{ eV}/c^2$	$< 0.17 \text{ MeV}/c^2$	$< 15.5 \text{ MeV}/c^2$	$80.4 \text{ GeV}/c^2$	
	0	0	0	$\pm 1$	
	$1/2$	$1/2$	$1/2$	1	
	<b><math>\nu_e</math></b> electron neutrino	<b><math>\nu_\mu</math></b> muon neutrino	<b><math>\nu_\tau</math></b> tau neutrino	<b>W</b> W boson	
				<b>GAUGE BOSONS</b>	

Figure 1.1: Particles of the Standard Model [1].

We only observe composite particles that are “color neutral”. Baryons, such as the proton and neutron, are three quark states, one of each color, while anti-baryons are three anti-quark states with three different anti-colors (anti-RED, anti-BLUE, and anti-GREEN). Mesons are quark anti-quark pairs with a color and corresponding anti-color.

The other main particle group contains four types of gauge bosons as shown in Table 1.1. With their effects. The Higgs field involves to generate mass and Higgs bosons discovered by quantizing the Higgs field in 2012 [18].

Table 1.1: The Fundamental gauge bosons

<b>Effects</b>	<b>Boson</b>
Strong Force	Gluons $g$
Electro-Magnetic Force	Photons $\gamma$
Weak Force	$W^\pm$ and $Z$

In the proton, the quarks are charged and feel the electromagnetic force carried by the photon. The electromagnetic force should cause these quarks to fly apart, but they do not due to the strong interaction. This force ties the quarks in the proton together via gluon exchange. Electrons are bound to the nucleus in atoms by the electromagnetic interaction [17].

The sun contains Hydrogen (H) that is transformed into Helium (He). This process is driven by the weak interaction. Fundamentally, up-quarks are transforming into down-quarks in an interaction mediated by the weak force, carried by the  $W^\pm$  gauge bosons whose emission and decay leads to the transformation of the quarks [16].

The baryon asymmetry of the universe is another important observation. Immediately after the Big Bang, there existed an almost equal amount of matter and anti-matter existed. However, today the Universe is dominated by matter, and we see no anti-matter particles at macroscopic scales. There should be a mechanism in the early universe which leads to this matter-anti-matter asymmetry.

Andrei Dmitrievich Sakharov [19] gave three conditions to break the matter-anti-matter symmetry in the early universe. These are called the Sakharov conditions :

- Baryon number violation: Total baryon number of initial state and final state are not equal .
- Charge and Parity(CP)-violation: Described in Sections 1.2 and 1.4.
- Interactions out of thermal equilibrium.

However the amount of CP-violation measured so far does not explain the observed matter-anti-matter asymmetry.

## 1.2 The $C$ , $P$ , and $T$ Symmetries

One of the most important ideas in the SM is the importance of symmetries. In physics symmetries stem from something being conserved or remaining constant within a system or experiment. Conservation laws and symmetries are strongly related to each other. Three important symmetries in particle physics, are charge conjugation( $C$ ), parity( $P$ ), and time-reversal ( $T$ ) [20].

- Charge conjugation( $C$ ) is electric charge inversion. This operation is defined by the change of particle into its an anti-particle leaving their other physical properties unchanged. Charge conjugation can have only two eigenvalues  $\eta_c = \pm 1$ . All of the known interactions conserve charge. Particle momentum function  $f(\underline{p})$  and anti-particle momentum function  $\bar{f}(\underline{p})$  can write symbolically

$$C|f(\underline{p})\rangle = \eta_c|\bar{f}(\underline{p})\rangle \quad (1.1)$$

- Parity ( $P$ ) is the transformation of a space coordinate  $\underline{r} \rightarrow -\underline{r}$ . Linear momentum is also reversed due to parity  $\underline{p} \rightarrow -\underline{p}$ , but not intrinsic angular momentum, spin, as the Pauli spin,  $\underline{\sigma}$ , are unchanged under the Parity transformation. According to Equation 1.2, helicity( $\lambda$ ) will change sign in parity inversion. Repeated Parity transformations lead back to the initial state, and it has only two eigenvalues  $\eta_p = \pm 1$ .

$$\lambda = \underline{\sigma} \cdot \underline{p}/|p| \quad (1.2)$$

$$P|f(\underline{p})\rangle = \eta_p|\bar{f}(-\underline{p})\rangle \quad (1.3)$$

Parity is conserved in the strong and electromagnetic interactions but not in weak interactions. This surprising observation was made in weak mediated atomic transitions [21]. The combined transformation for charge and parity, CP, has two eigenvalues  $+1$  for CP-even and  $-1$  for CP-odd.

$$CP|f(\underline{p})\rangle = \eta_{cp}|\bar{f}(-\underline{p})\rangle \quad (1.4)$$

Early thinking was that CP (the combined operation of parity transformation and charge conjugation) would be conserved in the weak interaction.

- Time reversal (T): transformation of  $t$  into  $-t$ . This reverses the time flow and time derivatives like momentum and angular momentum.

$$T|f(\underline{p})\rangle = \eta_T|\bar{f}(-\underline{p})\rangle \quad (1.5)$$

Both theoretically and experimentally, studies of the combined CPT symmetry invariance have received significant attention [22]. If CP is violated, then time (T)-symmetry must be violated if CPT is conserved. CP violation has been observed in neutral kaon (a meson containing the strange ( $s$ )-quark) decays and B meson decays [23, 24].

### 1.3 B Meson

The primary goal of the Belle and Belle II experiments is to study the properties of B mesons by accelerating and colliding  $e^+$  and  $e^-$ . B mesons contain the most massive quark, which survives long enough to form bound states, the  $b$ -quark. There are eight different B mesons consisting of a bottom anti-quark and either an up, down, strange, or charm quark. Due to the top quark's short life time it is not possible to have a B meson consisting of a bottom anti-quark and a top quark [16]. Each B meson has an anti-particle, and details of the B mesons are shown in Table 1.2.

Table 1.2: B meson family [1]

Particle	Anti-Particle	Quark Content	Charge	Isospin	Spin and Parity	Rest Mass ( $MeV/C^2$ )	Life Time ( $\times 10^{-12}S$ )
$B^+$	$B^-$	$u\bar{b}$	+1	1/2	$0^-$	$5279.29\pm 0.15$	$1.638\pm 0.004$
$B^0$	$\bar{B}^0$	$d\bar{b}$	0	1/2	$0^-$	$5279.61\pm 0.16$	$1.520\pm 0.004$
$B_S^0$	$\bar{B}_S^0$	$s\bar{b}$	0	0	$0^-$	$5366.79\pm 0.23$	$1.510\pm 0.005$
$B_C^+$	$B_C^-$	$c\bar{b}$	+1	0	$0^-$	$6275.10\pm 1.00$	$0.507\pm 0.009$

The Upsilon meson, a  $b$  anti- $b$  quark pair, was discovered at Fermilab in 1977. The interaction chain  $e^+ + e^- \rightarrow \Upsilon(4S) \rightarrow B^+ + B^-$  and  $B^0 + \bar{B}^0$  are realized by colliding beams of electrons and positrons head-on with a center-of-mass energy equivalent to the mass of the  $\Upsilon(4S)$ . By using the  $\Upsilon(4S)$  we can study the properties of  $B^\pm$  and  $B^0$  mesons. From the more massive  $\Upsilon(5S)$  we can study the  $B_S^0$  using the interaction chain  $e^+ + e^- \rightarrow \Upsilon(5S) \rightarrow B_S^0 + \bar{B}_S^0$ .

Neutral kaons, a meson with a strange quark, decay showed the first evidence of meson mixing. This is when a particle turns into its own anti-particle, and is also known as flavor oscillation. B meson mixing is possible for both the  $B^0$  and  $B_S^0$ . Studying this effect in B mesons is very interesting because they were expected to show a difference in behavior between matter and anti-matter, i.e. different oscillation rates for a B into an anti-B as compared to an anti-B into a B. This stems from certain types of weak decays violating CP symmetry or alternatively exhibited CP-violation. CP-violation can be observed in three different ways.

#### 1.4 CP Violation

Particle physics handbooks describe [23] CP violation manifesting in three different ways. All these can be observed in the neutral B meson system. The three types are:

- Direct CP violation
- CP violation in mixing
- CP violation in interference between direct and mixing

The charged B meson only has direct CP violation. The amplitudes of CP eigenstates of B mesons decaying to a specific final state  $f$  and the anti-B meson to the CP inverted final state  $\bar{f}$  are represented as:

$$A_f = \langle f|H|B\rangle \quad (1.6)$$

$$\bar{A}_f = \langle f|H|\bar{B}\rangle \quad (1.7)$$

$$A_{\bar{f}} = \langle \bar{f}|H|B\rangle \quad (1.8)$$

$$\bar{A}_{\bar{f}} = \langle \bar{f}|H|\bar{B}\rangle \quad (1.9)$$

#### 1.4.1 Direct CP Violation

This is the difference between branching fractions of a B meson to its final state  $f$ , compare with the anti-B to the final state  $\bar{f}$ . Direct CP violation is the only type available where B cannot decay to  $\bar{f}$  and  $\bar{B}$  cannot decay in to  $f$ , but this does not preclude B and  $\bar{B}$  having the same final state, i.e.  $f$  cannot be accessible to decay of  $\bar{B}$ , and likewise,  $\bar{f}$  cannot be accessible by B. The definition of directCP violation can be represented as

$$\left| \frac{\bar{A}_{\bar{f}}}{A_f} \right| \neq 1. \quad (1.10)$$

Direct CP violation can be observed in both charged and neutral B mesons, but for charged mesons, it is the only type that can occur. The other two types require meson oscillation which occur only for neutral mesons. In direct CP violation the CP violation

parameter is

$$A_{CP} = \frac{\Gamma(\bar{B} \rightarrow \bar{f}) - \Gamma(B \rightarrow f)}{\Gamma(\bar{B} \rightarrow \bar{f}) + \Gamma(B \rightarrow f)}. \quad (1.11)$$

### 1.4.2 CP Violation in Mixing

In B meson weak decays, it is important to consider mass eigenstates which are linear combinations of flavor eigenstates. This is implemented by the superposition of two general neutral B states as

$$|\psi\rangle = \alpha|B^0\rangle + \beta|\bar{B}^0\rangle. \quad (1.12)$$

The behavior of the above state obeys the time-dependent Schrodinger equation

$$i\frac{\partial\psi}{\partial t} = H\psi, \quad (1.13)$$

where the Hamiltonian, H, is given by

$$H = M - i\frac{\Gamma}{2}. \quad (1.14)$$

Here H is a  $2 \times 2$  Hermitian matrix. From the properties of CPT invariance  $H_{11} = H_{22}$  and  $H_{12} = H_{21}$  only if CP invariance is assumed. Then the Schrödinger equation can be specified in terms of two coupled modes

$$|\psi_1\rangle = \sqrt{1/2}(|B^0\rangle + |\bar{B}^0\rangle), \text{ and} \quad (1.15)$$

$$|\psi_2\rangle = \sqrt{1/2}(|B^0\rangle - |\bar{B}^0\rangle). \quad (1.16)$$

Using Equations 1.13, 1.14, 1.15, and 1.16

$$i\frac{\partial}{\partial t}\psi_{1,2} = M_{1,2}|\psi_{1,2}\rangle - i\frac{\Gamma_{1,2}}{2}|\psi_{1,2}\rangle. \quad (1.17)$$

The general solution of Equation 1.17 is

$$|\psi_{1,2}(t)\rangle = |\psi_{1,2}(0)\rangle e^{-iM_{1,2}t} e^{-\frac{\Gamma_{1,2}t}{2}}. \quad (1.18)$$

where the mass  $M_{1,2}$  and width  $\Gamma$  are

$$M_{1,2} = \text{Re}(H_{11} \pm H_{21}), \text{ and} \quad (1.19)$$

$$\frac{\Gamma_{1,2}}{2} = \text{Im}(H_{11} \pm H_{21})$$

The mass and width differences of the two states difference are

$$\Delta m = |M_1 - M_2|, \text{ and} \quad (1.20)$$

$$\Delta\Gamma = |\Gamma_1 - \Gamma_2|. \quad (1.21)$$

According to Equations 1.15, 1.16, and 1.19, the  $|\psi_1\rangle$  and  $|\psi_2\rangle$  states have different masses. In general, we can use mass terms for  $|\psi_1\rangle \approx |B_L\rangle$  and  $|\psi_2\rangle \approx |B_H\rangle$  where H and L stand for the Heavier and Lighter B meson mass eigenstates. In general Equations 1.15 and 1.16 can be rewritten as

$$|B_H\rangle = p|B^0\rangle - q|\overline{B^0}\rangle, \text{ and} \quad (1.22)$$

$$|B_L\rangle = p|B^0\rangle + q|\overline{B^0}\rangle, \quad (1.23)$$

where  $|p|^2 + |q|^2 = 1$ .

From Equations 1.14, 1.15, 1.22, and 1.23 the ratio of  $q$  and  $p$  is

$$\frac{|q|^2}{|p|^2} = \frac{|M_{12}^* - \frac{i}{2}\Gamma_{12}^*|}{|M_{12} - \frac{i}{2}\Gamma_{12}|}. \quad (1.24)$$

If  $M_{12} = M_{12}^*$  and  $\Gamma_{12} = \Gamma_{12}^*$  then CP is conserved and  $|q/p| = 1$ . If this ratio is not equal to one, then this is called CP-violation in mixing or indirect CP violation.

### 1.4.3 CP violation in interference between direct and mixing

This can occur only in neutral B meson decays to the same final state  $f$  for both B and  $\bar{B}$ . This final state can be reached in two different ways: in a direct decay  $B \rightarrow f$  or an indirect decay via mixing  $\bar{B} \rightarrow B \rightarrow f$ . We define a parameter  $\lambda$

$$\lambda = \frac{q \bar{A}_f}{p A_f}. \quad (1.25)$$

If  $|\lambda| \neq 1$ , then there is CP violation. However, if CP violation occurs via this channel, then the imaginary part of  $\lambda$  is not equal to zero. Therefore if  $|q/p| = 1$  and  $\Delta\Gamma = 0$   $A_{CP}$  can be rewritten as

$$A_{CP} = \frac{2\text{Im}(\lambda)}{1 + |\lambda|^2} \sin(\Delta mt) - \frac{1 - |\lambda|^2}{1 + |\lambda|^2} \cos(\Delta mt). \quad (1.26)$$

## 1.5 CKM Matrix

The Cabibbo-Kobayashi-Maskawa (CKM) matrix is a unitary matrix that shows the strength of quark flavor transitions mediated by the weak interaction in the Standard Model. In 1963, Nicola Cabibbo introduced the Cabibbo angle ( $\theta_C$ ) and explained any down type quark coupled to up type quarks via charged current weak interaction as a superposition of all the down type quarks [25]. This relationship can be represented as

$$\begin{pmatrix} d' \\ s' \end{pmatrix} = \begin{pmatrix} \cos \theta_C & \sin \theta_C \\ -\sin \theta_C & \cos \theta_C \end{pmatrix} \begin{pmatrix} d \\ s \end{pmatrix} \quad (1.27)$$

This matrix was expanded by introducing the third generation of quarks by Makoto Kobayashi and Toshihide Maskawa. The CKM matrix relates weak and mass eigenstates of down-type quarks

$$\begin{pmatrix} d' \\ s' \\ b' \end{pmatrix} = \begin{pmatrix} V_{ud} & V_{us} & V_{ub} \\ V_{cd} & V_{cs} & V_{cb} \\ V_{td} & V_{ts} & V_{tb} \end{pmatrix} \begin{pmatrix} d \\ s \\ b \end{pmatrix} \quad (1.28)$$

where  $V_{xy}$  represents the probability that  $y$  quark decay in to  $x$  quark. This unitary  $3 \times 3$  matrix has three real parameters and one phase parameter. The standard CKM matrix parameterization uses three Euler angles  $\theta_{12}$ ,  $\theta_{23}$ ,  $\theta_{13}$  and one CP phase ( $\delta_{13}$ ) [26]. The standard notation of CKM matrix can be written as

$$V = \begin{pmatrix} C_{12}C_{13} & S_{12}C_{13} & S_{13}e^{-i\delta} \\ -S_{12}C_{23} - C_{12}S_{23}S_{13}e^{i\delta} & C_{12}C_{23} - S_{12}S_{23}S_{13}e^{i\delta} & S_{23}C_{13} \\ S_{12}S_{23} - C_{12}C_{23}S_{13}e^{i\delta} & -C_{12}S_{23} - S_{12}C_{23}S_{13}e^{i\delta} & C_{23}C_{13} \end{pmatrix} \quad (1.29)$$

where the notations  $C_{ij} = \cos \theta_{ij}$  and  $S_{ij} = \sin \theta_{ij}$ . Euler angles describe the coupling across the different generations.

The Wolfenstein representation [27] of the CKM matrix is a valuable approximate parameterization of the CKM matrix, which is widely use in B physics:

$$V = \begin{pmatrix} 1 - \lambda^2/2 & \lambda & A\lambda^3(\rho - i\eta) \\ -\lambda & 1 - \lambda^2/2 & A\lambda^2 \\ A\lambda^3(1 - \rho - i\eta) & -A\lambda^2 & 1 \end{pmatrix} + o(\lambda^4) \quad (1.30)$$

where  $\lambda = S_{12}$  (the original Cabibbo parameter),  $A\lambda^2 = S_{23}$ ,  $A\lambda^3(\rho - i\eta) = S_{13} e^{-i\delta}$ . The current best values of the Wolfenstein parameters values are [28]

$$\lambda = 0.2257_{-0.0010}^{+0.0009}, A = 0.814_{-0.022}^{+0.021}, \rho = 0.135_{-0.016}^{+0.031} \text{ and } \eta = 0.349_{-0.017}^{+0.015} \quad (1.31)$$

CP violation comes from the complex elements in the CKM matrix. In the CKM matrix of Equation 1.29,  $\delta$  gives the CP violating effects. In the Wolfenstein parametrization 1.30, a non-zero value of  $\eta$  gives CP violation.

## 1.6 The Unitary Triangle

The CKM matrix is unitary, and taking products of different rows and columns generates nine relations among the matrix elements in the form of

$$V_{ud}V_{us}^* + V_{cd}V_{cs}^* + V_{td}V_{ts}^* = 0, \quad (1.32)$$

or

$$V_{ud}V_{ud}^* + V_{us}V_{us}^* + V_{ub}V_{ub}^* = 1. \quad (1.33)$$

Six of these contain complex numbers, and the unitarity relationship can be represented as a triangle in the complex plane. The first and third columns in the CKM matrix give

$$V_{ud}V_{ub}^* + V_{cd}V_{cb}^* + V_{td}V_{tb}^* = 0, \quad (1.34)$$

and each side of the unitary triangle have the same order of magnitude. A plot of Equation 1.34 in the complex plane is shown in Figure 1.2

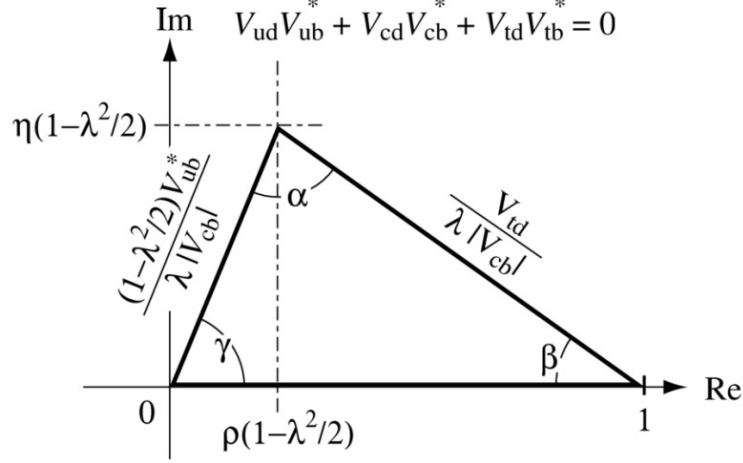


Figure 1.2: The unitarity triangle representation in the complex plane [2]. Both Belle and Belle II use  $\phi_1 \equiv \beta$ ,  $\phi_2 \equiv \alpha$ ,  $\phi_3 \equiv \gamma$

The coordinates of the peak of the triangle are  $(\rho(1-\lambda^2/2), \eta(1-\lambda^2/2))$ . By dividing all the sides by  $|V_{cd}V_{cb}^*|$ , i.e. normalizing the bottom edge of the triangle length to 1 and other sides have lengths

$$\frac{V_{ud}V_{ub}^*}{|V_{cd}V_{cb}^*|} = \frac{(1-\lambda^2/2)V_{ub}^*}{\lambda|V_{cb}^*|}, \quad (1.35)$$

and

$$\frac{V_{td}V_{tb}^*}{|V_{cd}V_{cb}^*|} = \frac{V_{td}}{\lambda|V_{cb}^*|}. \quad (1.36)$$

The three angles of the triangle are named  $\alpha$ ,  $\beta$ , and  $\gamma$  defined as follows

$$\alpha \equiv \phi_2 \equiv \arg \left[ -\frac{V_{td}V_{tb}^*}{V_{ud}V_{ub}^*} \right], \quad (1.37)$$

$$\beta \equiv \phi_1 \equiv \arg \left[ -\frac{V_{cd}V_{cb}^*}{V_{td}V_{tb}^*} \right], \quad (1.38)$$

$$\gamma \equiv \phi_3 \equiv \arg \left[ -\frac{V_{ud}V_{ub}^*}{V_{cd}V_{cb}^*} \right]. \quad (1.39)$$

The right side of the unitarity triangle and the angle  $\beta$  are measured by studying the oscillation of  $B^0$ ,  $\bar{B}^0$  and place it inside the yellow ring covered by a large orange ring, as

shown in Figure 1.3. BaBar experiment at SLAC in California and the Belle experiment at KEK in Japan measured  $\sin(2\beta)$ , and it contains four possible solutions, as shown as the four narrow cone shapes from the bottom corner of the triangle in Figure 1.3.

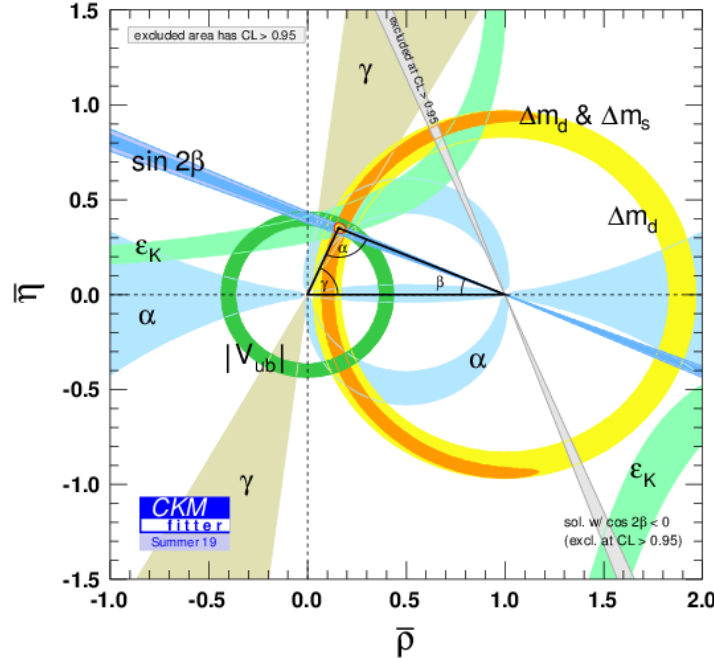


Figure 1.3: Constraints on the unitary triangle from the CKM fitter collaboration [3].

The other two angles,  $\alpha$ , and  $\gamma$  are more difficult to measure because  $\gamma$  requires studies of rare decay processes. The B-factories measured these angles, adding two constraints on  $\beta$ . The best measurements of  $V_{ub}$  and  $V_{cb}$  matrix elements come for the left side length of the unitary triangle, which lies in the dark green circle in Figure 1.3.

Still the CKM weak force picture is incomplete. All the current measurements are consistent with the red outlined region in Figure 1.3. To reduce this region with new methods the aim is to measure the position of the vertex of the triangle more precisely. One of the primary goals of the Belle II experiment is to narrow the red outlined region and constrain indications of BSM in B meson decays indicated by an inconsistent picture of the Unitary Triangle.

### 1.7 Weak phase and Strong Phase

As seen in Equations 1.6 to 1.9 the complex decay amplitude is a function of real amplitudes and phases. The phases can be divided into two parts called the weak phase,  $\phi$ , and the strong phase,  $\delta$ . The decay amplitude  $A_f$  is a sum of component amplitudes  $A_i$  and phases  $(\delta_i + \phi_i)$  as

$$A_f = \sum_i A_i e^{i(\delta_i + \phi_i)}. \quad (1.40)$$

Similarly replacing the  $(\delta_i + \phi_i)$  term with  $(\delta_i - \phi_i)$ , the CP conjugate decay amplitude is

$$\bar{A}_f = \sum_i A_i e^{i(\delta_i - \phi_i)}. \quad (1.41)$$

Under a CP transformation only the weak interaction phase changes sign, while the strong interaction phase is unchanged. From Equation 1.10 the ratio of the CP conjugate decay amplitude and the original decay amplitude is not one if there is direct CP violation. Similarly Equation 1.11 can be rewritten as

$$A_{CP} = \frac{1 - \left| \frac{\bar{A}_f}{A_f} \right|^2}{1 + \left| \frac{\bar{A}_f}{A_f} \right|^2}. \quad (1.42)$$

Combing Equations 1.40, 1.41 and 1.42 this ratio can be re-arranged as a difference of amplitudes

$$|\bar{A}_f|^2 - |A_f|^2 = 2 \sum_{i,j} A_i A_j \sin(\phi_i - \phi_j) \sin(\delta_i - \delta_j). \quad (1.43)$$

This shows there must be a difference between weak phases and the strong phases for

there to be direct CP violation. These phase differences can be measured experimentally.

### 1.8 Tree and Penguin diagrams for Charmless Decays

In particle physics, Feynman diagrams are commonly used graphical representations and calculation tools to describe interactions. They are a mathematical and pictorial representation which helps to understand any decay from the initial state to the final state. There are many types of Feynman diagram types with fanciful names such as Tadpole diagram, Box diagram, and many more but tree diagrams and penguin diagrams are the most important for my work here.

For weak decay tree diagrams a virtual  $W^\pm$  mediates the decay of a heavier quark into a lighter quark and the  $W$  then decays into a pair of quarks or leptons. Penguin diagrams contain a loop. If a quark radiates a gluon from this loop it is called a gluonic penguin; if a  $Z^0$  boson or photon, then it is called an electroweak penguin. In the Figure 1.4, a tree diagram is shown on the left, where the  $W$  boson decays into a  $u$  and  $\bar{s}$ . The right side shows a penguin diagram with a virtual loop that can emit a gluon or photon and converts a heavy quark into a light quark. This radiated gluon or photon materializes as a quark-anti-quark pair.

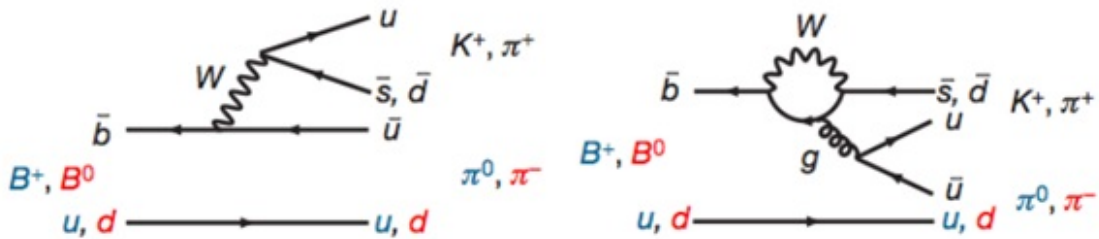


Figure 1.4: Left side is a tree and the right side is a penguin diagram [4].

Most tree-level decays of B mesons are to charm states, i.e the meson with a  $b$  quark goes to another meson containing a  $c$  quark. Any B meson decay process in which the  $b$  quark does not go to a  $c$  quark ( $b \rightarrow c$ ) is called charmless B decay. Charmless transitions can proceed by a  $b \rightarrow u$  transition via a tree level diagram or  $b \rightarrow s$  or  $d$  via a penguin

diagram. Both decay types are highly suppressed compared to the  $b \rightarrow c$  transition and have suppressed branching fractions, in the  $10^{-4}$  -  $10^{-5}$  range.. This low branching fraction is a huge challenge to separate strong and weak phases in B-meson decay. Penguin processes are dominant in B meson charmless decays. Therefore it is possible to have many more contributions from unknown particles in the loop process and leading to a CP-violation contribution from BSM [29].

### 1.9 Dalitz analysis

The Dalitz plot is frequently used in particle physics. It is named after Richard Dalitz (1925-2006), a professor at Chicago and Oxford [30]. The Dalitz plot is a visual representation of the phase space of a decay of an initial particle into three final state particles. As an example let us assume a particle  $X$  decays into three particles  $a, b, c$  ( $X \rightarrow a b c$ ). The plot shows all kinematic boundaries of the three particles using two invariant masses squared, as shown in Figure 1.5. The main advantage of these plots is intermediate resonances and their spins are evident by inspection of the plot. More information on Dalitz analysis and its kinematics are given in Section 3.4.

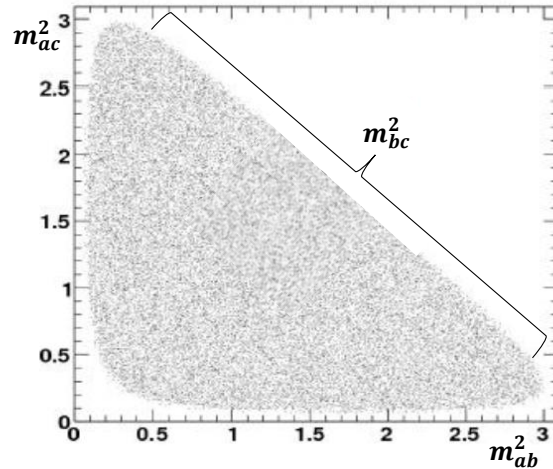


Figure 1.5: Uniformly distributed Dalitz plot [5].

## 1.10 Overview of this Thesis

The large mass of  $B$  mesons leads to many possible decay channels. Among the categories are charmless decay, charmed decay, quasi-two-body decay, and so on. This thesis contains a study of of the charmless three-body decay  $B \rightarrow K_S^0 \pi^+ \pi^0$ .

Chapter 1 covers some basic theories related to these three-body decays, such as fundamental particles and forces in the current universe, symmetry breaking in the early universe with CP violation, why the B meson is important, etc. As mentioned in Sections 1.6 and 1.8, this charmless decay is sensitive to the angle  $\gamma$  in the unitary triangle and charmless decays open new window to analyze the CP violation process via tree and penguin diagrams. It is very important to determine the short-lived particles that are intermediate between the initial decaying state and the final three bodies. This process is done with the Dalitz techniques described in Section 3.4 and helps to understand the nature of these intermediate resonances.

Chapter 2 describes the experiment set up. I describe the KEKB accelerator ring and the Belle detector. Belle II is an upgrade of Belle detector and at a projected luminosity 50 times that observed by the Belle detector. In this chapter the Belle data acquisition system is also covered.

Chapter 3 covers the analysis done in this thesis. Particle identification and reconstructions, data analysis tools such as basf2(Belle II software), multivariate analysis(MVA), Laura++, and the Dalitz technique are among the analysis techniques discussed in this chapter.

Chapter 4 details results of the analysis including selection criteria, intermediate resonances, graphs, Dalitz plots, data driven background estimation, branching fraction calculation and others.

Chapter 5 is a summary, conclusion, discussion and future works of the results. Comparisons are made with results from the BaBar experiment and PDG [1].

## CHAPTER 2 BELLE EXPERIMENT

The Belle collaboration is an international particle physics collaboration with more than 900 physicists and engineers across the world. The experiment operates at the High Energy Accelerator Research Organization, Tsukuba Japan, also known as KEK. It is based on the large asymmetric electron and positron collider called KEKB. The main goal of this B factory is to measure CP violation effects in B mesons [31]. Belle is placed in the interaction point of the KEKB accelerator which held the highest luminosity record at  $2.11 \times 10^{34} \text{ cm}^{-2} \text{ s}^{-1}$  and Belle collected  $1 \text{ ab}^{-1}$  of data from 1999 to 2010.

### 2.1 KEKB Accelerator

KEKB is an asymmetric electron and positron collider with a high-energy ring at (HER)  $8.0 \text{ GeV}$  for electrons and a low-energy ring (LER)  $3.5 \text{ GeV}$  for positrons. This asymmetry causes B meson to move from the interaction point with a flight length long enough for time dependent CP violation measurements. The circumference of both rings is  $3016 \text{ m}$  and they are constructed  $11 \text{ m}$  underground. These rings have four main stations called Fuji, Nikko, Tsukuba and Oho [32]. As shown in Figure 2.1 positrons come from Oho side, electrons come from Nikko side and collisions occur in Tsukuba station where the Belle detector is located.

Positrons are produced by colliding an electron beam with a tungsten heavy metal target. When the electron beam hits this target, it produces a shower of particles including positrons. The positrons are isolated and collected using pulsed magnetic coils in a linear accelerator (LINAC). Then, both electron and positron beams are accelerated to their final energy and injected into the KEKB rings [33]. Both electron and positron beams are accelerated close to the speed of light and circulate inside the beam pipe using dipole, quadrupole and sextupole magnets along the beam pipe. During the physics experiment time, i.e. collision time, both beam pipes maintain constant high currents  $1.7 \text{ A}$  in LER and  $1.4 \text{ A}$  in HER. They are focused to maintain a very small beam size with a profile roughly  $150 \mu\text{m}$  horizontal and  $1 \mu\text{m}$

vertical [34]. KEKB reached its high luminosity mainly with help of new technologies such as Accelerator Resonant Storage damped RF cavity (ARES), a superconducting damped cavity, a radiation/background-free interaction region with a large crossing angle.

The Equation 2.1 uses the energies of each ring to set the center of mass energy, 10.58 GeV i.e. the  $\Upsilon(4S)$  meson mass,

$$E_{CM} = 2\sqrt{E_{HER} \times E_{LER}}. \quad (2.1)$$

At this energy  $e^+ + e^- \rightarrow \Upsilon(4S)$  has a large cross-section. Thus it produces a large number of  $B\bar{B}$  pairs and with energy adjustments is also able to collect data at the other Upsilon resonances. KEKB ran from 1998 to 2010 when it was shut down for the upgrade to SuperKEKB [35].

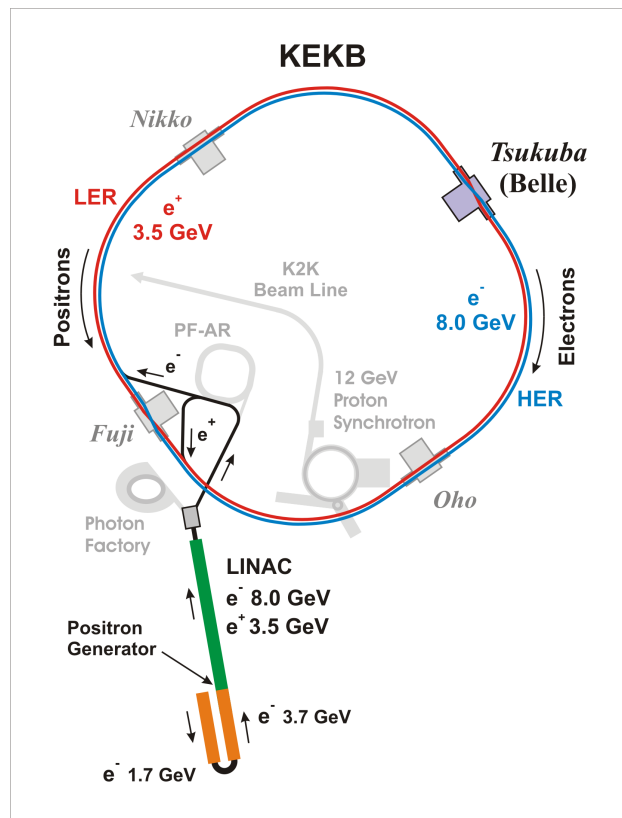


Figure 2.1: Schematic diagram of the KEKB accelerator [6].

## 2.2 Belle Detector

The Belle detector is designed to study B mesons and understand the difference between matter and antimatter, specifically CP violation. The detector is composed of several layers designed for specific tasks. The Silicon Vertex Detector (SVD) placed close to the interaction point helps to measure decay vertices of B mesons. The Central Drift Chamber (CDC) measures momentum using the bending of charged particles in an axial magnetic field. It also measures the energy loss of the charged particles. Charged hadrons are identified using the combination of CDC, Aerogel Cherenkov Counter (ACC) and Time Of Flight (TOF) counters. The Electromagnetic Calorimeter (ECL) is used to identify electrons, positrons, and photons. The outer most layer consists of thick iron plates helps to identify long lived particles such as neutral kaons and muons (KLM). Figures 2.2 and 2.3 shows a schematic of the Belle detector with its layers.

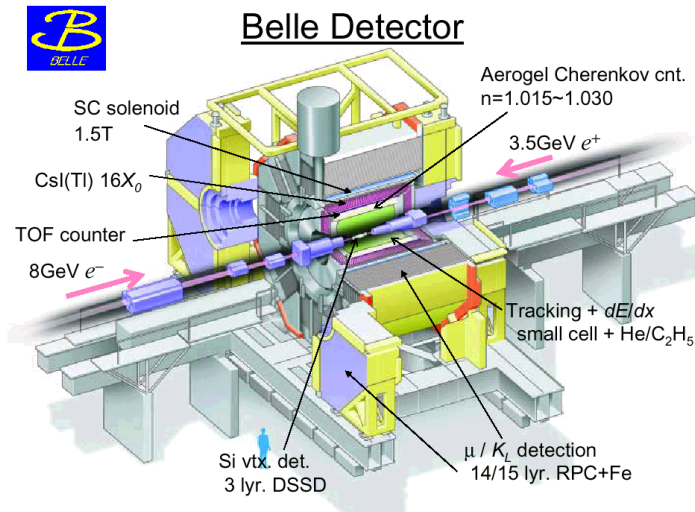


Figure 2.2: Schematic diagram of the Belle detector [7].

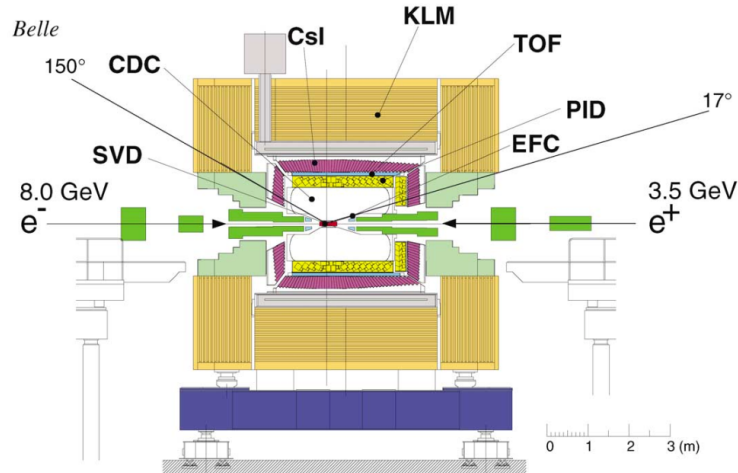


Figure 2.3: Cross section of the Belle detector [7].

### 2.2.1 Beam Pipe

The most important part of the experiment is precise measurements of decay vertices. Coulomb scattering inside the beam pipe wall, and the most inner layer in the silicon vertex detector reduce the resolution in direction along the beams. Therefore, it is important to minimize the thickness of the beampipe wall. After considering high radiation effects Beryllium is used for the material for beam pipe because it has low radiation length. As shown in Figure 2.4 the beam pipe is constructed with two layers of inner radius 20.00  $mm$  and outer radius 23.00  $mm$  [8]. The outside of the pipe is coated with a thin gold layer to reduce low energy X-ray backgrounds. The electron and positron beams create a huge amount of heat. This heat will cause damage to electronics placed near the interaction point, especially the vertex detector. The beam pipe needs a proper cooling system. Helium gas is flowed between two walls of the beam pipe to provide a good cooling system and is able to maintain  $25^{\circ}C$  inside the beam pipe.

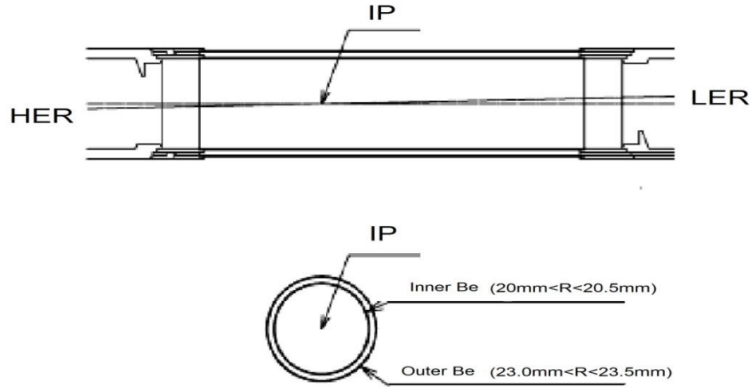


Figure 2.4: Schematic diagram of the Belle beam pipe [8].

### 2.2.2 Silicon Vertex Detector (SVD)

The silicon vertex detector is made using double-sided silicon detector (DSSD) strips. This detector is placed close to the interaction point (IP) by covering the beam pipe because it is important to have precise measurements of B meson vertices with around  $100 \mu\text{m}$  accuracy. Not only B meson but also D and  $\tau$  decay vertices are measured and its precise position measurements help to track charged particles. Two SVDs were used in the Belle experiment: SVD1 from 1999 to 2003 and the upgrade to SVD2 used until the end of the Belle experiment in 2010. SVD1 consists of three layers of DSSD strips and a total of 32 modules arranged in cylindrical shape. These DSSDs covered a polar angle range of  $23^\circ < \theta < 139^\circ$  which corresponds to 86% of the solid angle. The three layers of strips are located 30, 45.5, and 60.5 mm from the IP. SVD2 increased the number of DSSDs to 54 by adding an extra layer. SVD2 has 4 layers of DSSDs located 20, 43.5, 70, 80 mm from the IP. It has a larger polar angle coverage from  $17^\circ < \theta < 150^\circ$ , representing 92% of the solid angle [8]. Figures 2.5 and 2.6 show the schematic of DSSD configuration of both SVD1 and SVD2.

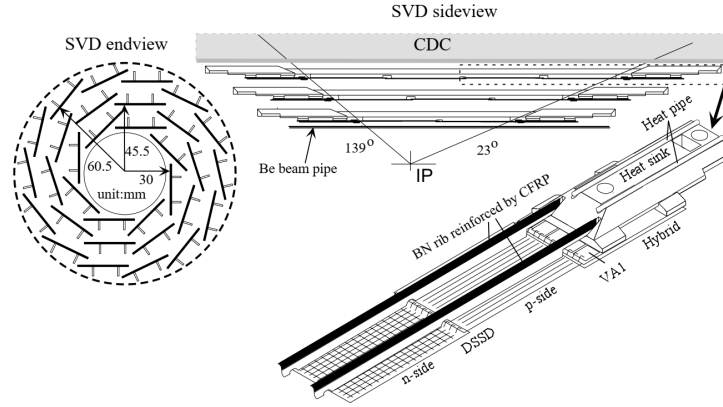


Figure 2.5: Schematic diagram of Belle SVD1 [8].

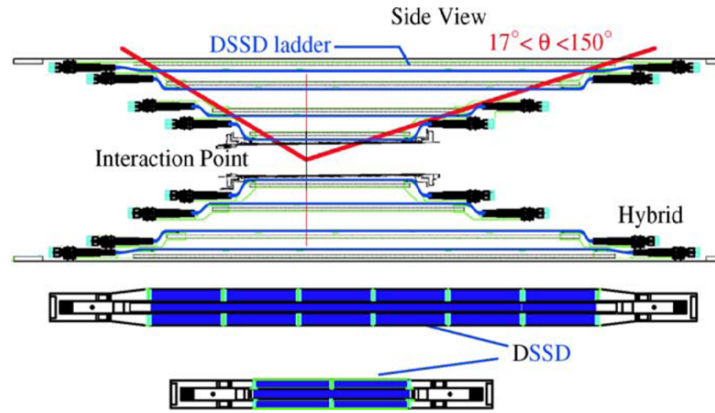


Figure 2.6: Schematic diagram of Belle SVD2 [8].

### 2.2.3 Central Drift Chamber (CDC)

After an electron and positron collision at the Belle interaction point many charged particles fly in three dimensional space through a  $1.5 T$  axial magnetic field. Trajectories of these charged particles have a helical shape. The goal of this CDC is to track all these charged particles and tracking algorithms can measure the longitudinal and transverse momenta ( $P_T$  and  $P_Z$ ) by analyzing the shape of the helix. It also measures the specific ionization,  $dE/dx$ , of the tracked particles [8]. The CDC works together with the three subdetectors SVD, TOF and ACC. The combination of CDC and SVD covers tracking system of the Belle detector. The CDC contributes to particle identification together with TOF and ACC. Figure 2.7 shows the basic schematic view of CDC.

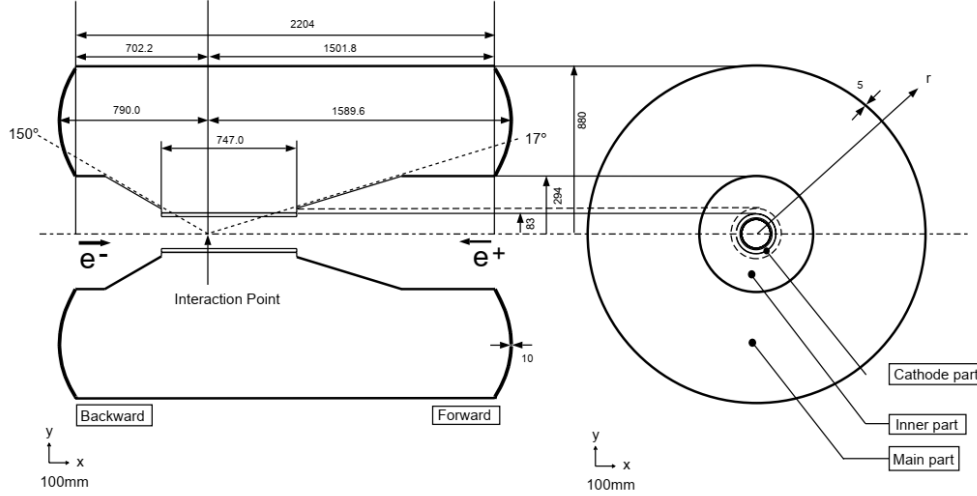


Figure 2.7: CDC structure [8].

The CDC is a drift chamber with  $103.5 \text{ mm}$  inner radius and  $874 \text{ mm}$  outer radius. It covers  $17^\circ < \theta < 150^\circ$  in polar angle which is exactly same as SVD2. This sub-detector contains 8400 cells in 50 cylindrical layers. The structure of each cell contains an anode wire covered by few cathode field wires. The CDC is filled with a mixture of helium ( $He$ ) 50% and ethane ( $C_2H_6$ ) 50%. While  $He$  gas gives easy calibration and good stability,  $C_2H_6$  gives accurate measurement of energy loss. The transverse momentum resolution of this sub-detector is  $\sigma_{P_T}/p_T \sim 0.5\% \sqrt{1 + P_T^2}$  for all charged particles with  $P_T \geq 100 \text{ MeV}/c$ . Spatial resolution lies between  $120 \text{ }\mu\text{m}$  and  $150 \text{ }\mu\text{m}$  depending on incident angle and layer in the CDC [36].

The energy loss directly depends on the velocity of the particle and gas medium filled inside CDC. The rate of energy loss is expressed as

$$-\frac{dE}{dx} = 2\pi N_a r_e m_e c^2 \frac{Zz^2}{A\beta^2} \left[ \ln\left(\frac{2m_e \gamma^2 v^2 W_{max}}{I^2}\right) - 2\beta^2 - \frac{\delta^2}{2} \right], \quad (2.2)$$

where

- $N_a$  = Avogadro's number
- $r_e$  = Electron radius

- $m_e$  = Electron mass
- $c$  = Velocity of light
- $Z$  = Atomic number of the gas medium
- $A$  = Mass number gas medium
- $z$  = Charge of the particle
- $v$  = Velocity of the particle
- $\beta = v/c$  ;  $\gamma = 1/\sqrt{1 - \beta^2}$
- $I$  = Mean excitation potential of the medium
- $W_{max}$  = Maximum energy transfer during the particle-medium collision
- $\delta$  = Density correction factor

This energy loss depends only on charge and velocity ( $\beta$ ) of the particle. The energy loss combined with the momentum of the particle gives information on the mass of the particle [8]. Figure 2.8 shows the scatter plot of  $dE/dx$ , the energy loss, versus the measured momentum and it shows clear separation of pions( $\pi$ ), kaons( $K$ ), protons( $P$ ) and electrons( $e$ ).

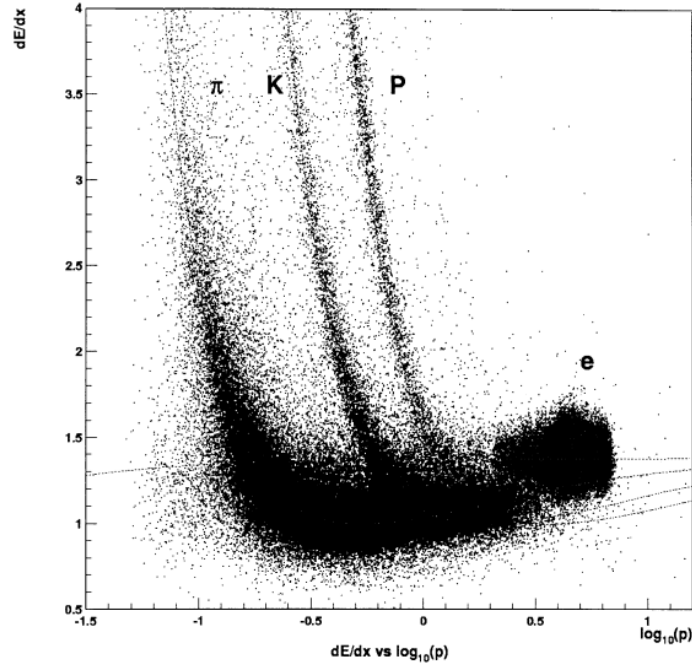


Figure 2.8: Rate of energy loss Vs Momentum of charged particles [8].

#### 2.2.4 Aerogel Cherenkov Counter (ACC)

Aerogel, has an extremely low density and thermal conductivity. This sub-detector is based on Cherenkov radiation using silica Aerogel, a fragile expanded polystyrene, and mainly contained within the barrel and endcap. If a charged particle travels through a dielectric medium at a velocity  $v$  greater than the speed of light in that medium, the particle starts to emit Cherenkov radiation. Threshold velocity for the particle to emit Cherenkov radiation is  $\beta = \frac{v}{c} = \frac{1}{n}$  where  $n$  is the refractive index of the dielectric medium. Compared to the CDC and TOF (Time of Flight) this detector can identify particles with high efficiency especially K (kaon) and  $\pi$  (pion) as it has a refractive index of 1.01 to 1.03 depending on the polar angle as shown in the Figure 2.9.

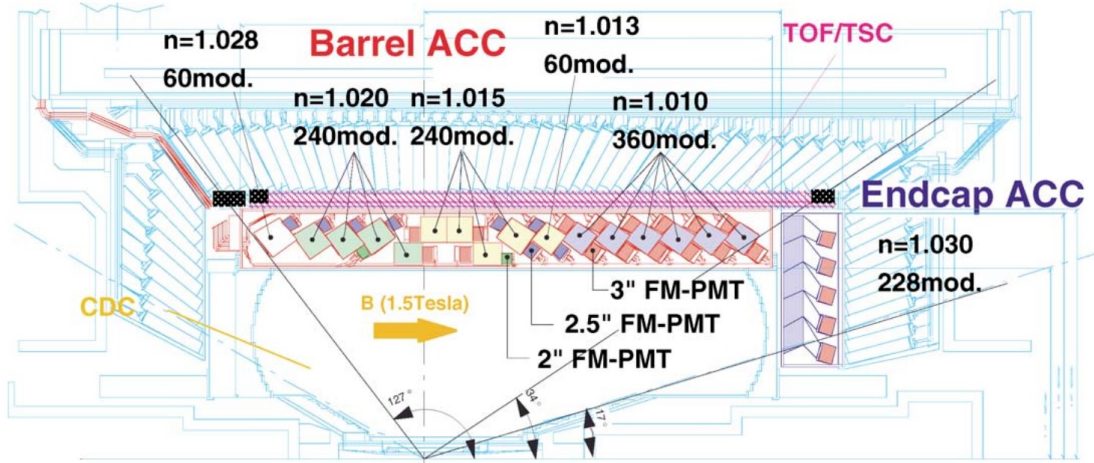


Figure 2.9: Configuration of ACC Barrel [9].

There are 960 modules in the barrel having different dielectric index from 1.01 to 1.028 and 228 modules arranged in 5 different layers for the endcap having refractive index of 1.030. These different index values are able to catch the high momentum range from 1.2 to  $3.5 \text{ GeV}/c$  and provides clear separation of kaons and pions. As shown in Figure 2.10 each module contains at least one fine-mesh, high-gain, photo-multiplier tube (FM-PMT) with diameter 2, 2.5, or 3.0 inch.

Each module is covered by a  $0.2 \text{ mm}$  thick aluminum box with dimensions of  $12 \times 12 \times 12 \text{ cm}^3$ . Inside this box are 5 silica Aerogel tiles. Barrel modules contain two PMTs and (left side Figure 2.10), and endcap modules have only one PMT (right side Figure 2.10). This entire unit works within the  $1.5 \text{ T}$  magnetic field, and for better light collection the inner surface is covered by diffusive reflective sheets. Quality tests done using the radiation source  $^{60}\text{Co}$ , which produces high-intensity  $\gamma$  rays, up to a dose of  $9.8 \text{ Mrad}$  show no degradation or change of refractive index [9].

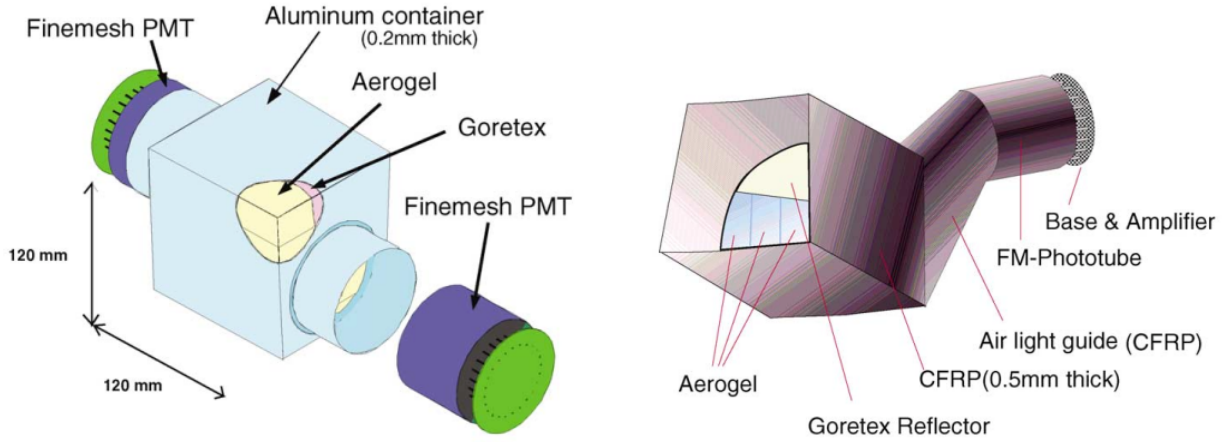


Figure 2.10: Left side Barrel ACC module configuration and Right side Endcap module configuration [9].

### 2.2.5 Time Of Flight counter (TOF)

After an electron-positron collision, TOF measures how long particles take to reach the TOF counters. Roughly this time difference is 3 ns to travel from IP to TOF. This sub detector covers the barrel part of the ACC at a radial distance of roughly 1.2 m from the interaction point. This is the perfect location to capture 90% of particles from  $B\bar{B}$ , and it sends timing signal to the Belle trigger system. TOF clearly identify particles in the momentum range of 0.8 to 1.2 GeV/c within polar angles of  $34^\circ$  to  $120^\circ$ . The structure of the TOF has 64 Trigger Scintillation Counters (TSC) and 128 plastic scintillators. These scintillators are ionized when charged particles pass through and produce optical photons. These optical photons are collected in FM-PMT, the same as in the ACC. TSC has one PMT and TOF have two PMTs. Figure 2.11 shows the dimensions of TOF/TCS counters.

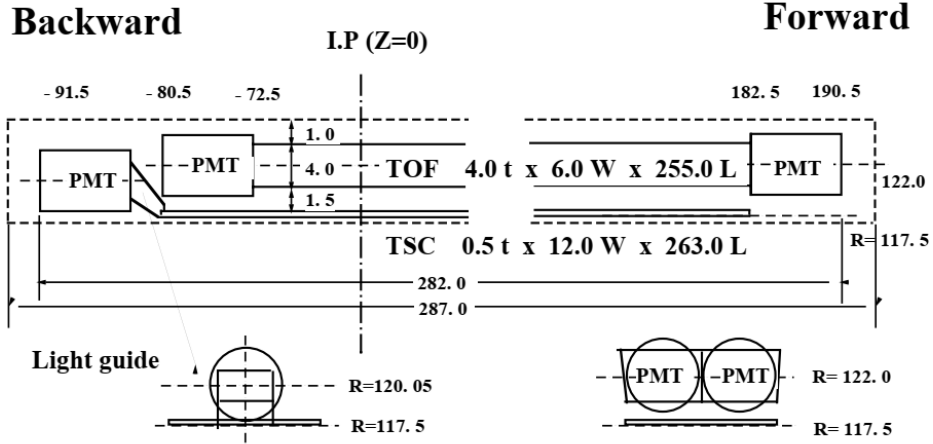


Figure 2.11: Dimensions of TOF and TSC module [8].

From CDC and TOF there is a measure of the flight length, flight time, and momentum of the charged particles. This information relates to the mass of the charged particle as

$$t = \frac{1}{c\beta} = \frac{l}{c} \sqrt{1 + c^2 \left(\frac{m}{p}\right)^2}. \quad (2.3)$$

where:

- $l$  = length of the helical path from IP to TOF
- $\beta$  = velocity of the particle
- $p$  = momentum of the charged particle measured by CDC and SVD
- $t$  = flight time from IP to TOF
- $m$  = mass of the charged particle.

Resolution is very important in the mass calculation in this sub-detector. Therefore the TOF is designed to have 100  $ps$  timing accuracy and is good enough to measure kaons and pions with  $3\sigma$  separation as shown in Figure 2.12.

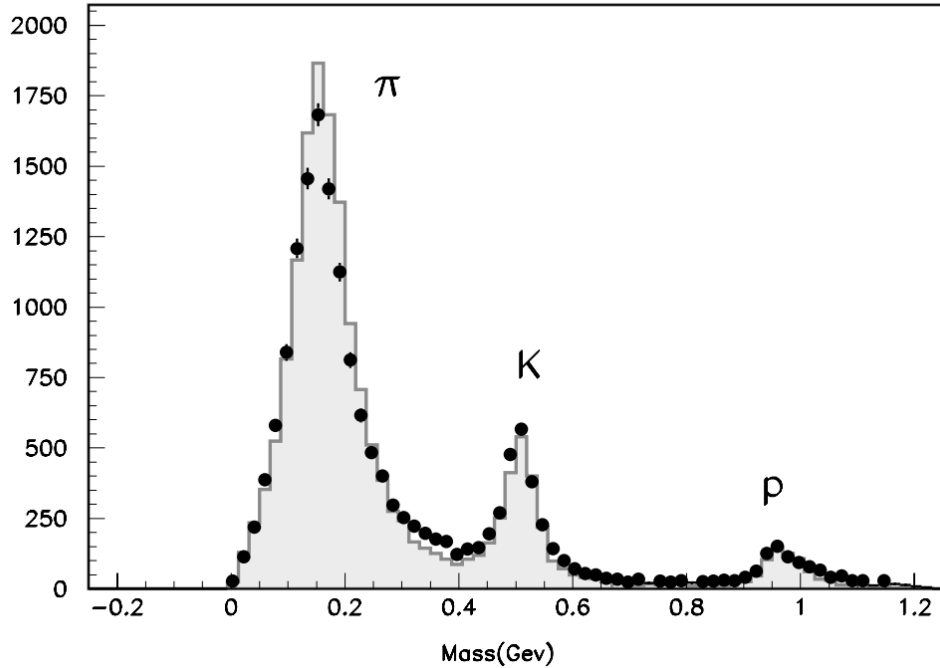


Figure 2.12: The separation of kaon and pions for momentum less than  $1.2 \text{ GeV}/c$ . Black points represent data and histogram represent MC prediction [10].

### 2.2.6 Electromagnetic Calorimeter (ECL)

The electromagnetic calorimeter is designed to identify electrons and photons by measuring and analyzing their electromagnetic showers inside the calorimeter medium with high efficiency. Bremsstrahlung radiation is one of the methods high energy electrons loses their energy. High energy photons can lose their energy by pair production of electron and positron. These newly generated pairs can travel very short distances with clusters of energy deposit as a result of the electromagnetic shower. After the beam collision it produces large numbers of  $\pi^0$  and  $\eta$  particles and these also decay in to photons. In order to identify these unstable particles it is very important to have clear separation of daughter photons and their opening angles. This task requires fine-grained segmentation in the calorimeter.

This sub-detector is much larger than TOF. Figure 2.13 shows the configuration of ECL. All the crystals are built using  $CsI(Tl)$  because it has a large photon yield, mechanical stability, and has a moderate price. This sub-detector consists of three parts: the barrel, forward endcap, and backward endcap. Each part consists of 6624, 1152, and 960 crystals



behavior can be used to calculate particle momentum. The Belle solenoid magnet, shown in Figure 2.14, is designed to produce a very high magnetic field of  $1.5\text{ T}$  and operates with a high current of around  $4000\text{ A}$ . The coils are surrounded by cylinder of  $1.7\text{ m}$  radius and  $4.4\text{ m}$  of length [37].

The complete structure of the superconducting magnet uses roughly 7 tons of coils with  $22\text{ W}$  of thermal load at  $4.2\text{ K}$ . A helium refrigerator unit is attached to the system to maintain the cooling process. During the operation there is a chance for the superconductor to “quench” into a normal conductor. Therefore laminated aluminum strips are used to stabilize the superconductor and quench protection. In most high energy experiments detectors the ECL is located outside of the superconducting magnet. In Belle all the subdetectors are located inside the solenoid cavity except KLM sub-detector. The magnet stores  $6.4\text{ kJ/m}^3$ .

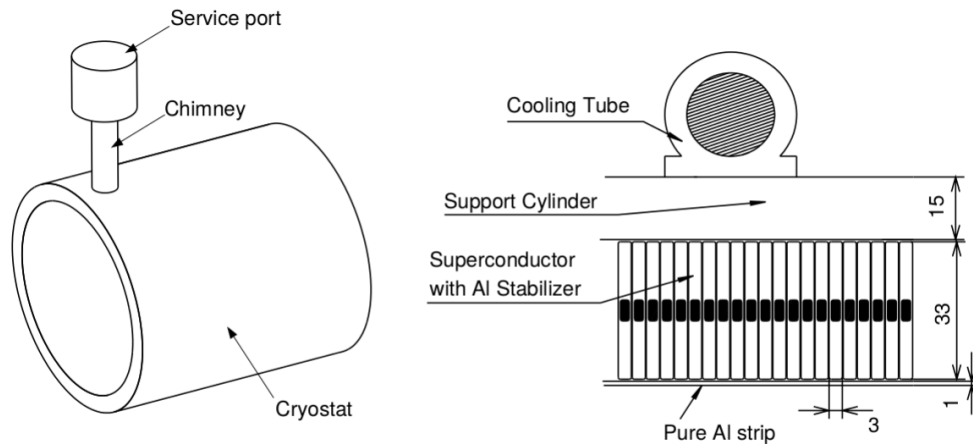


Figure 2.14: The Belle solenoid magnet and the cross-sectional view of the coil [10].

The magnetic field is mainly used to measure the momentum of charged particles. The radius  $R$  of the helical paths depends on the transverse momentum of the charged particle  $p_T$ , magnetic field  $B$ , and charge of the particle  $q$  as

$$R = \frac{p_T}{0.3qB}. \quad (2.4)$$

The radius of the track is measured using the CDC and SVD.

### 2.2.8 K-Long and Muon Detector (KLM)

The K-Long and Muon detector (KLM) is the final layer of the Belle detector, used to identify K-longs,  $K_L^0$ , and muons,  $\mu$ . These particles travel long distances compared to other particles produced after the collision. This sub-detector is located outside of the superconducting magnet and is designed to identify particles in the broad momentum range greater than  $600 \text{ MeV}/c$ . Mainly this system has three parts: barrel, forward endcap, and backward endcap. The barrel covers  $45^\circ < \theta < 125^\circ$  range of polar angle and including both endcaps the KLM covers  $17^\circ < \theta < 155^\circ$  of polar angle. A schematic of the KLM detector is shown in Figure 2.3.

The barrel region has 15 detector layers and 14 - 47  $\text{mm}$  thick iron plates. Both end caps have 28 detector layers. These multiple detector layers and iron layers helps to identify muons and charged hadrons based on scattering. Muons have a relatively long life time, around  $10^{-6} \text{ s}$ , and travel a longer path than other hadrons. Detector layers are made using glass-electrode-resistive plate counters (RPCs). Single RPC layer has two electrodes separated by glass and a gas gap provides high resistivity, shown in Figure 2.15.

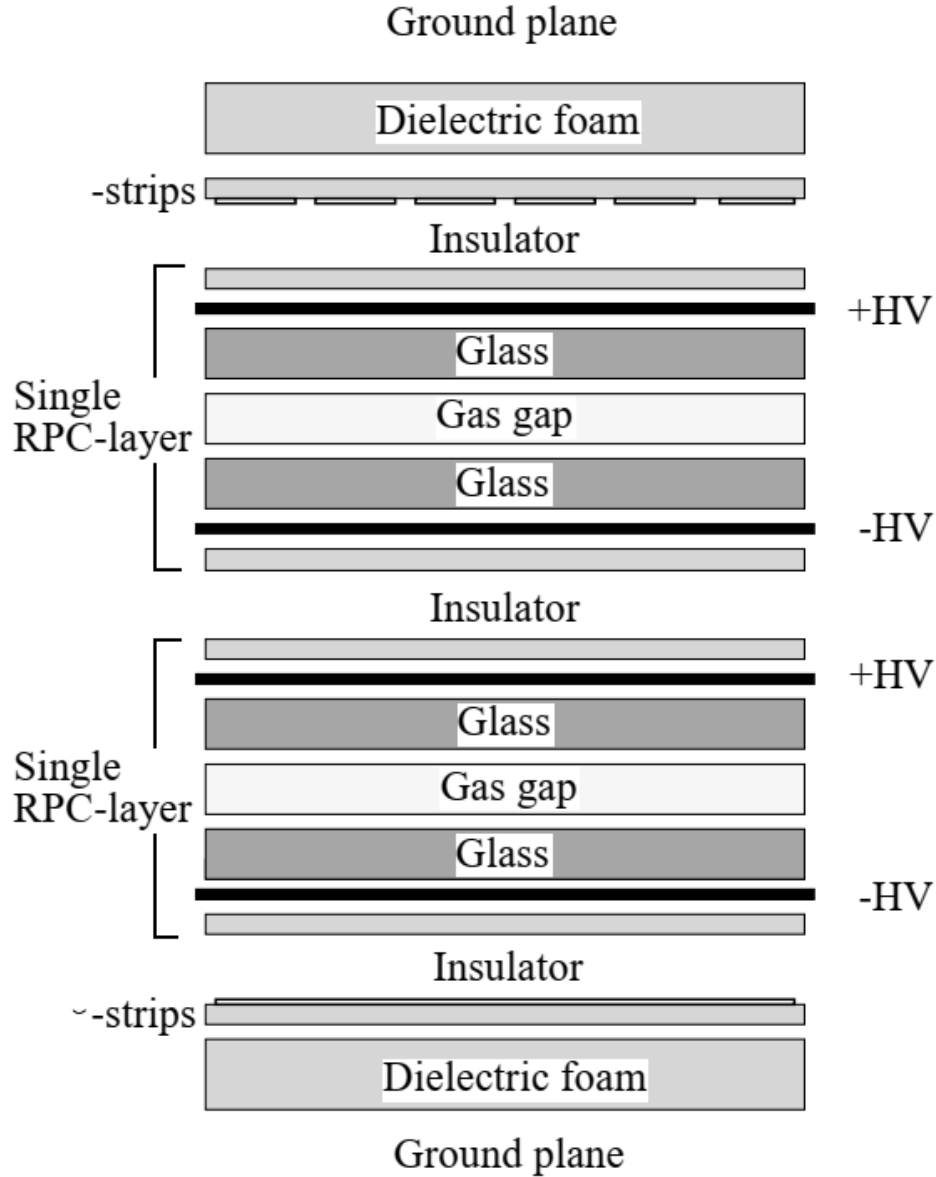


Figure 2.15: Cross-sectional view of KLM detector layers [8].

In the barrel it has 24  $mm$  thickness glass sheets with a bulk resistivity range of  $10^{12} - 10^{13} \Omega cm$  at room temperature. These have dimensions of  $2.2 \times 1.5$  up to  $2.2 \times 2.7 m^2$ . The gas gap between the glass plates is filled with a special mixture of hydro-fluorocarbon-134a, argon, and butane-silver. This gas mixture is environmentally friendly and has high detection efficiency.

### 2.3 Belle Trigger and Data Acquisition System (DAQ)

The Belle experiment is designed to operate at a luminosity of  $10^{34} \text{ cm}^{-2}\text{s}^{-1}$  and a beam crossing interval of  $2 \text{ ns}$  [38]. According to these conditions, the rate of physics events is expected at around 100 Hz, with data size around 30 kB/event. Plus there are few hundred Hz of background events which varies with beam condition. Considering these conditions, the Belle Trigger and Data Acquisition System (DAQ) is designed to select events at a rate up to 500 Hz. After the electron positron collision and an event achieving minimum trigger conditions then all sub-detectors are ready to store all the information on that particular event. These trigger conditions helps to reject all unnecessary events and pass important events with high efficiency to the DAQ system for storage and later processing. Many events do not come from electron and positron collisions, but are similar to real collision events. It is important to filter and remove these non-collision events without storing their information. These events mainly come from undesirable interactions between electron and positron beams, collisions of beam particles with residual gas molecules or with the beam pipe, and synchrotron radiation from the beams [39].

Belle has a two level trigger systems composed of a hardware trigger (L1) and software trigger (L3). Figure 2.16 shows a schematic of the hardware trigger system in Belle. All the sub-detector trigger systems are categorized as track triggers and energy triggers which are combined into one main trigger system called Global Decision Logic (GDL) [40]. GDL receives sub-detector signals within  $1.85 \mu\text{s}$  and the final hardware trigger decision comes  $2.2 \mu\text{s}$  after collision. The software trigger stores all the raw data containing all the information from subdetectors. Before storing data the L3 trigger checks all information from the L1 trigger. If L1 information does not belong to Bhabha ( $e^+e^- \rightarrow e^+e^-$ ) or random trigger event categories then L3 quickly checks the reconstruction process and removes events having no track with impact parameter with direction  $|z| < 5 \text{ cm}$  and events with energy less than  $3 \text{ GeV}$  deposited in the ECL. This suppresses a large amount of background and results in a 50% reduction of stored data.

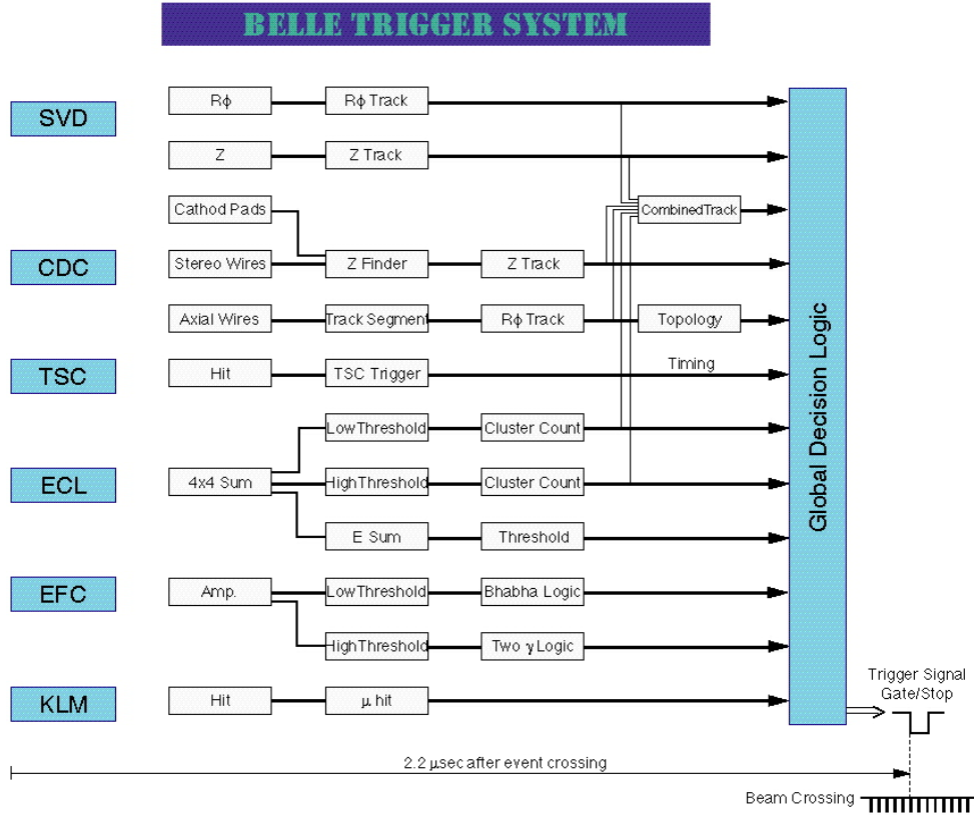


Figure 2.16: Belle trigger system from [8].

The Belle DAQ system is designed to manage and store all signal data from each sub-detector. Figure 2.17 shows the arrangement of the DAQ system. This system contains seven parallel processing sub-systems. Most sub-detectors are capable of measuring energy deposits and signals come out proportional to energy deposits in each sub-detector. The signals are analog and are converted to digital. The conversion is done by Time-to-Digital (TDG) converters in the DAQ system. The SVD uses Flash Analog to Digital Converter (Flash ADC) [41]. After the GDL receives a trigger signal, the event builder processes all data from each sub-detector and converts these detector-by-detector parallel data in to event-by-event data. After the conversion it forwards the event data to an online computer farm and transforms it into the offline event format with background filtering. Finally data is transferred using optical cables from the online computer farm to a data storage system at the KEK computing facility [42].

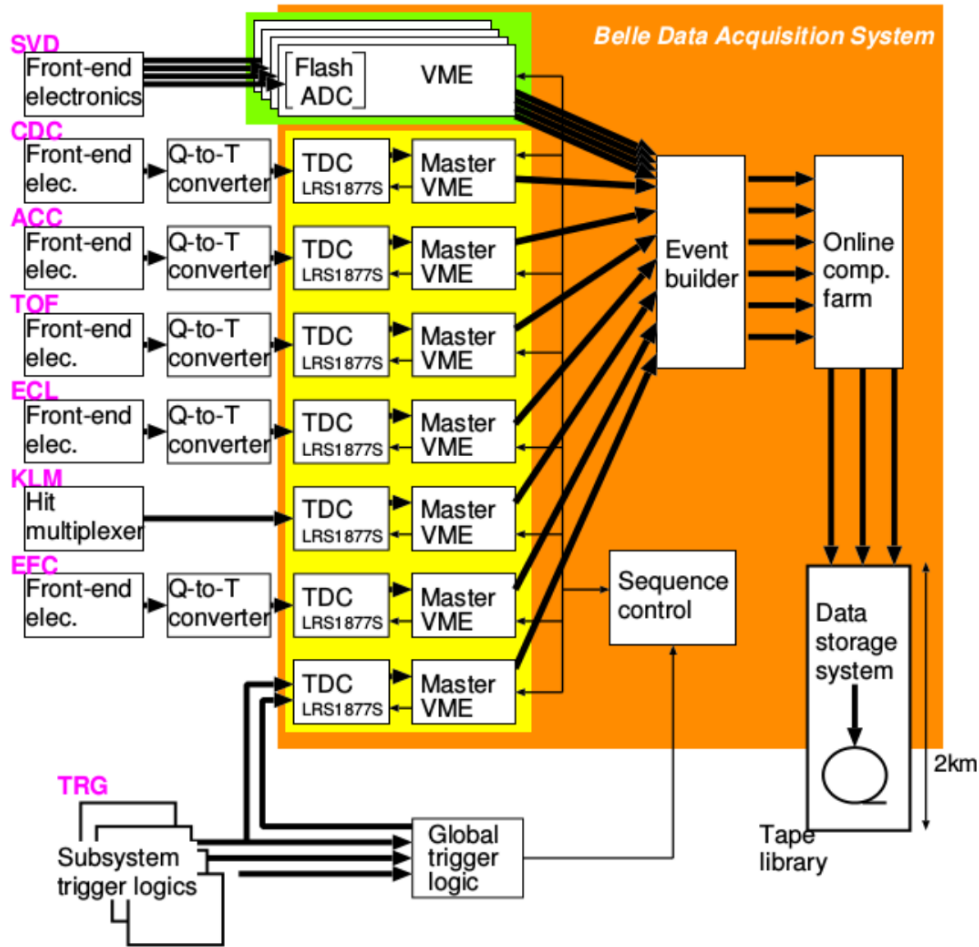


Figure 2.17: Belle data acquisition system [10].

## 2.4 Belle Analysis Software Framework (BASF) and Monte Carlo (MC)

Belle Analysis Software Framework (BASF) is the main software framework used for event processing and offline physics analysis using Belle data. All Belle experiment users can write their own analysis code using Fortran, C, C++, or Python language and run it in the BASF environment. Depending on the analysis, users can import any analysis modules for their code such as “inputMdstList”, “reconstructDecay”, “ntupleFile”, and others. These modules help to read data files, select particle lists, choose variables, add conditions or cut values, and others. Finally the user gets reconstructed files in a ROOT-Data-Analysis format for future analysis. This format is easy to continue analyses deeper with data visualization, optimization, filtering, and others.

Before analyzing real data it is always recommended to perform a Monte Carlo (MC) analysis with knowledge of the experiment [43]. This means all optimizations of the analysis are done with a statistically independent data set before performing it on real data. The Belle collaboration has a detailed MC simulation including detector effects, possible backgrounds, and optimization of selection criteria. MC production follows two procedures of generation and simulation. In generation mode a set of semi-random particles fly from the IP based on physics predictions and kinematics limitations. All the kinematics are controlled by the EvtGen package where PYTHIA 5.7 and JETSET 7.4 [44] are used to model the fragmentation of quarks.

Second the detector response for each generated particle is simulated. This process is done by the GEANT 3 package and a final simulated MC file is produced as a Mini Data Summary Table (MDST) with some additional information on reconstructed particles such as generated momentum, vertex information, and others. These official MC samples look as much as possible like real data. The Belle collaboration generates a large number of MC data sets which are divided in to *streams* where each stream has a number of events equivalent to the luminosity of the Belle experiment. Apart from these official MC samples users can generate their own individual signal samples which can be used for their efficiency calculations.

## CHAPTER 3 ANALYSIS

The B meson has a high mass and thus can decay into many final states. We categorize B-decays based on their final state quark contents such as charmless decays with no charm quark in the intermediate or final state, charm decays with charm quarks in the intermediate or final states, Charmonium decays, etc. This helps analysis as categorized working groups share their ideas and analysis techniques with each other leading to the same goals such as calculating angles of the unitary triangle or measuring CP violation parameters .

B meson decays are dominated by decays to charm and those are dominated by tree level processes. Charmless B-decays have large contributions from penguin processes which have a large opportunity for new physics contributions. The goal of this analysis is to study the charmless three-body decay  $e^+e^- \rightarrow \Upsilon(4S) \rightarrow B^+B^-$  and  $B^+$  or  $B^-$  decays to final state  $K_S^0\pi^+\pi^0$  or  $K_S^0\pi^-\pi^0$  with Belle Full Monte Carlo simulation to develop analysis techniques subsequently applied to Belle data. This chapter describes the study of the decay mode based on an equivalent luminosity of the  $571 \text{ fb}^{-1}$  of simulated data from Belle. The goal is to demonstrate a complete analysis, obtaining a good signal to background ratio for the decay of  $B^\pm \rightarrow K_S^0\pi^\pm\pi^0$  and calculate the branching fraction for this process.

### 3.1 Particle Identification and Event Reconstruction

#### 3.1.1 Data sample

The Belle experiment collected a data sample corresponding to a total integrated luminosity of approximately  $1 \text{ ab}^{-1}$  during the operation period of 1999 to 2010 at various  $\Upsilon$  resonances. Most of the data recorded was at the energy corresponding to the mass of the  $\Upsilon(4S)$ . The  $\Upsilon(4S)$  data was recorded in two detector configurations of the silicon vertex detector: SVD1 (official luminosity  $140 \text{ fb}^{-1}$ ) and SVD2 (official luminosity  $571 \text{ fb}^{-1}$ ) [45]. In this analysis I used simulated SVD2 data corresponding to exp 31 to 65 containing approximately 620 million pairs of  $B\bar{B}$  mesons. Table 3.1 shows the detailed information on the luminosity for each experiment number and how many events of each type of event are

expected for each experiment. Table 3.2 shows an example (for experiment 31) of the MC stream 0 data sets used in this analysis.

Table 3.1: Summary of the luminosity and number of events in each experiment [13]

Exp No	Luminosity $fb^{-1}$	Number of MC Events			
		Charged	Mixed	Charm	uds
31	17.725	9278486	9278483	22133172	35582936
33	17.508	9473597	9473593	22598090	36330562
35	16.691	9194075	9194074	21931344	35258660
37	60.909	33181995	33181993	79151036	127249999
39	41.157	23083585	23083591	55062602	88523407
41	58.752	31243163	31243161	74525788	119814238
43	56.206	29763451	29763443	70996068	114139596
45	12.946	6972626	6972626	16632145	26739289
47	37.205	20015809	20015813	47744637	76758509
49	27.024	14535659	14535658	34672643	55742786
51	39.237	21130003	21130008	50402720	81031726
55	72.088	38841213	38841208	92649805	148951973
61	34.095	18624949	18624948	44427294	71425095
63	32.858	17528959	17528960	41812691	67221743
65	37.751	20259429	20259430	48325746	77692728
<b>Total</b>	<b>562.152</b>	<b>303126999</b>	<b>303126989</b>	<b>723065781</b>	<b>1162463247</b>

Table 3.2: MC stream 0 file Location sample for experiment 31 [13]

MC Type	MC location in Belle storage
Charged	/group/belle/bdata_b/mcprod/dat/e000031/evtgen/charged/00/all/0127/ on_resonance/[02-17]
Mixed	/group/belle/bdata_b/mcprod/dat/e000031/evtgen/mixed/00/all/0127/ on_resonance/[00-11]
Charm	/group/belle/bdata_b/mcprod/dat/e000031/evtgen/charm/00/all/0127/ on_resonance/[02-17]
uds	/group/belle/bdata_b/mcprod/dat/e000031/evtgen/uds/00/all/0127/ on_resonance/[02-17]

First I use  $\Upsilon(4S)$  full Monte Carlo (Full MC) simulated data. I used the dedicated signal sample for  $B^\pm \rightarrow K_s^0 \pi^\pm \pi^0$ , and for background samples I used the  $uds(\Upsilon(4S) \rightarrow u\bar{u} + d\bar{d} + s\bar{s})$ ,  $c\bar{c}$ , mixed ( $\Upsilon(4S) \rightarrow B^0 \bar{B}^0$ ) and charged ( $B^\pm$  decays) samples corresponding to  $571 fb^{-1}$  of integrated luminosity. The  $uds$  ( $u\bar{u}$ ,  $d\bar{d}$ ,  $s\bar{s}$ ) sample is chosen as representative of the continuum background data. All Belle full MC background samples are listed in the Belle Generic MC page [46].

Signal Full MC samples are generated using EvtGen for the simulation of B meson decays and GSIM(GEANT3) for the simulation of the Belle detector. Two different sets of signal MC were generated: the first had 5 million events generated as direct decay,  $B^\pm \rightarrow K_s^0 \pi^\pm \pi^0$ . The second sample had  $10^5$  events generated including expected intermediate resonances of  $K^{*+}(892)$ ,  $K^{*0}(892)$ ,  $K_0^*(1430)$ ,  $K_2^*(1430)$ , and  $\rho^+(770)$ . All output files are stored as mdst (mini data summary table) file format for reconstruction process.

All Belle data are *skimmed*. Skimming is the process whereby a loose set of selection criteria are applied to the data sets to produce smaller data sets. Analysts run their analysis over skimmed data sets not the full data sets. This analysis uses the HadronB(J) skim, the most commonly used skim for analyses with hadrons.

### 3.1.2 Monte Carlo Simulation

Before looking at the experimental data, all groups test their methods using full MC (described in the Section 2.4) to develop robust, unbiased analysis methods. It is important to have all selection criteria developed using MC studies, and tested on control samples (experimental data statistically independent from the data used for the measurement) where possible. In this analysis it is important to study possible background contributions and optimize selection criteria. For this purpose full MC simulations are available to all Belle collaborators. This full MC is generated with the full detector modeled, including effects such as performance, efficiency, threshold values, detector physics, and others. All the kinematics calculations are done by the generator package EvtGen [47] with the modeling of hadronization done by PYTHIA 5.7 and JETSET 7.4 [48] generators.

After generation every event goes through simulation of the detector response. This process is done by the GEANT3 [49] package and final output is stored in the mdst format. This output looks exactly as experimental data but it contains some additional underlying information such as what is each particle's parent particle, generated energy, momentum etc. These full MC are generated according to stable conditions of the experiment and are called streams. Apart from these simulations, Belle collaborators are able to generate their own (signal) decay channels with their own number of events according to the detector performance and parameters. This enables analysts to do signal analysis and calculate effects such as signal reconstruction efficiency.

### 3.1.3 Data and MC Reconstruction

Belle II software called basf2 is written in C++. Packages in basf2 contain C++ modules to manipulate data. Analysts can build particles from primitive objects and they can calculate physics quantities, and apply cuts using basf2. For my complete analysis full MC was reconstructed using basf2, release-03-02-04, software. The reconstruction process takes

a very long time to run on local computers because data samples contain billions of events. Therefore parallel processing is highly recommended. The Belle grid provides a distributed computing infrastructure that can be used for such processing and I use it heavily for reconstruction of both signal and background events.

The framework uses “steering files” written in python to control the settings used by each analyst for reconstructing data and MC. I wrote a python script to manage the reconstruction process using Belle II software tools to reconstruct Belle MC and data. I use the `b2biiConversion` package and `b2biiMonitors` to convert and monitor the Belle to Belle II process. For the particle list in the reconstruction process, standard Belle particle definitions are used to create the particle lists `K_S0:mdst pi+:all pi0:mdst` are selected. This builds representations of all  $K_S^0$ ,  $\pi^+$ ,  $\pi^-$ , and  $\pi^0$ .

Precision reconstruction of particles from daughters to parent particles is very important. Normally in particle physics decay chains reconstruction starts from daughter particles, going from vertex to vertex and ending with the head of the decay tree. I use `TREEFITTER` for my reconstruction. It fits the entire decay channels using a Kalman filter technique. `TREEFITTER` is a global vertex fitter, fitting the entire decay channel simultaneously. This method is fast, has high background rejection, and almost importantly, it can handle decay chains containing neutral final state particles.

The most challenging aspect of this analysis is background rejection to obtain good signal to background. It is important to study a number of useful variables like number of candidates, beam constrained mass ( $M_{BC}$ ), energy difference between B meson and beam energy ( $\Delta E$ ), and others. Many such kinematic variables are available in the `ntupleFile` package [50].

### 3.1.4 Continuum and B related Backgrounds

I consider two types of backgrounds called continuum and B related backgrounds.  $B$  backgrounds have two categories called generic  $B$  (mediated by  $b \rightarrow c$ ) and rare  $B$  (me-

diated by  $b \rightarrow u, d, s$ ). The major background comes from continuum events  $e^+e^- \rightarrow q\bar{q}$  where  $q = u, d, s, c$ . It is necessary to find a method to remove these backgrounds. Therefore we need to understand the behavior of these events and study the geometric properties and spatial relations of these events compared to  $B\bar{B}$  signal events. The  $\Upsilon(4S)$  ( $e^+e^- \rightarrow \Upsilon(4S) \rightarrow B\bar{B}$ ) mass is slightly above than  $B\bar{B}$  pair production in the center of mass frame(CMF). Therefore the B mesons are created almost at rest and the decay products fill the  $4\pi$  solid angle. Continuum backgrounds come from electron positron collision( $e^+e^- \rightarrow q\bar{q}$ ). These light quarks have high momentum and are likely to fly back to back forming two jets of light hadrons. Using these two different event shapes, I can differentiate and suppress background events.

## 3.2 Selection Criteria

### 3.2.1 Initial Event Selection

We reconstruct decays of  $B^\pm \rightarrow K_S^0 \pi^\pm \pi^0$  in the full MC samples using b2bii and basf2 software. As mentioned in the Section 3.1.3 standard particle lists for the particles  $K_S^0$ ,  $\pi^+$  and,  $\pi^0$  are used and all possible combinations of these particles are reconstructed subject to very basic selection criteria to give us candidates for our decay  $B^\pm \rightarrow K_S^0 \pi^\pm \pi^0$ . When using the standard particles list, I use loose selections and afterwards I can look at the distributions and place tighter selection criteria. After creating both signal and background analysis root files, basic or initial selections are applied to the data in order to see how they affect the number of events.

To reduce the number of background events I use basic cuts to obtain a good signal to background ratio. The basf2 reconstruction contain loose requirements on  $M_{BC}$  and  $\Delta E$  to reduce the number of candidates stored. Considering continuum event geometry we added extra loose selections on continuum variables  $\cos\text{TBTO}$  (cosine of the angle between the thrust axis of the B and the thrust axis of the rest of events) and  $\cos\text{TBz}$  (cosine of the angle between the thrust axis of the B and the z-axis) [51]3.2.2. The initial selections are loose and

are intended to mirror selections used in skimming and I can tighten these at a later stage of my analysis. The very initial selections used are listed below before the multivariable analysis and optimization.

The selection criteria include two D vetos. After applying the other selection criteria there is still a relatively large number of background events arising from D decays as seen in Figure 4.2 in Section 4.1 . These all occur in bands centered on the D mass in the Dalitz plot. Since these regions are relatively narrow and in these regions the D background swamps any signal I remove these regions out.

- Initial processing with a basf2 reconstruction steering file: selections applied here:  
 $5.24 < M_{BC} < 5.29$ ,  $abs(\Delta E) < 0.5$ ,  $0 < cosTBTO < 0.9$  and,  $0 < cosTBz < 0.85$
- $GoodK_S^0 = 1$  to select well reconstructed  $K_S^0$
- $M_{BC}$ :  $5.275 < M_{BC} < 5.29$
- $\Delta E$ :  $-0.1 < \Delta E < 0.05$
- Chi Probability:  $ChiProb > 0.5$  (Probability of the vertex fit result)
- $M_{K_S^0}$ :  $0.49 < M_{K_S^0} < 0.51$
- $E_{\pi^0}$ :  $0.7 < E_{\pi^0}$
- $D^\pm$  veto:  $M_{K_S^0\pi^+}$ :  $M_{K_S^0\pi^+} < 1.70788$  or  $M_{K_S^0\pi^+} > 1.9924$
- $D^0$  veto:  $M_{K_S^0\pi^0}$ :  $M_{K_S^0\pi^0} < 1.70788$  or  $M_{K_S^0\pi^0} > 1.9924$
- I select randomly one of the candidate in events of multiple candidates.

The candidate selection is equivalent to an almost random best candidate selection. For the purposes of selection flow I select one candidate per event to show the selection criteria flow in terms of number of events rather than number of candidates. Figure 3.1 shows the

number of candidate varies after all selection criteria including multivariable analysis but without candidate selection. I randomly select one candidate per event.

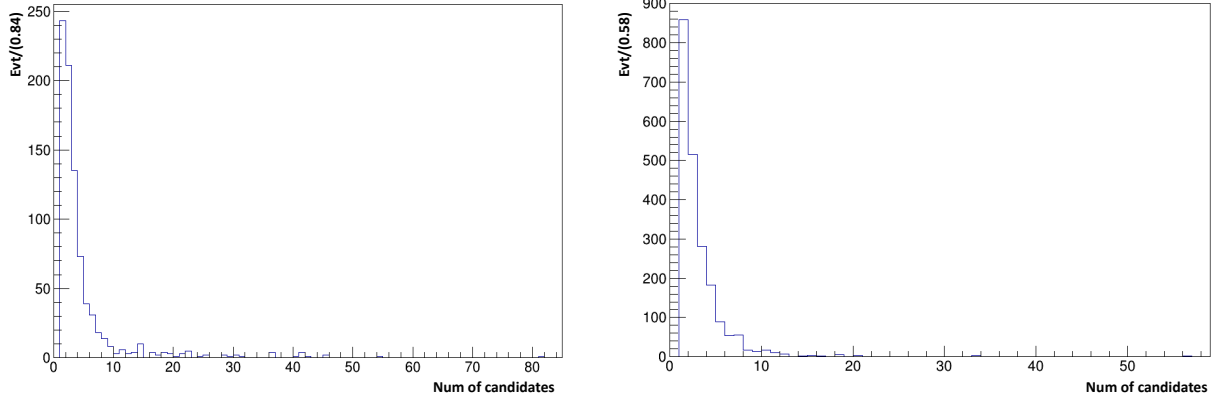


Figure 3.1: Background(Left) and Signal(Right) candidate distributions

After event selection, it is very important to normalize generated full MC signal events in  $571 \text{ fb}^{-1}$  of luminosity to compare the number of background events in the cut flow table in Chapter 4, background estimation as in the Section 3.3 and also to calculate branching fraction (BF) as in the Equation 3.13.

Calculation of normalization factors for the full signal MC needs the following inputs: the number of  $B^\pm$  events in a collision (taken to be roughly 309.81 million from the charged background sample) and the branching fraction of the  $B^\pm \rightarrow K_s^0 \pi^\pm \pi^0$  mode, which we take to be  $5 \times 10^{-5}$  [52]. Equation 3.1 presents this calculation.

$$\begin{aligned}
 Full\ MC\ Signal_{Norm} &= (\text{number of } B^\pm \text{ events}) \times (\text{branching fraction}) \times (\text{cut efficiency}) \\
 &= (3.0981 \times 10^8) \times (5 \times 10^{-5}) \times (Efficiency)
 \end{aligned}
 \tag{3.1}$$

where *Efficiency* is

$$Efficiency = \frac{(Number\ of\ events\ (After\ selection\ criteria))}{(Number\ of\ events\ (Before\ reconstruction))}. \quad (3.2)$$

The beam-constrained mass ( $M_{BC}$ )

$$M_{BC} = \sqrt{E_{beam}^2 - P_B^2} \quad (3.3)$$

peaks sharply around the B meson mass for signal events, where  $P_B$  is the momentum of the  $B$  meson in the CMS (Center of Mass System) and  $E_{beam}$  is half of the CMS energy. Normally  $B^\pm$  has a very small momentum, almost zero. Similarly the  $\Delta E$  variable is

$$\Delta E = E_B - E_{beam} \quad (3.4)$$

The  $\Delta E$  variable always peaks around zero for correctly reconstructed signal events.

Initially events can contain many reconstructed  $B^\pm$  candidates which pass the loose selections. At this stage in the analysis, there are some low quality signal events coming from poorly reconstructed  $\pi^0$  and  $K_S^0$ . Therefore I place an additional initial cut on  $E_{\pi^0}$  which is very helpful to remove both background and poorly reconstructed signal events. Most of the poorly reconstructed events look like signal but actually they are mis-reconstructed events called self cross feed (SCF). This is very common in both signal MC and data. There is a substantial amount of events in SCF and because of that it has separated shape. SCF events are treated as in both initial selection and MVA analysis but in the background estimation (Section 3.3) and Laura++ fitting (Section 3.6) I treat SCF as a separate component to obtain better results.

### 3.2.2 Continuum Suppression and Multi Variate Analysis (MVA)

After processing the continuum background files, multi variate analysis is a very useful tool to reduce continuum background and keep signal events. For this purpose I use the built-in TMVA (Toolkit for Multivariate Analysis) package in ROOT [53]. This package contains a number of different statistical analysis methods from which I choose the most effective. According to the geometry there are a number of variables to separate the signal events from the continuum background. Variables which help to separate signal and continuum events are [50]

- ThrustB : Magnitude of B thrust axis
- ThrustO : Magnitude of RoE (Rest of Event) thrust axis
- CosTBTO : Cosine of the angle between the thrust axis of the B and the thrust axis of the RoE
- CosTBz : Cosine of the angle between the thrust axis of the B and the z-axis
- KSFw : Kakuno-Super-Fox-Wolfram variables
- CLEO : Cleo cone 1 - 9 variables

Individually these variables are not very useful; they have minimal separation power. Rather than looking at these variables and having individual selections, I can take multiple variables into account simultaneously. This multivariate analysis can be much more powerful than having selections on variables separately and can be a much more efficient way to keep signal events while reducing continuum backgrounds. Several methods or statistical models are considered as MVA techniques such as *Cut optimization* , *likelihood* , *Nearest-Neighbor* , *Neural Networks* and then I can choose the method which shows the best performance for the analysis.

For MVA analysis two samples from both signal and background are required, this allows me to do separate training and testing of MVA methods to check that I do not over-train the

method. Over-training is when the method is focused on specific details of the training data rather than general trends. An over-trained method will have a much better performance on the training data than the testing data. I tried a number of analysis methods, their results shown in Figure 3.2. This plot shows background rejection versus signal efficiency for the MVA models which TMVA applied to the full MC signal and background samples.

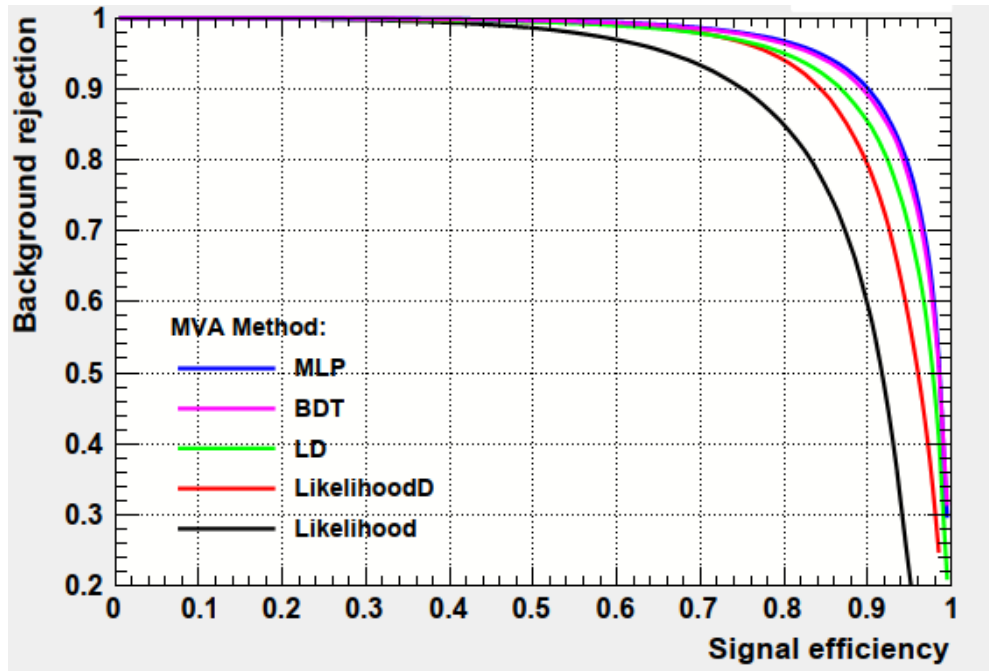


Figure 3.2: Background rejection vs. signal efficiency generated by TMVA for several MVA methods.

### 3.2.3 Boosted Decision Trees (BDT)

In high energy physics (HEP) experiments, it is usually necessary to select signal events with specific selections, out of a large number of background events for study. A boosted decision tree (BDT) is a modern method of multivariate data analysis. First consider a decision tree (DT). By using several variables we can build a tree for example as in Figure 3.3. There are many possible ways to build a tree. It is important to go through all variables and find the best variables and values to split events in to smaller groups of events called nodes. Final nodes are called leaves and leaves must contain at least a minimum number of

events. If we have an equal amount of signal and background training events and more than  $1/2$  of the events in a leaf are signal, it is a signal leaf, otherwise it is a background leaf [54].

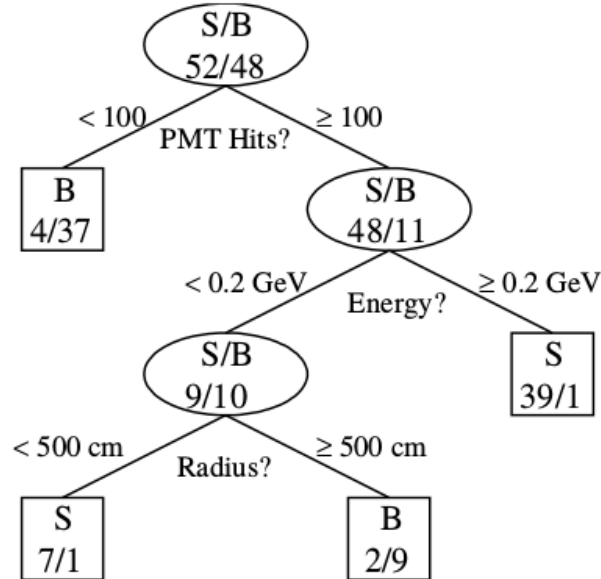


Figure 3.3: Example of a decision tree.

Some signal events appear in a background leaf or background events in a signal leaf because of misclassification. There is a disadvantage of DT in that they are not stable; a small change or fluctuation in the input data can make a large difference. A solution to this is to use boosted decision trees, so that the weighted average over a number of trees is insensitive to fluctuations. This is done by building and optimizing new trees and re-weighting the trees based on their performance. There are several boosting algorithms for changing weights such as

- AdaBoost (Adaptive Boosting),
- Epsilon Boost,
- Epsilon-Logit Boost,

- Epsilon-Hinge Boost,
- Logit Boost,
- Gentle AdaBoost.

In TMVA, Adaptive Boosting is a common method to use for a BDT. For this analysis, the BDT method performed best on the MC throughout multiple iterations of improving the MVA. Figure 3.2 shows the BDT method was closest to 90% background rejection and 90% signal efficiency. multilayer perceptron (MLP) method also performed similar to the BDT, but when tested with Belle II full MC, the BDT method shows best performance. After an analysis done using the BDT method, a new variable, the BDT output, is created for both signal and background events. Figure 3.4 shows the distribution of the BDT output variable for signal and background events.

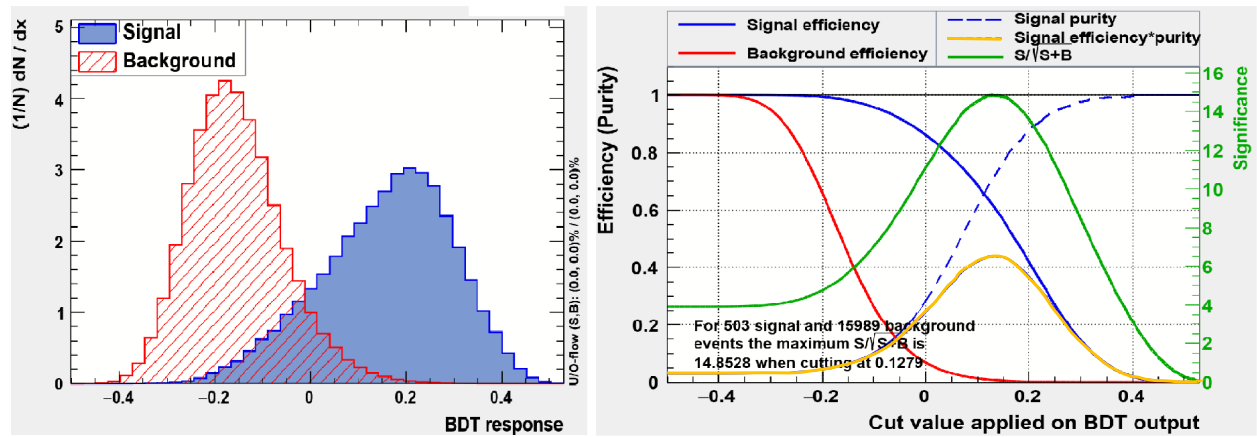


Figure 3.4: The left histogram shows the BDT variable for 1000 events of signal and  $u\bar{u}$  background samples. The right plot shows BDT cut optimization for expected signal and background events.

TMVA has an option to see the best for a given number of signal and background events together with efficiency as shown in Figure 3.4. In this plot we use 503 signal events and 15989 background events, which is approximately the expected number of signal and background events normalized to an integrated luminosity of  $571 \text{ fb}^{-1}$ . The best cut value will change as we change the number of events. A figure of merit (FoM)

$$\begin{aligned}
FoM &= (\text{num of signal events}) / \sqrt{(\text{num of signal events}) + (\text{num of background events})} \\
&= \frac{S}{\sqrt{S+B}},
\end{aligned}
\tag{3.5}$$

is used here to determine what is the best selection value for the BDT output to reject background. According to the Equation 3.5 the optimized selection value is 0.1279 and I round it off to 0.13.

### 3.3 Full MC and Data driven Background estimation

After applying the selection criteria we obtain the signal and background estimates shown in Table 4.1 and we know the expected background events from each section in the signal dominant region ( $5.275 < M_{BC} < 5.29$ ). Figure 3.5 shows the combination of all signal and background events. Figure 3.5(A) shows the  $\Delta E$  versus  $M_{BC}$  distribution. This plot includes all selection criteria except  $M_{BC}$  and  $\Delta E$  selections. We can see a high density area around signal region. Figure 3.5(B) is the 1D projection of  $M_{BC}$  corresponding to Figure 3.5(A). Figure 3.5(C) shows the event distribution after all selection criteria and Figure 3.5(D) is the 1D projection of  $M_{BC}$ .

Figure 3.6 shows the distribution of all signal and background events with all selection criteria except  $M_{BC}$  selection ( $5.275 < M_{BC} < 5.29$ ). I used 4 background fitting methods to estimate the number of background (continuum and B related) events in the signal region by fitting Figure 3.6.

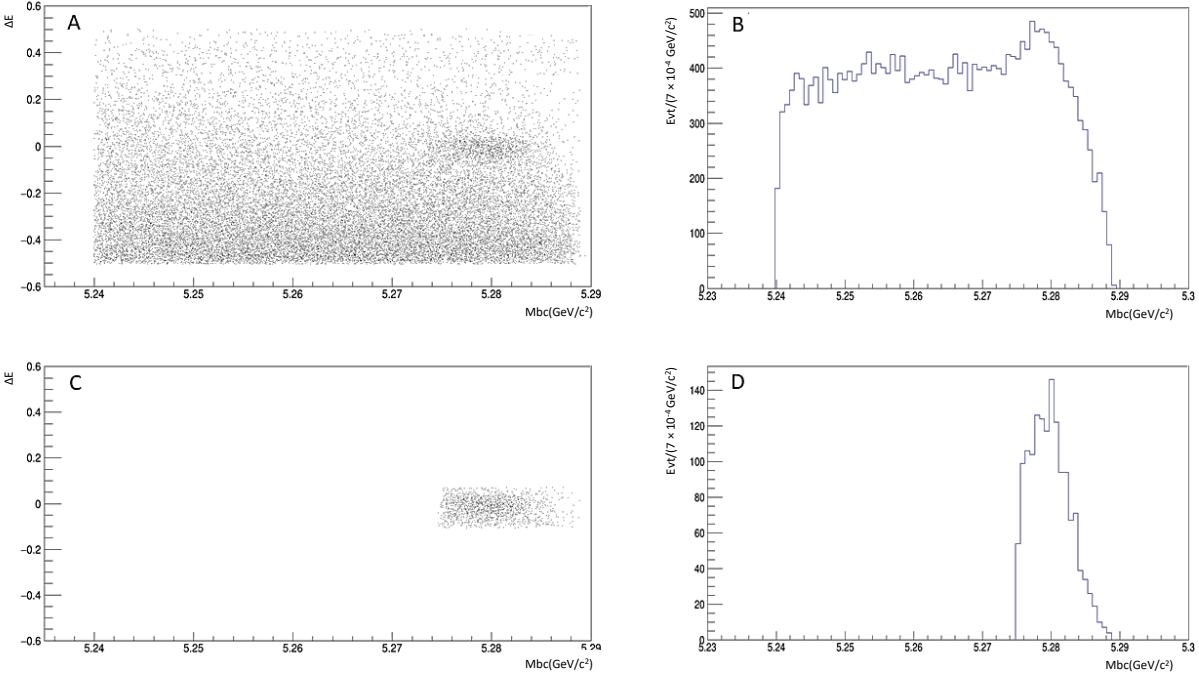


Figure 3.5: Full MC: (A)  $\Delta E$  vs  $M_{BC}$  distribution without  $M_{BC}$  and  $\Delta E$  selection. (B) 1D projection of  $M_{BC}$  distribution without  $M_{BC}$  and  $\Delta E$  selection. (C)  $\Delta E$  vs  $M_{BC}$  distribution with  $M_{BC}$  and  $\Delta E$  Selection. (D) 1D projection of  $M_{BC}$  distribution with  $M_{BC}$  and  $\Delta E$  selection.

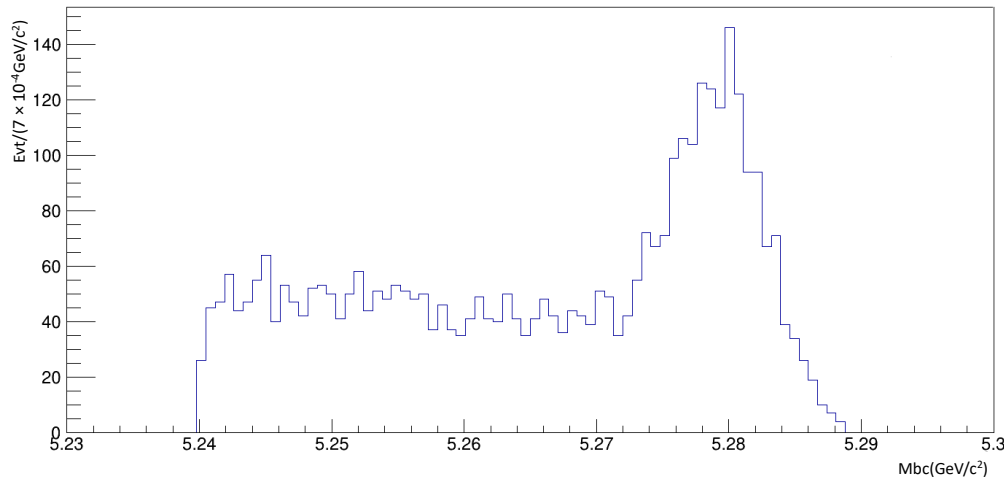


Figure 3.6: Unlike Figure 3.5 B, this figure includes the  $\Delta E$  cut.

- Method 1

As shown in Figure 3.7 is the entire full MC distribution fitted using an ARGUS function [55]. I fit the distribution in the range 5.24 to 5.27 and extrapolate to the

region 5.27 to 5.29 and calculate the area under the ARGUS function (red line) to estimate the number of background events.

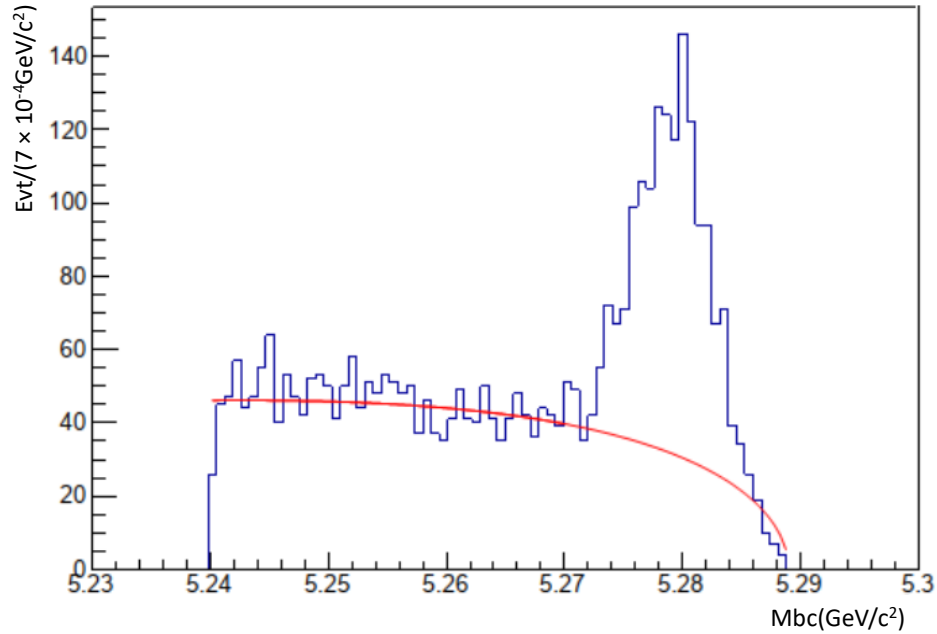


Figure 3.7: Method 1:  $M_{BC}$  distribution Fit with ARGUS function

- Method 2

As shown in Figure 3.8 the total distribution is fitted in the range 5.24 to 5.29, using combined function (red line) featuring a double GAUSSIAN (magenta line) to represent the signal (including SCF) and an ARGUS function (blue line) to represent the backgrounds. The number of background events is estimated from the area under the ARGUS function in the range 5.275 to 5.29. Compared to method 1, this method requires additional modeling of the shape of the signal distribution.

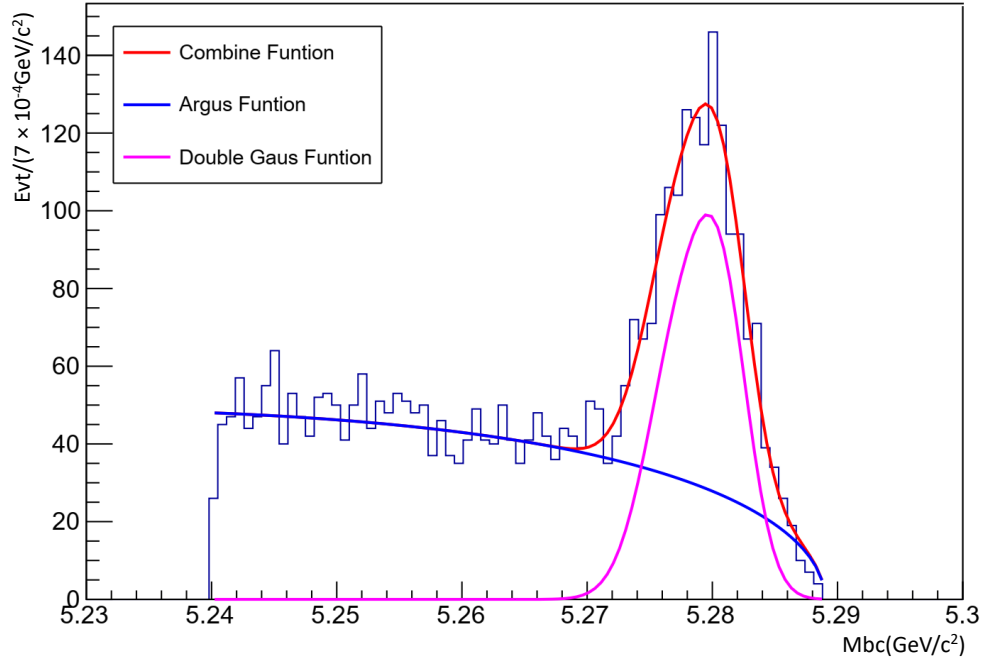


Figure 3.8: Method 2:  $M_{BC}$  distribution Fit with ARGUS and double GAUSSIAN function

- Method 3

As shown in Figure 3.9 this method also involves fitting the full distribution in the range 5.24 to 5.29. The area under the (blue) ARGUS function in the range 5.275 to 5.29 is used to estimate the number of background events. The red line represents the total fit. The difference between this model and the previous model, is that this model modifies the function representing the signal and SCF to include an additional "tail" arising from the self cross feed. This tail can be seen in Figure 3.10; now the signal and SCF distribution is modeled as a double GAUSSIAN plus a small ARGUS function for the tail. As both the signal and background functions now contain an ARGUS function, in order for the fit to work, it is necessary to constrain the parameters of the ARGUS part of the signal distribution based on the values of the parameters by fitting the tail of the distribution in Figure 3.10 alone.

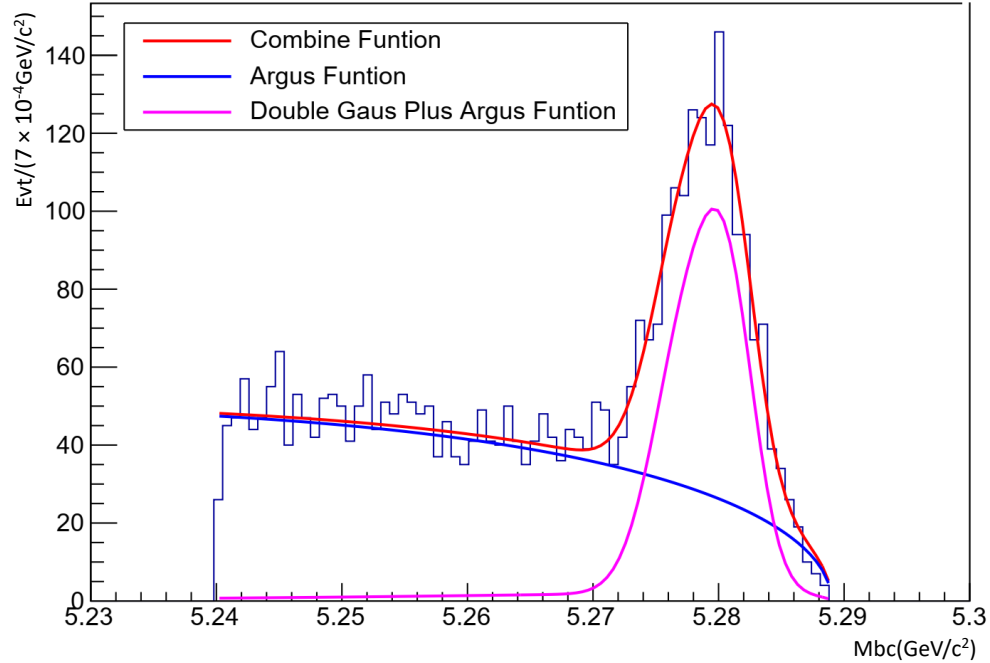


Figure 3.9: Method 3:  $M_{BC}$  distribution fit with ARGUS function and combination of ARGUS and double GAUSSIAN function

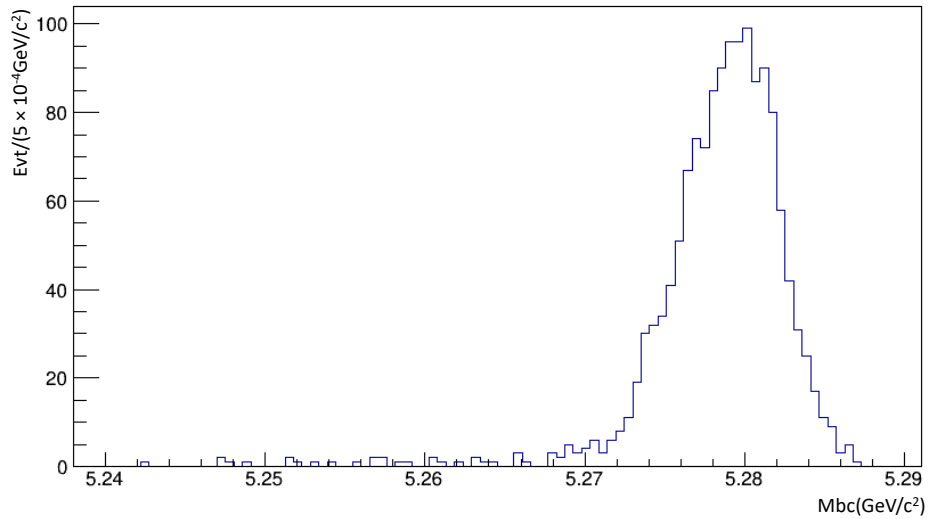


Figure 3.10: Signal + SCF  $M_{BC}$  events distribution tail in the background region

- Method 4

As shown in Figure 3.11, I fit a combined function in the range 5.24 to 5.27 - the combined function (red line) consists of two parts, an ARGUS function (green line)

representing the background, and a second ARGUS function (blue line) representing the tail of the SCF distribution. I obtain the estimate of the number of background events from extrapolating the background ARGUS function and calculating the area under this function in the range 5.275 to 5.29. This method has the advantage that it does not involve having to model the whole of the signal distribution, and apart from a very small contribution of the SCF tail, relies only on fitting the background distribution.

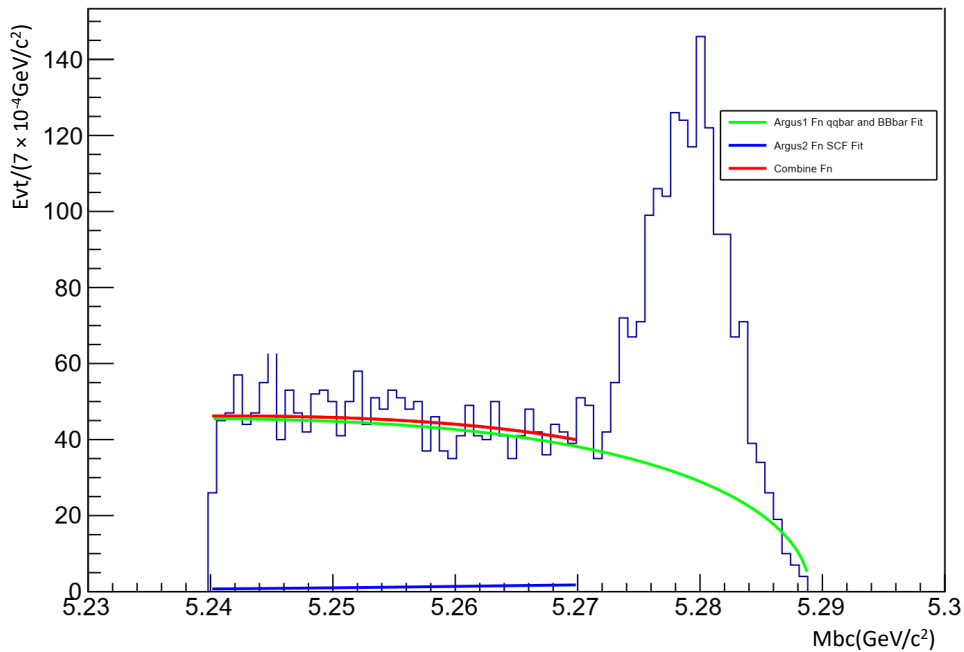


Figure 3.11: Method 4:  $M_{BC}$  distribution Fit with two ARGUS functions

When comparing the performance of the methods, the estimate of the number of background events contained from method 4 shows the best agreement with the number of events from the MC, and as it does not rely on fitting the signal as well as the background, I have selected this method for my analysis. Full results from fitting with these methods are shown in Section 4.2.1.

### 3.4 Dalitz analysis using Laura++

#### 3.4.1 Kinematics of three body decays

There are many possible ways for a  $B$  meson to decay into a three bodies via intermediate two body decays. In these decays I can analyze what are the intermediate resonances and extract information about them including phase, amplitude, and fit fraction values for each separate decay path. Figure 3.12 shows some possible tree and penguin Feynman diagrams for the process of  $B^\pm \rightarrow K_s^0 \pi^\pm \pi^0$ . Here only the  $b$  quark changes its flavor. As shown in Figure 3.12(C) the  $u$  quark can be generated from vacuum like the  $d$  quark without gluon or photon coupling therefore, this process can have many Feynman diagrams contributing and be sensitive to new physics contributions.

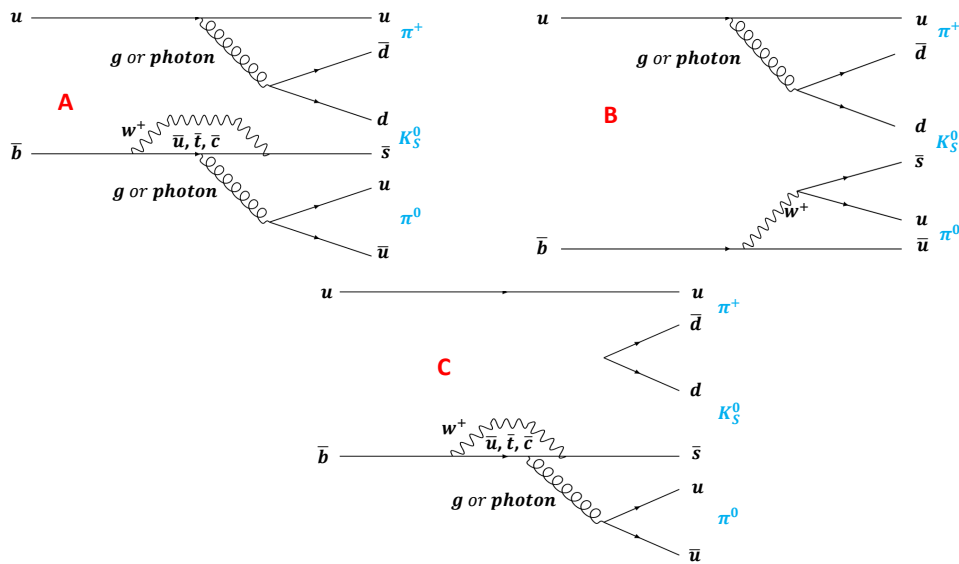


Figure 3.12: Feynman diagrams contributing to  $B^\pm \rightarrow K_s^0 \pi^\pm \pi^0$ . (A) and (C) are penguin level diagrams and (B) is tree level diagram

It is important to have a good understanding of the kinematics of the three body decay. The particles created in the final state must have a total invariant mass equal to the mass of the decaying particle. Unstable particles often have multiple ways to decay. Each decay process has its own associated probability. The particles in the final state may themselves be unstable and subject to further decay. In the three body decay shown in the Figure 3.13,

assume the parent mass and momentum are  $M$  and  $\underline{P}$  and daughter particles masses and momenta are  $(m_1, \underline{p}_1)$ ,  $(m_2, \underline{p}_2)$ ,  $(m_3, \underline{p}_3)$ .

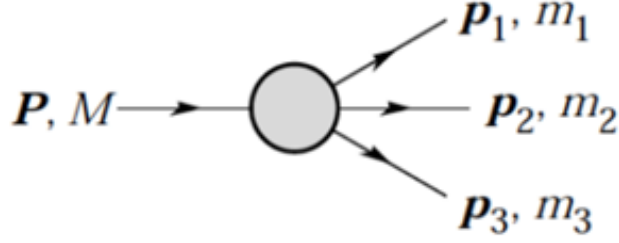


Figure 3.13: Three Body decay of parent particle to daughter particles [11].

Then three intermediate resonance masses can be written as

$$m_{ij}^2 = p_{ij}^2 = (\underline{p}_i + \underline{p}_j)^2 \quad (3.6)$$

where  $i, j = 1, 2, 3$ . All these squared masses of intermediate resonances are linearly dependent. According to

$$m_{12}^2 + m_{13}^2 + m_{23}^2 = M^2 + m_1^2 + m_2^2 + m_3^2 \quad (3.7)$$

any pair of squared masses can be used to specify the kinematics of the decay can be used to calculate the decay probability as given by the square of the invariant amplitude  $|\overline{\mathcal{M}}|^2$  shown in

$$d\Gamma = \frac{1}{(2\pi)^3} \times \frac{1}{32M^3} \times |\overline{\mathcal{M}}|^2 dm_{12}^2 dm_{23}^2 \quad (3.8)$$

where  $\mathcal{M}$  is the matrix element of the decay process. If the invariant amplitude is constant, a scatter plot of  $m_{13}^2$  ( $X$  axis) and  $m_{23}^2$  ( $Y$  axis) will be uniformly populated. A plot of  $m_{ij}^2$  vs  $m_{ik}^2$ , is called a Dalitz plot where  $i, j, k, = 1, 2, 3$ . Non-uniformity in the population of the Dalitz plot gives information on intermediate state resonant contributions to the final state decay. For example Figure 3.14 clearly shows resonance bands within the plot from  $B^\pm \rightarrow K_S^0 \rho^\pm(770)$ ,  $\rho^\pm(770) \rightarrow \pi^+ \pi^0$ .

## Dalitz Plot $B^\pm \rightarrow K_S^0 \pi^\pm \pi^0$

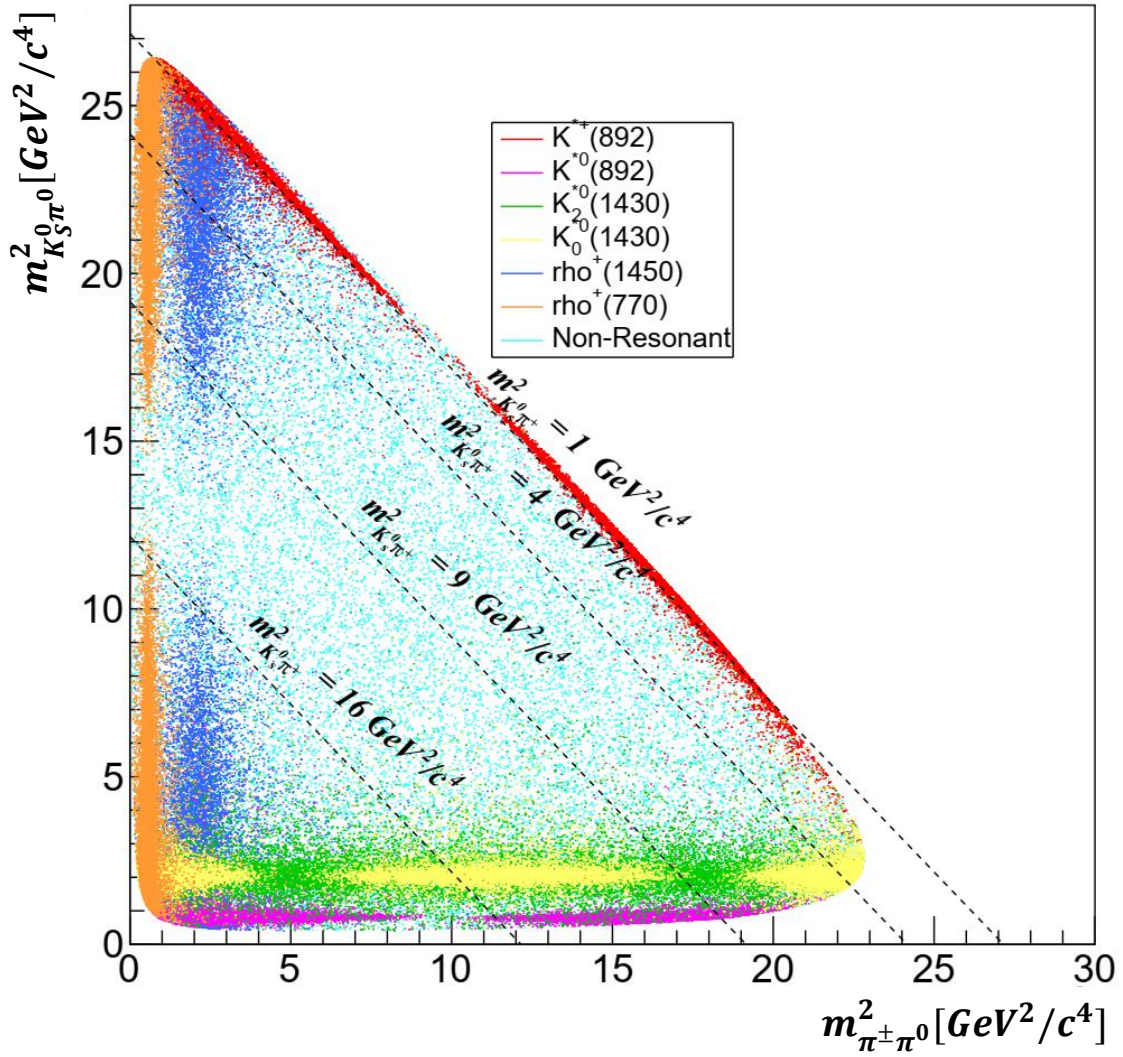


Figure 3.14: Simulated Dalitz plot for  $B^\pm \rightarrow K_S^0 \pi^\pm \pi^0$  with intermediate resonances.

### 3.4.2 Kinematic boundaries of a Dalitz plot

Dalitz plot boundaries depend on kinematic limits of the daughter particles. As shown in Figure 3.15 the edges are determined when the momentum of each of the daughter particles becomes zero in the rest frame for the decaying particle.

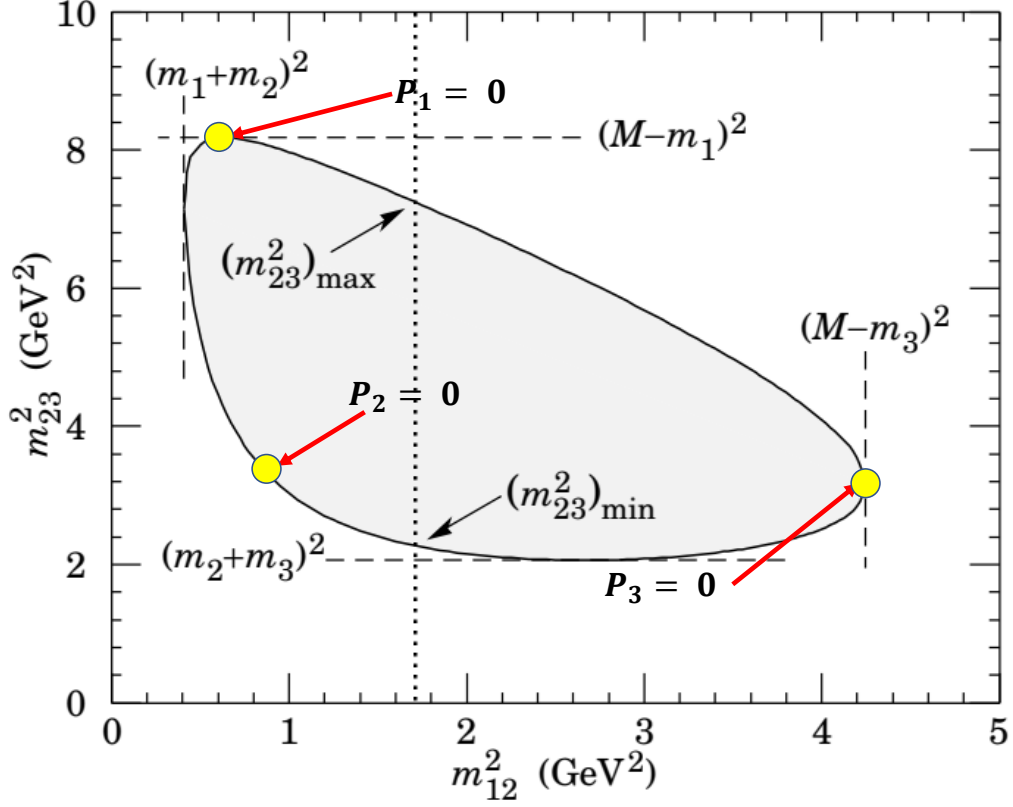


Figure 3.15: Dalitz plot boundaries [11]

These boundaries can be determined using two points of the Dalitz plot coordinates [11] represented by  $(m_{23}^2)_{max}$  and  $(m_{23}^2)_{min}$  as in

$$(m_{23}^2)_{max} = (E_2^* + E_3^*)^2 - \left( \sqrt{E_2^{*2} - m_2^2} - \sqrt{E_3^{*2} - m_3^2} \right)^2 \quad (3.9)$$

and

$$(m_{23}^2)_{min} = (E_2^* + E_3^*)^2 - \left( \sqrt{E_2^{*2} - m_2^2} + \sqrt{E_3^{*2} - m_3^2} \right)^2. \quad (3.10)$$

According to the Figure 3.15, minimum and maximum values for  $m_{12}^2$  are  $(m_1 + m_2)^2$ ,  $(M - m_3)^2$ . For  $m_{23}^2$  the corresponding values are  $(m_2 + m_3)^2$ , and  $(M - m_1)^2$ .

### 3.4.3 Introduction to Laura++

Likelihood Analysis Unbinned Reconstruction of Amplitudes (Laura++) is a software package design for three body decays in the C++ programming language. The package can be generalized to Dalitz plot analysis from any parent particle to three daughter particles [56]. It can generate Toy MC according to given resonances, and apply efficiency maps, and background maps. Toy MC does not include full detector modeling and simulations. It uses different line shapes (Simple Breit-Wigner, Relativistic Breit-Wigner, flatter or coupled-channel Breit-Wigner, and others.) to generate events [57]. These events are generated using the invariant square masses (e.g.  $m_{13}^2, m_{23}^2$ ) within the Dalitz space. Amplitudes, phase values, and fit fractions can be calculated for each resonance based on given line shapes. The amplitude and phase values are input values to the Toy MC generation and affect Dalitz plot distribution. Finally events are accepted or rejected by comparing generated event amplitude, phase values and calculated maximum amplitude and phase values for each resonance and turned into an efficiency map.

Laura++ is capable of fitting both MC and data and uses TMinuit [56] for minimization. This fitting process is a maximum likelihood method. It varies the parameter values in a systematic fashion until the function reaches its maximum and then extracts the parameter value which give the highest likelihood value. Laura++ minimizes the negative log likelihood (NLL) for the same effect [56].

The likelihood functions are written with a signal contributions, continuum, and  $B$  related background contributions as

$$\begin{aligned}
 \mathcal{L}_n(x, y) = & (1 - f_{q\bar{q}} - f_{B\bar{B}}) \frac{|\sum_{i=1}^N a_i g_i(x, y)|^2 \epsilon(x, y)}{\int \int_{DP} |\sum_{i=1}^N a_i g_i(x, y)|^2 \epsilon(x, y) dx dy} \\
 & + f_{q\bar{q}} \frac{Q(x, y)}{\int \int_{DP} Q(x, y) dx dy} \\
 & + f_{B\bar{B}} \frac{B(x, y)}{\int \int_{DP} B(x, y) dx dy}
 \end{aligned} \tag{3.11}$$

where

- $x$  and  $y$  are the event position in the Dalitz plane.
- $\epsilon(x, y)$  is the efficiency of reconstruction of events.
- $N$  is the number of resonant contributions.
- $a_i$  is the complex coefficient for each resonant contribution.
- $g_i$  refers to the dynamics associated including line shape and angular distribution with each of the contributions.
- $Q(x, y)$  and  $B(x, y)$  are the amount of continuum and  $B$  related background in the Dalitz plot.
- $f_{q\bar{q}}$  and  $f_{B\bar{B}}$  are the fraction of continuum and  $B$  related background.

After fitting with Laura++ the complex coefficient values  $a_i = C_i e^{i\theta_i}$  are output which gives resonant amplitudes  $c_i$  and phase  $\theta_i$  for  $i^{th}$  resonance [56]. Generating toy MC using Laura++ it is possible to assign arbitrary amplitude and phase values for each resonance but in the fitting Laura++ can only measure relative amplitudes and phase values. Therefore we choose to arbitrarily set one resonant amplitude as 1 and phase as 0. Then all the other resonant amplitudes and phases are calculated relative to this reference resonance.

Even if we have extracted amplitudes and phase values from a fit, it is hard to compare with another analysis because the definitions of amplitude and phase could be different for both analysis. To compare different analyses we calculate fit fractions according to

$$F_i = \frac{\int \int_{DP} |a_i g_i(x, y)|^2 dx dy}{\int \int_{DP} |\sum_j a_j g_j(x, y)|^2 dx dy} \quad (3.12)$$

between resonances and give them as output. These values allow us to compare with another analysis and also calculate a branching fraction (BF) of each intermediate decay.

### 3.5 Dalitz plot Efficiency and Self cross feed

#### 3.5.1 Efficiency

In my analysis one of the main objectives is to calculate the BF using

$$BF = \frac{\textit{Signal yield}}{(\textit{Total number of } B\bar{B} \textit{ pairs}) \times (\textit{Efficiency})}. \quad (3.13)$$

The *Signal yield* is the number of signal events returned by the final fit to the  $M_{BC}$  distribution and *Total number of  $B\bar{B}$  pairs* taken by Belle records [58]. I will calculate the *Efficiency* using MC and/or data control channels according to Equation 3.2. When calculating the efficiency from MC I know the number of events after reconstruction and I also know the number of input events from the MC data sets. I calculate the efficiency using signal MC for the mode  $B^\pm \rightarrow K_s^0 \pi^\pm \pi^0$  generated uniformly in phase space. I check the distribution of the efficiency across the Dalitz plot by plotting the histograms of efficiency versus Dalitz plot position. To do this I use reconstructed information and the MC truth (generated event) information for all generated events. To make the efficiency plot I first take the truth MC to make the denominator histogram. Secondly, using the reconstructed MC, I make another histogram with the same binning for the numerator and then divide the numerator by the denominator on a bin by bin basis as shown in the Figure 3.16. When making the efficiency plot it is important to have a reasonable bin size because if the bin size is too small as shown in the Figure 3.17 or too large as shown in the Figure 3.18 we cannot see features of the plot such as efficiency drops near the edges or corners, or the plot will be dominated by statistical fluctuations, respectively.

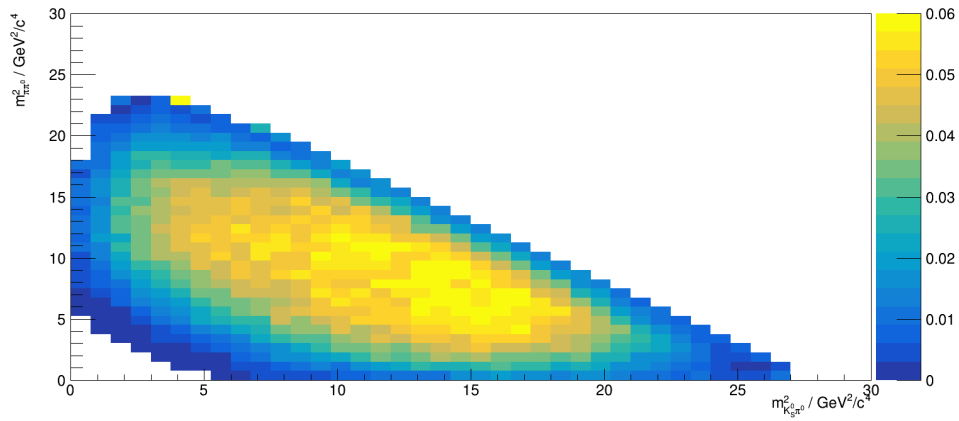


Figure 3.16: Dalitz efficiency plot for 40 by 40 bin size

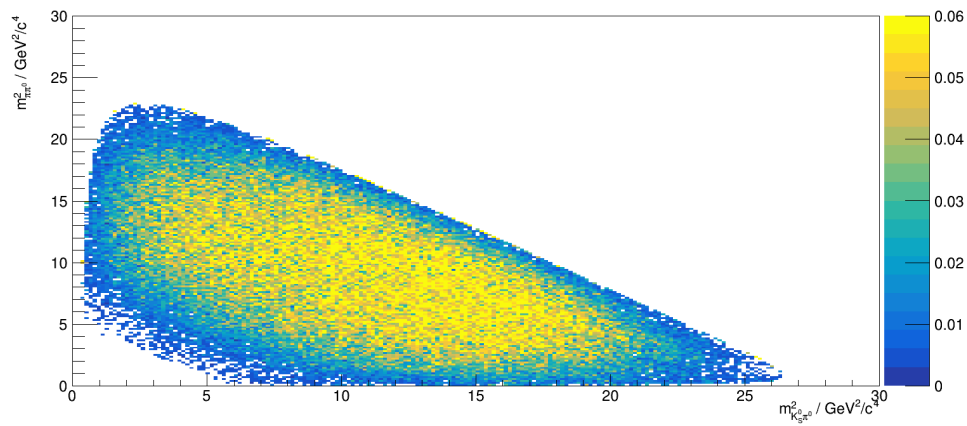


Figure 3.17: Dalitz efficiency plot for 200 by 200 bin size. Bin size is too small and plot is dominated by statistical fluctuation particularly near the edges of the plot

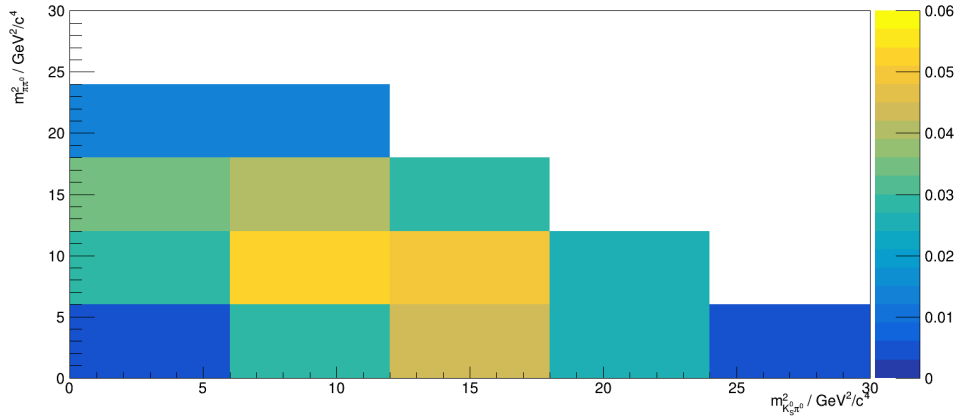


Figure 3.18: Dalitz efficiency plot for 5 by 5 bin size. Bin size is too large and plot does not show enough details

When looking at efficiency, I would like it to be as high as possible, but I also want to reduce the background. I have to balance between efficiency and background. It is useful if the efficiency is relatively uniform across the Dalitz plot, as sharp changes in efficiency may artificially distort potential resonance bands in the plot. If there are sharp efficiency changes around the regions where resonances occur I need to re-examine our analysis method or study more to understand exactly how these sharp changes can affect our fit and results.

### 3.5.2 Self Cross Feed (SCF)

Self cross feed(SCF) can only be studied in MC. These events are signal events but incorrectly reconstructed. This can happen when two daughter particles come from one  $B$  meson decay and the third daughter particle comes from the other  $B$  meson in the event. Then the reconstructed event can look like a signal event but it is not a signal event. Mainly this can happen due to using an incorrect  $\pi^0$  because there are many  $\pi^0$ s reconstructed in each event and false  $\pi^0$ s from random gamma pairs. Selection criteria help to remove these SCF events and keep true signal events. I expect that there should be a relatively small number of SCF events after all selection criteria. Figure 3.19 shows a SCF map created using the same MC sample and selection criteria used to create the efficiency map as in the

Figure 3.16.

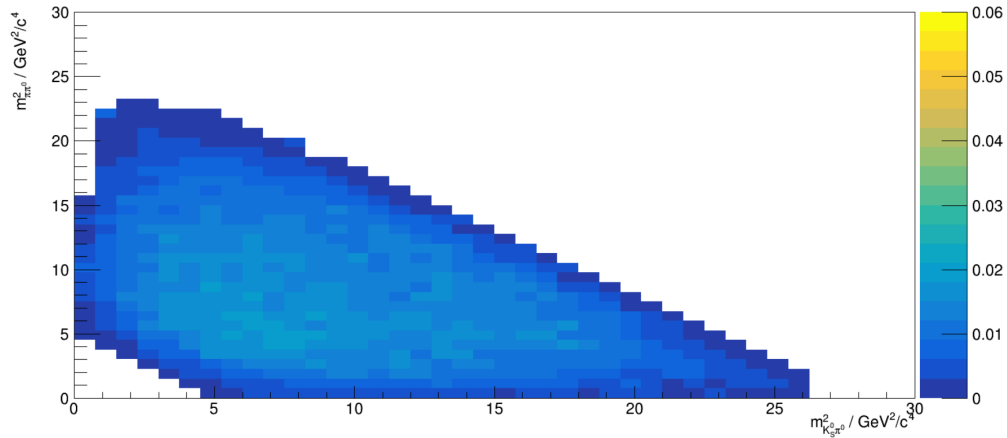


Figure 3.19: Dalitz SCF plot for 40 by 40 bin size

## 3.6 Fitting

### 3.6.1 Resonance model

My analysis strategy will involve performing a fit to MC or data in the Dalitz plot to extract the signal yield taken from the  $M_{BC}$  fit. It is important to develop an analysis strategy that will work on the data without bias or unexpected behaviors. I use full MC generated with known resonances using the Belle event generators to test fit models using Laura++. Initially 5 million  $B^\pm \rightarrow K_S^0 \pi^\pm \pi^0$  direct decay events are generated and reconstructed for an efficiency map as shown in Figure 3.16. The high number of full MC events helps to smooth the Dalitz plot within the boundaries and this map is very important as input to Laura++. Secondly one hundred thousand signal events are generated including the following resonances and a non-resonant contribution for the fitting study

- $K^{*\pm}(892)$
- $K^{*0}(892)$
- $K_0^{*0}(1430)$
- $K_2^{*0}(1430)$

- $\rho^\pm(770)$ .

After applying all selection criteria, we can draw the Dalitz plot as  $m_{23}^2$  vs  $m_{13}^2$ . Some resonance bands may be identifiable by inspection, this can help determine the most prominent intermediate resonances and their spin status using line band continuity or dis-continuity. The Dalitz plot shown in the Figure 3.14 is a sample plot generated using toy MC without have any interference between resonances. In real full MC or data analysis we cannot identify the individual resonances so easily, and there is interference between resonances and of course in data no way to assign them to any specific intermediate decay path. Figure 3.20 shows the full MC Dalitz plot distribution before and after selection criteria.

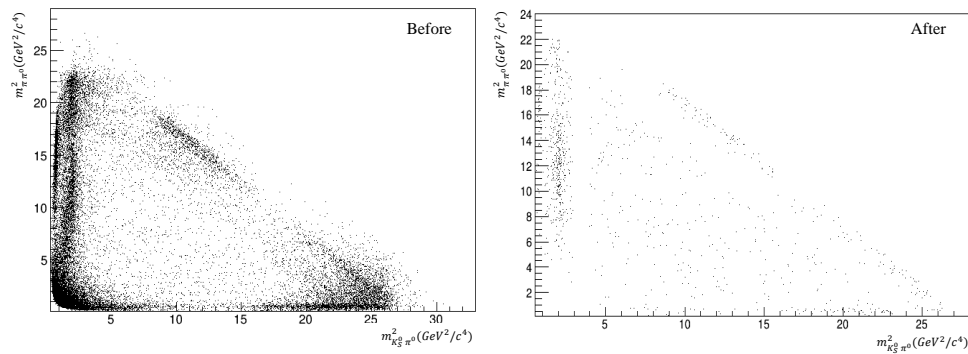


Figure 3.20: Dalitz Plot distribution of full MC before (left) and after (right) selection criteria are applied.

As seen in the Figure 3.20 by inspection of the Dalitz plot I can determine the mass and spin of possible contributing resonances and associate them with known particles as above. For all but the most common resonances, these resonance bands are not easily visible because of low amplitude and therefore low number of events. I can look at the projections of the Dalitz variables individually. As an example Figure 3.21 shows the histogram of the invariant mass distributions of  $K_S^0 \pi^\pm$ ,  $K_S^0 \pi^0$  and  $\pi^\pm \pi^0$  in a full MC sample.

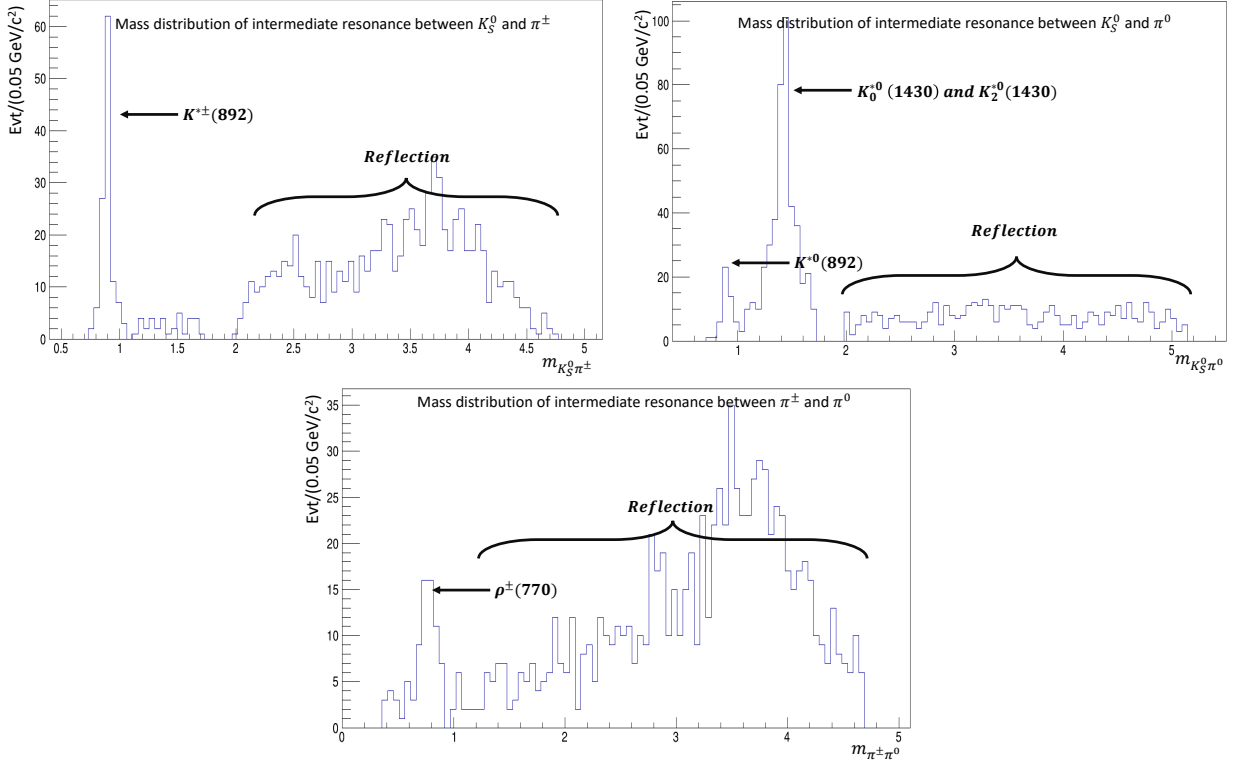


Figure 3.21: Invariant mass distribution of  $K_S^0 \pi^\pm$  (top left),  $K_S^0 \pi^0$  (top right), and  $\pi^\pm \pi^0$  (bottom).

As shown in Figure 3.21 I can clearly find four peaks in the plots corresponding to different intermediate resonances. Structure in the mass distribution between 2 - 5 GeV range comes from *reflections* of the distribution of resonances between a different pair of particles. These mass distributions include only full MC signal events, but, in the full analysis, would include background events also. Therefore it is important to consider the DP distribution of continuum and B-related background events.

### 3.6.2 Background distributions in the DP

In order to develop a good fitting module, it is important to include the expected background Dalitz plot distribution. Therefore continuum and B-related background MC are reconstructed and selected using same signal selection criteria. The resulting Dalitz plot distributions are shown in Figure 3.22. These plots demonstrate how well the large continuum

and B-related background rejection works and the distribution of background events in the Dalitz plot.

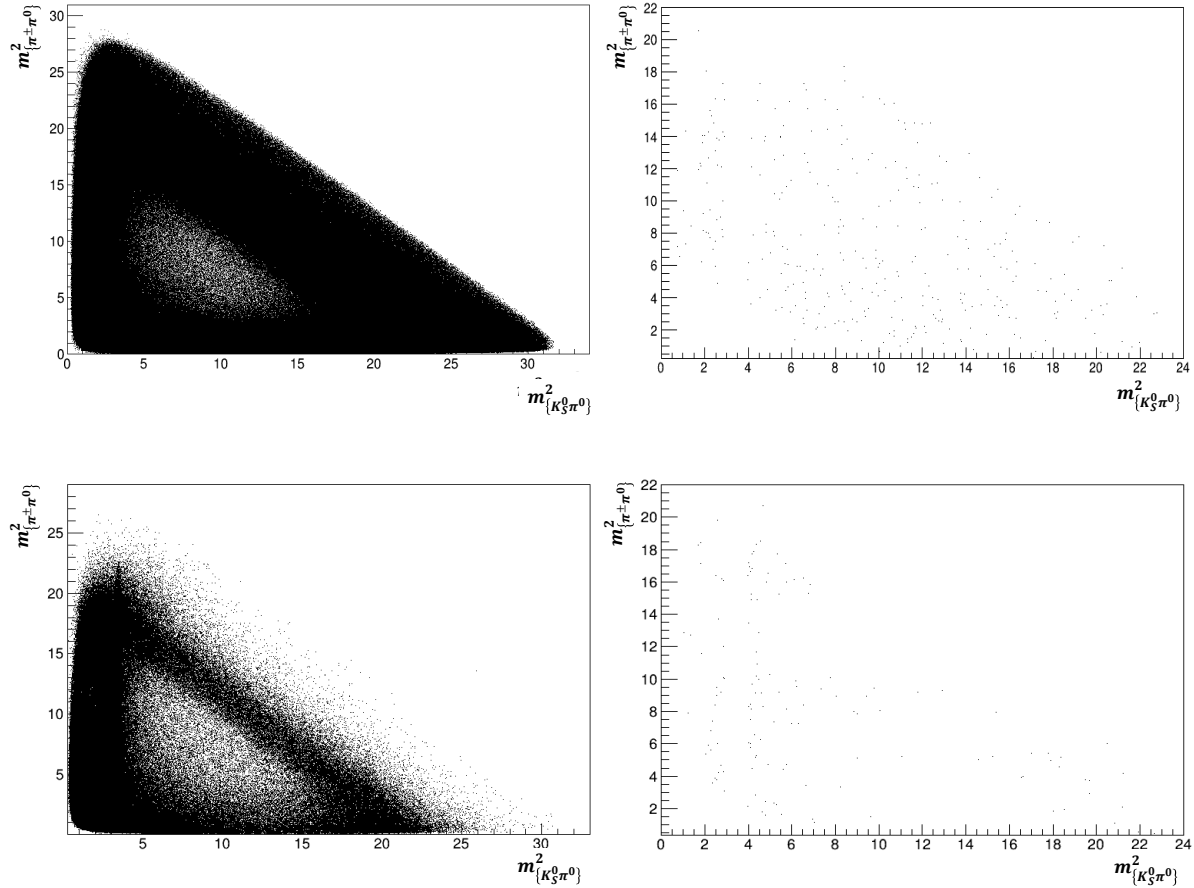


Figure 3.22: Continuum background distribution before and after selection criteria (top left and right plots), B-related background distribution before and after selection criteria (bottom left and right plots).

I need one more Dalitz distribution to build the fit model. In full MC it is possible to separate SCF events from the pure signal events but, in the data it is impossible. Figure 3.23 shows the SCF distribution.

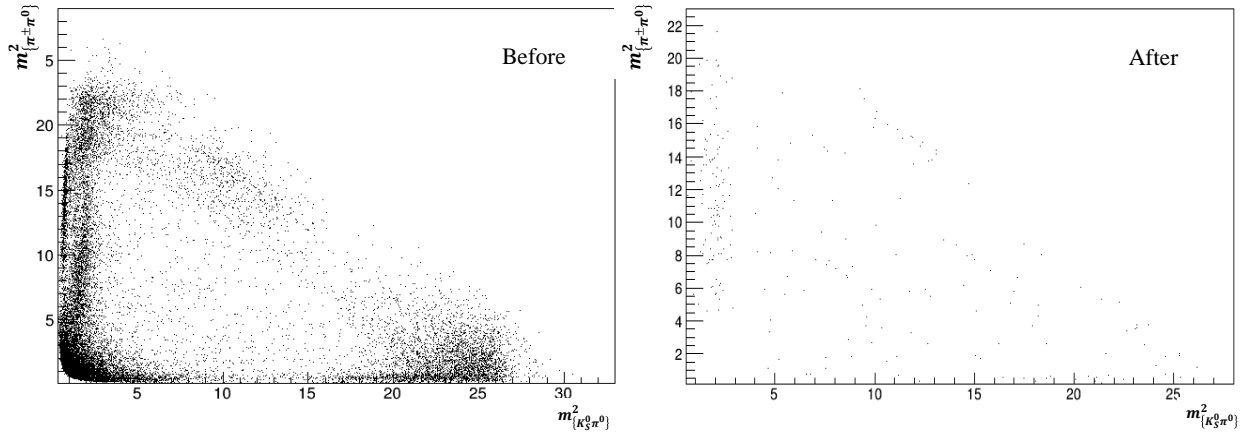


Figure 3.23: SCF distribution before selection criteria (left) and after selection criteria (right)

I created the SCF DP distribution using the same selection criteria as developed for signal. Lastly I combine all signal and background events after selection into one DP distribution shown in Figure 3.24.

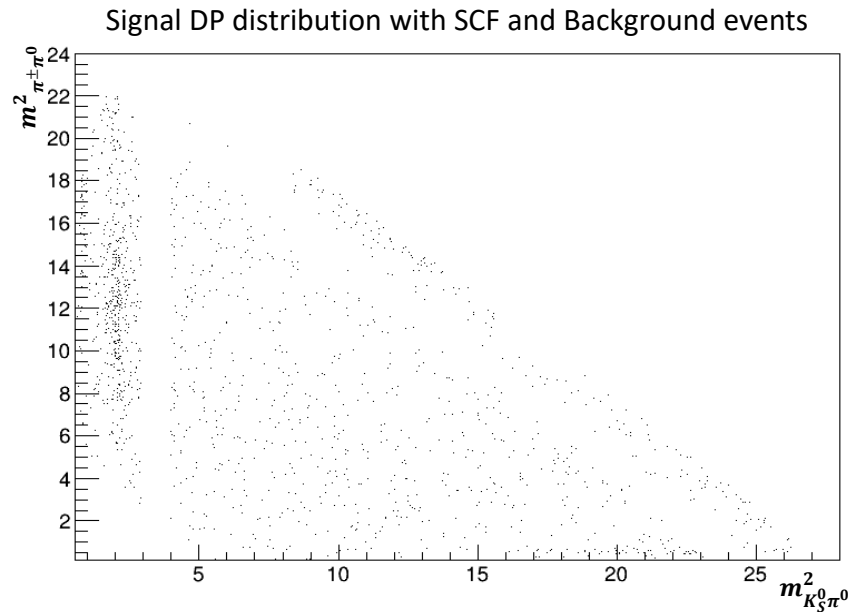


Figure 3.24: Signal Dalitz plot combined with continuum, B-related and SCF event distributions

This DP distribution represents what we might expect from experimental data and is used as input for fitting with Laura++. For fitting we provide various inputs to Laura++;

the efficiency Dalitz map; continuum Dalitz map; B-related Dalitz map; and SCF Dalitz map. These maps contain our knowledge of the Belle detector response and basic physics used to extract the branching fraction from the data.

## CHAPTER 4 RESULTS

### 4.1 Performance of selection criteria on Full MC and Data

In the reconstruction process of the  $B^\pm \rightarrow K_s^0 \pi^\pm \pi^0$  decay, I use loose selection ranges for different variables as described in Section 3.2. I compare signal, B-related, and continuum event distributions in the  $M_{BC}$  and  $\Delta E$  variables to optimize the tight cuts as explained in Section 3.2.1. Figure 4.1 shows the behavior of signal, B-related, and continuum events after the tight selection. When I compare signal, continuum and B-related  $M_{BC}$  distributions in the figure the signal events accumulate around  $5.28 \text{ GeV}$  which is the  $B$  meson mass. A similar feature is observed in the B-related events, but not in the continuum events.

In the  $\Delta E$  distributions we can see the signal events around  $Zero$  but both continuum and B-related events gather around  $-0.4 \text{ GeV}$ . These two selections are the most important because they give large separation of background and signal events.

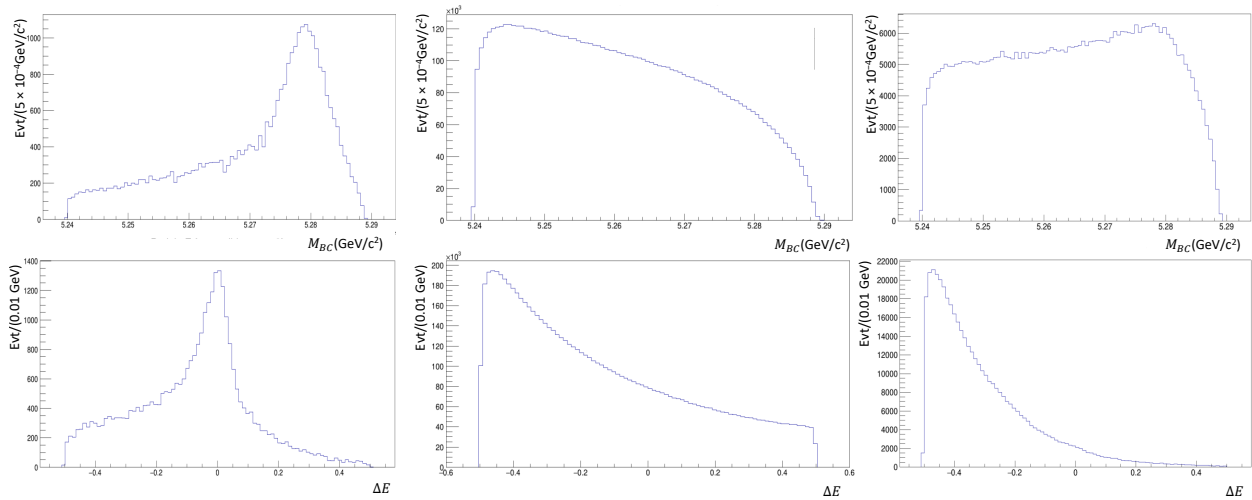


Figure 4.1: Signal, Continuum and, B-related events distribution in the  $M_{BC}$  and  $\Delta E$  variables before selections

After the initial selection criteria described in Section 3.2.1, it is important to reject more background events using continuum shape sensitive variables [50] (ClearCone, Thrust, Helicity angle, and others.) as discussed in Section 3.2.2. After two rounds of training and testing with signal and background samples, I find the BDT method is the most effective to

reject backgrounds. Figure 4.2 shows the invariant mass distribution for  $K_S^0\pi^0$  before and after the BDT selection of greater than 0.13. When I compare the top and bottom rows of the histograms in the plots, I can clearly see peaks from the signal and B-related events reduced, but the continuum sample is reduced much more than the other two types.

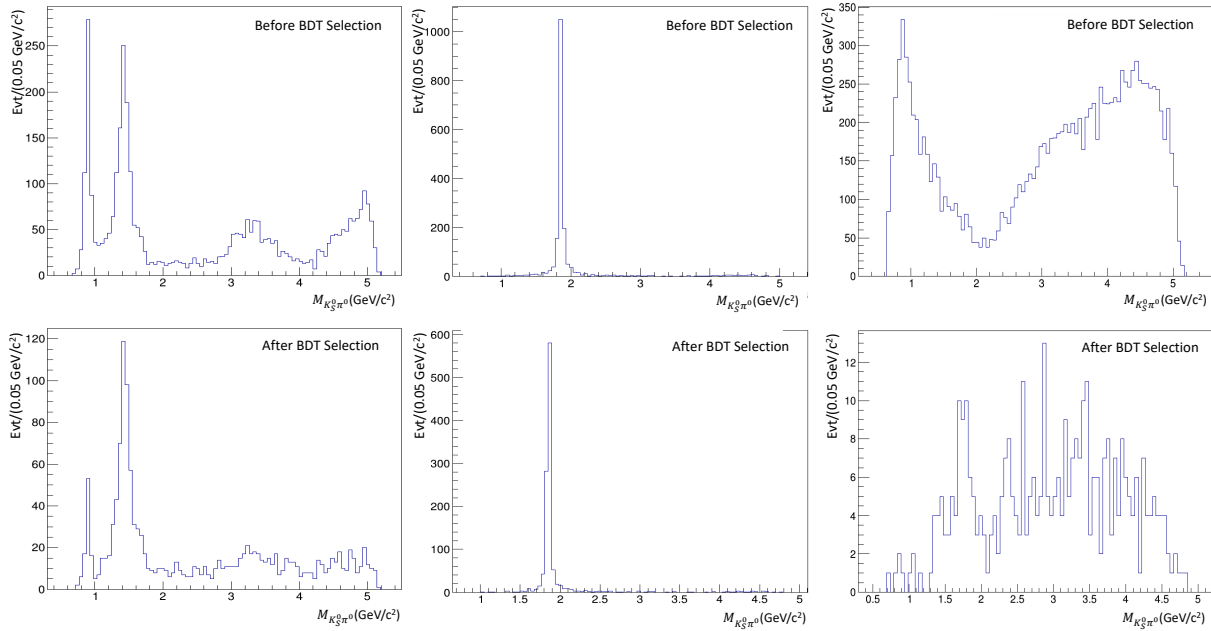


Figure 4.2: Signal, continuum and, B-related events  $K_S^0\pi^0$  mass distribution before and after the BDT selection.

Another major background contribution to this analysis comes from  $D$  meson decays seen in the invariant mass distributions of  $K_S^0\pi^+$  and  $K_S^0\pi^0$ . I can see this  $D$  meson contribution clearly in B-related background distribution; as example the peak in the bottom middle graph in Figure 4.2. These clearly show  $D^0$  meson contribution. Formation of  $D$  mesons come from  $B$  decays to charm quarks with the  $D$  decaying to  $K_S^0$  and  $\pi$ . To select only the  $B^\pm \rightarrow K_S^0\pi^\pm\pi^0$  charmless decay, I remove  $D$  meson with a veto as explained in Section 3.2.1 to remove any  $D$  meson contributions.

Finally all my selection criteria are summarized in Table 4.1 in the full MC corresponding to  $571 \text{ fb}^{-1}$  of integrated luminosity. Here:

- Signal events  $\Rightarrow$  Both pure signal and SCF events

- B-related events  $\Rightarrow$  Charged and mixed events
- $q\bar{q}$  events  $\Rightarrow$  Charm and  $uds$  events (all continuum events)
- Total Background events  $\Rightarrow$  Summation of continuum and B-related events

Table 4.1: Summary of the full MC selection criteria corresponding to  $571 \text{ fb}^{-1}$  of simulated luminosity.

Variable (X)	Range	Signal Events	B-Related Events	$q\bar{q}$ Events	Total Bkgnd Events
Candidate	$X = 0$	4110	438523	7767845	8206368
Good $K_S^0$	$X = 1$	3040	102815	1503053	1605868
$M_{BC}$	$5.275 < X < 5.29$	1564	33654	254580	288234
$\Delta E$	$-0.1 < X < 0.05$	980	3311	35846	39157
ChiProb	$0.5 < X$	693	2265	21971	24236
$M_{K_S^0}$	$0.49 < X < 0.51$	677	2216	20159	22375
$E_{\pi^0}$	$0.7 < X$	503	1909	15051	16960
BDT	$0.13 < X$	174	1193	410	1603
$M_{K_S^0\pi^+}$	$X < 1.70788$ or $1.9924 < X$	168	1164	385	1549
$M_{K_S^0\pi^0}$	$X < 1.70788$ or $1.9924 < X$	152	138	341	479

In this table I begin with 8,206,368 full MC background events and 4,110 signal events with a ratio of roughly 1:2000. Of these 4,110 signal events, 3,274 comes from SCF. Table 4.2 compares the detailed effects of my selection in the full MC to  $571 \text{ fb}^{-1}$  of data. Here I can see how the SCF events and all other background events types change with my selection criteria. The initial 8,206,368 full MC background events correspond to 836 true signal events. This is roughly 1:9800. After all selections I have 479 background to 114 of true signal events which is a ratio of 1:4. I can use these to verify background estimations and

BF calculations for both full MC and data.

Applying all the selections to the data yields the distribution of  $\Delta E$  vs  $M_{BC}$  and 1D projection of  $M_{BC}$  shown in the Figure 4.3, to compare with Figure 3.5.

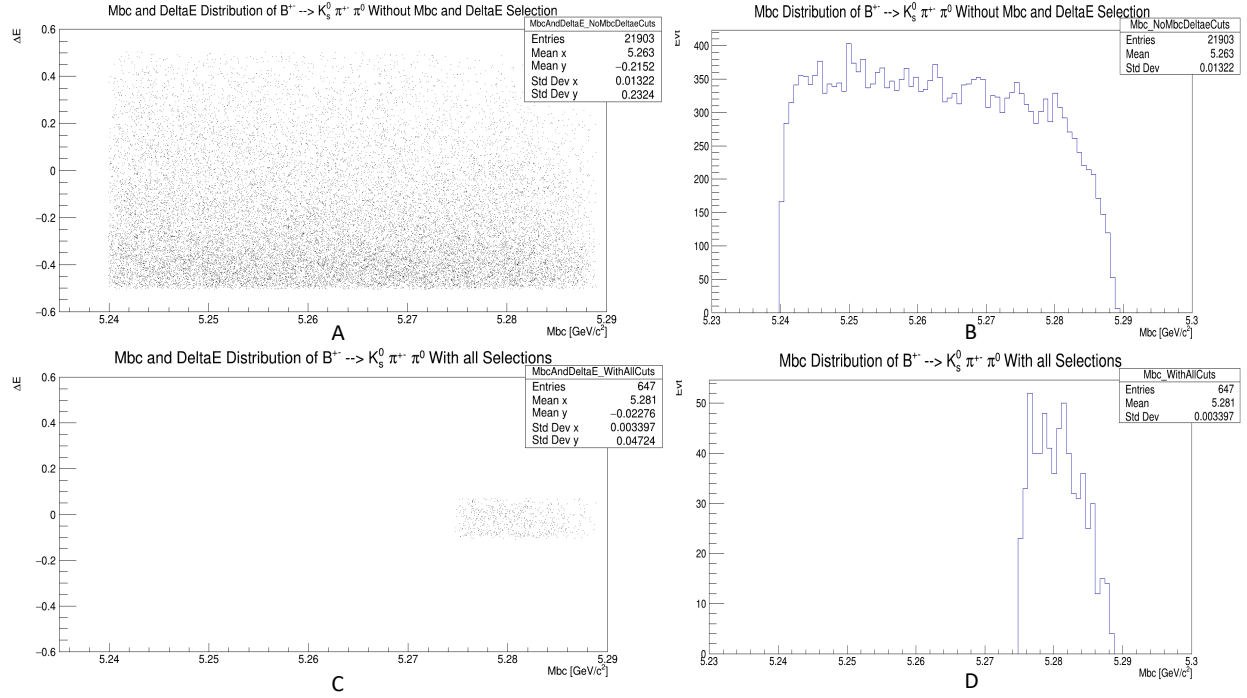


Figure 4.3: DATA : (A)  $\Delta E$  Vs  $M_{BC}$  distribution without  $M_{BC}$  and  $\Delta E$  Selection. (B) 1D projection of  $M_{BC}$  distribution without  $M_{BC}$  and  $\Delta E$  selection. (C)  $\Delta E$  Vs  $M_{BC}$  distribution with  $M_{BC}$  and  $\Delta E$  Selection. (D) 1D projection of  $M_{BC}$  distribution with  $M_{BC}$  and  $\Delta E$  selection.

Table 4.2: Number of events after each selection criteria for signal, charged, mixed, charm and,  $uds$  for  $571 \text{ fb}^{-1}$  of luminosity in both full MC and data.

Variable (X)	Range	Signal Ev		Charged Ev		Mixed Ev	Charm Ev	uds Ev	Data Ev
		True Sig	SCF	Bkg	Sig				
Candidate	$X = 0$	836	3274	276211	2322	159990	2594227	5173618	4111983
Good $K_S^0$	$X = 1$	675	2365	57161	1830	43824	674475	828578	908295
$M_{BC}$	$5.275 < X < 5.29$	585	979	19024	1582	13048	108470	146110	151608
$\Delta E$	$-0.1 < X < 0.05$	519	461	1503	1406	402	14755	21091	22998
ChiProb	$0.5 < X$	385	308	1003	1012	250	8759	13212	13267
$M_{K_S^0}$	$0.49 < X < 0.51$	378	299	977	995	244	8211	11948	12101
$E_{\pi^0}$	$0.7 < X$	364	139	757	971	181	6127	8924	9225
BDT	$0.13 < X$	130	44	438	670	85	174	236	660
$M_{K_S^0\pi^+}$	$X < 1.70788$ or $1.9924 < X$	126	42	432	657	75	163	222	647
$M_{K_S^0\pi^0}$	$X < 1.70788$ or $1.9924 < X$	114	38	84	0	54	138	203	647

## 4.2 Results of Data driven background estimation

### 4.2.1 Background and Error estimation

These numbers guide my expectation for the background contribution in the signal region of 5.275 to 5.29  $GeV$  in  $M_{BC}$ . In Section 3.3 I use four different methods to estimate the number of background events in the signal region by fitting an ARGUS function to the  $M_{BC}$  distribution in Figure 3.6. I subtract the estimated background from the total number of events in the signal region. The ARGUS function has three parameters and a fixed “End point” parameter

$$f(x; \chi, c) = \frac{\chi^3}{\sqrt{2\pi}\Psi(\chi)c^2} \cdot x \sqrt{1 - \frac{x^2}{c^2}} \cdot \exp\left\{-\frac{\chi^2}{2} \left(1 - \frac{x^2}{c^2}\right)\right\}, \quad (4.1)$$

where:

- $c$  : is the end point parameter (fixed at 5.289)
- $\frac{\chi^2}{2}$  : is the shape parameter
- $\frac{\chi^3}{\sqrt{2\pi}\Psi(\chi)c^2}$  : is the normalization ( $\Psi(\chi)$  is function of cumulative distribution and probability density distribution ).

Table 4.3 shows the ARGUS function parameter values and their errors I find in fits to both full MC and data. In this fit, I fixed the “end point” as 5.289  $GeV$ . The normalization parameter errors vary between 7% - 9% and the shape parameter errors vary between 20% - 30%. Method 4 in Section 3.3 shows the best agreement with the MC truth. Therefore I use Method 4 to fit the data distribution.

Table 4.3: ARGUS function parameter values for full MC and data fit

Method	ARGUS Function Parameters Value		
	Normalization	End point (Fixed)	Shape
Method 1	$109.022 \pm 9.94653$	5.28900	$28.1711 \pm 6.79792$
Method 2	$96.6475 \pm 7.60892$	5.28900	$19.4822 \pm 5.81918$
Method 3	$90.1706 \pm 7.04663$	5.28900	$16.3526 \pm 5.70209$
Method 4	$102.698 \pm 9.65601$	5.28900	$25.6894 \pm 6.97809$
DATA (Method 4)	$110.949 \pm 10.4183$	5.28900	$31.6915 \pm 7.02032$

The extracted parameters in the Table 4.3 allow me to calculate the area under the function and convert it to a number of events and their stranded deviation. Each parameter has an upper and lower limit and I use a GAUSSIAN distributed random number generator to generate  $10^5$  parameter values between the lower and upper limits and integrate the ARGUS function from 5.275 to 5.289  $GeV$  in  $M_{BC}$  to estimate the background contribution and its uncertainty. Figure 4.4 shows the distribution of the number of background events in the signal region using this methodology on data and Table 4.4 summarizes the results of the background estimation on the full MC and data.

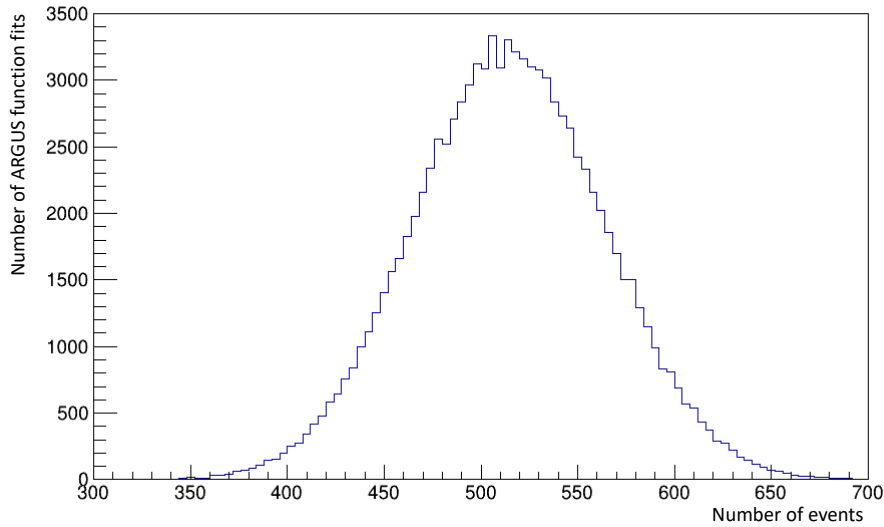


Figure 4.4: Distrubition of the number of estimated background events in data after fit using method 4.

Table 4.4: Area under the curve and number of events for Full MC and DATA

Method	Integreated area	Cal Bkgnd evts	Total evts	True MC Bkgnd evts
Method 1	$0.35784 \pm 0.03430$	$511 \pm 49$	631	479
Method 2	$0.32543 \pm 0.02588$	$465 \pm 37$	631	479
Method 3	$0.30660 \pm 0.02460$	$438 \pm 35$	631	479
Method 4	$0.33887 \pm 0.03176$	$484 \pm 45$	631	479
Data	$0.36008 \pm 0.03461$	$514 \pm 49$	647	Unknown

### 4.3 Branching Fraction determination and error calculation

The goal of this thesis is to calculate the branching fraction (BF) of the  $B^\pm \rightarrow K_s^0 \pi^\pm \pi^0$  decay for both generated Full MC, as check, and in Belle data. After all selection criteria, background estimation and, Laura++ fitting the BF can be calculated as mentioned in Equation 3.13, and I need the numbers and uncertainties corresponding to *Signal yield*, *Total number of  $B\bar{B}$  pairs*, and *Efficiency*.

- Step 1 (*Efficiency* and its uncertainty)

Initially I generate 100,000 full MC events with intermediate resonances and after all selection criteria I end up with 984 events. Therefore according to Equation 3.2

$$\begin{aligned} Efficiency &= 984/100000 \\ &= 9.84 \times 10^{-3} \end{aligned} \tag{4.2}$$

and the rough relative statistical uncertainty is

$$\begin{aligned} Efficiency_{Uncertainty} &= 1/\sqrt{984} \\ &= 3.1878 \times 10^{-2} \sim 3.1\% \end{aligned} \tag{4.3}$$

- Step 2 (*Total number of  $B\bar{B}$  pairs* and its uncertainty)

The number of  $B$  events in Hadron B(J) from experiments 31 to 65 is  $(619.620 \pm 9.441) \times 10^6$  which corresponds to  $571 \text{ fb}^{-1}$  of integrated luminosity documented in [58]. This includes both  $B^0\bar{B}^0$  and  $B^+B^-$  events. I assume 50% of  $\Upsilon(4S)$  decay to  $B^+B^-$  pairs. Therefore *Total number of  $B\bar{B}$  pairs* =  $(309.81 \pm 4.72) \times 10^6$  and the statistical uncertainty is  $4.72/309.81 \sim 1.52\%$ .

- Step 3 (*Signal yield* and its uncertainty)

The *Signal yield* can be calculated by subtracting the estimated background events from the total number of input events as in Table 4.4. As mentioned in Sections 3.3 and 4.2.1 Method 4 gives the best result. Using Method 4, *Signal yield* for full MC is  $147 \pm 45 \approx 30.61\%$  uncertainty and  $133 \pm 49$  for data and its uncertainty  $\approx 36.84\%$ .

- Step 4 (Branching Fraction uncertainty)

As in Section 3.5.1 I can calculate the BF using Equation 3.13

$$\begin{aligned}
BF \text{ pct uncertainty} &= \sqrt{\frac{\sigma_S^2}{S^2} + \frac{\sigma_E^2}{E^2} + \frac{\sigma_N^2}{N^2}} \\
&= \sqrt{S_E^2 + E_E^2 + N_E^2}
\end{aligned} \tag{4.4}$$

where:

- $S, S_E$  : Signal yield, Signal yield percentage uncertainty.
- $E, E_E$  : Efficiency, Efficiency percentage uncertainty.
- $N, N_E$  : Total number of  $B\bar{B}$  pairs, total number of  $B\bar{B}$  pairs percentage uncertainty.
- $\sigma_S^2$  : Signal yield uncertainty.
- $\sigma_E^2$  : Efficiency uncertainty.
- $\sigma_N^2$  : Number of  $B\bar{B}$  pair uncertainty

As a summary of the above steps for full MC and data, Tables 4.5 and 4.6 show all the values and errors for the BF calculation.

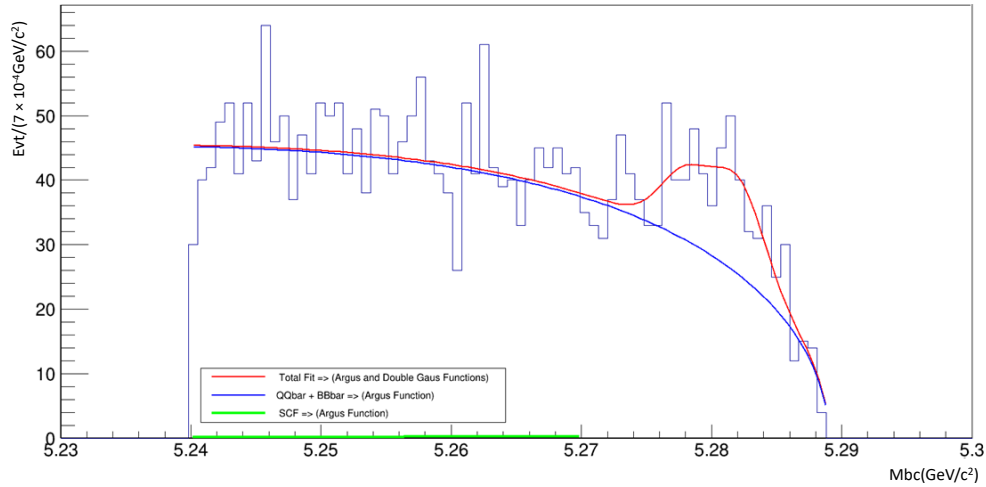
Table 4.5: Branching fraction calculation values for full MC.

Source	Value	Uncertainty %
Total number of $B\bar{B}$ pairs	309810000	1.52
Efficiency	0.00984	3.10
Signal yield	147	30.61
Total		30.8

Table 4.6: Branching fraction calculation values for data

Source	Value	Uncertainty %
Total Number of $B\bar{B}$ pairs	309810000	1.52
Efficiency	0.00984	3.10
Signal yield (DATA)	133	36.84
Total		37.0

According to the tables above the uncertainty on the BF is dominated by the uncertainty on the *Signal yield*. Minimizing this error is very challenging because I have a small number of events in the signal region as shown in Figure 4.5. According to Table 4.1, the signal to background ratio is 1:3 in Full MC and we can see the same result in this figure. Therefore as mentioned in Step 3, variation in the *Signal yield* and its uncertainty directly depends on the background estimation.

Figure 4.5:  $M_{BC}$  distribution of data without  $M_{BC}$  selection.

In Figure 4.5 the green line represents the SCF fit in the background region using ARGUS function. The blue line represents the continuum and B-related background events fit using another ARGUS function in the background region (5.24 to 5.27 GeV). The dashed line

represents the extrapolation of the background into the signal region. From this extrapolation I can calculate only continuum and B-related background events without any SCF events. The red line represents the combined fit of both ARGUS functions (QQbar + BBbar, SCF) and the double GAUSSIAN function for signal. I can clearly see a small peak in the signal region between 5.278 to 5.282  $GeV$  which is around the B meson mass of 5.28  $GeV$  and where I expect signal to accumulate. It is challenging to isolate this small peak using a known functional fit with good accuracy. Results are summarized in Table 4.7. Note the branching fraction in the full MC was set to  $5 \times 10^{-5}$  and my extraction agrees well.

Table 4.7: Summary of branching fraction for full MC and data

Source	Branching Fraction $10^{-5}$	Branching Fraction uncertainty %
Full MC	$4.822 \pm 1.49$	30.8
Data	$4.363 \pm 1.61$	37.0

## 4.4 Full MC Dalitz plot study

### 4.4.1 Determination of resonance model

The signal in data is not large or clean enough to do a Dalitz analysis. Here I do the Dalitz analysis on the full MC to show how such an analysis could be done with larger, more pure data set. In Section 3.6.1 the generated full MC with known resonance contributions goes through my selection criteria, giving the Dalitz plot distribution in Figure 3.20 and the 1D mass distributions in Figure 3.21. I use these distributions to determine the resonances in this decay by fitting with Laura++. For the resonance fitting, it is very important to give all Dalitz plot maps as input to Laura++. As mentioned in Section 3.6.2 Dalitz plots of continuum background, B-related background both after selection criteria, shown in Figure 3.22 and the Dalitz plot of selected SCF events, shown in Figure 3.23, are used as background input. Figure 3.16 is the efficiency Dalitz map input to Laura++. Finally the generated full MC distributions (signal, SCF,  $q\bar{q}$  and,  $B$ -related) shown in Figure 3.24 is

the Laura++ fit target.

I fit this model using randomized initial amplitude and phase values. I select two contributions, one resonance contribution which is  $K^{*+}(892)$  and direct decay NR (non-resonance) as fixed parameters one at a time before running the fit. Laura++ allows amplitude ranges  $0 < x$  and phase ranges  $-\pi < x < \pi$ . I fix the  $K^{*+}(892)$  amplitude, phase values as 1.3 and -1.831 respectively non-resonance contribution as 1 and 0 for fitting. After running a number of fits, Laura++ generated an output root file containing the amplitudes, phases, fit fractions, fit status, NLL (Section 3.4.3), and others. One of the very important variables in the generated root file is the fit status variable as shown in Figure 4.6. This helps to understand how well the fits work and remove the poor fits.

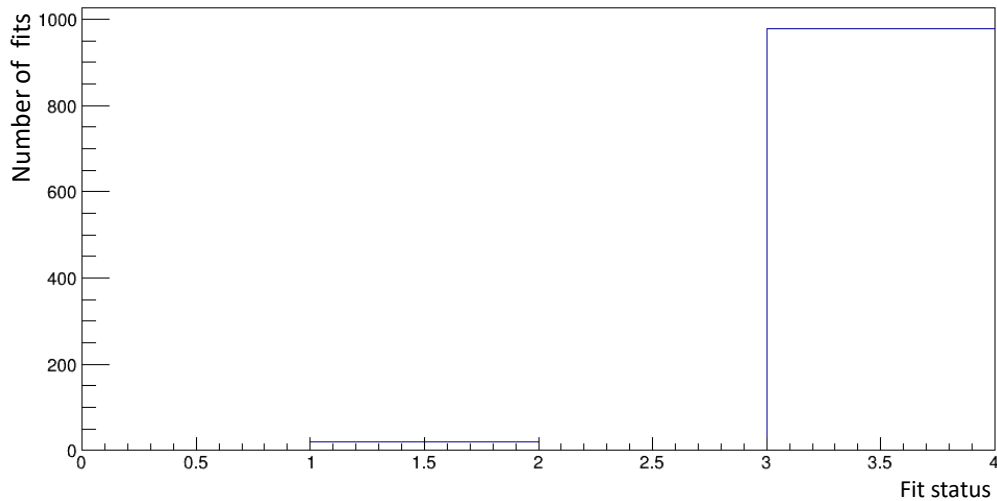


Figure 4.6: Number of good, from 3 to 4, and bad, from 1 to 2, fits after 1000 fits in Laura++

I remove all bad fits before extracting amplitude and phase values from the fit. According to Figure 4.6 among 1000 Laura++ fits, I accept good fits by requiring “fitStatus=3” and obtain the NLL distribution in Figure 4.7. This shows clearly how failed fits gives bad NLL value, around -14000, and all good fits give NLL value greater than -2000.

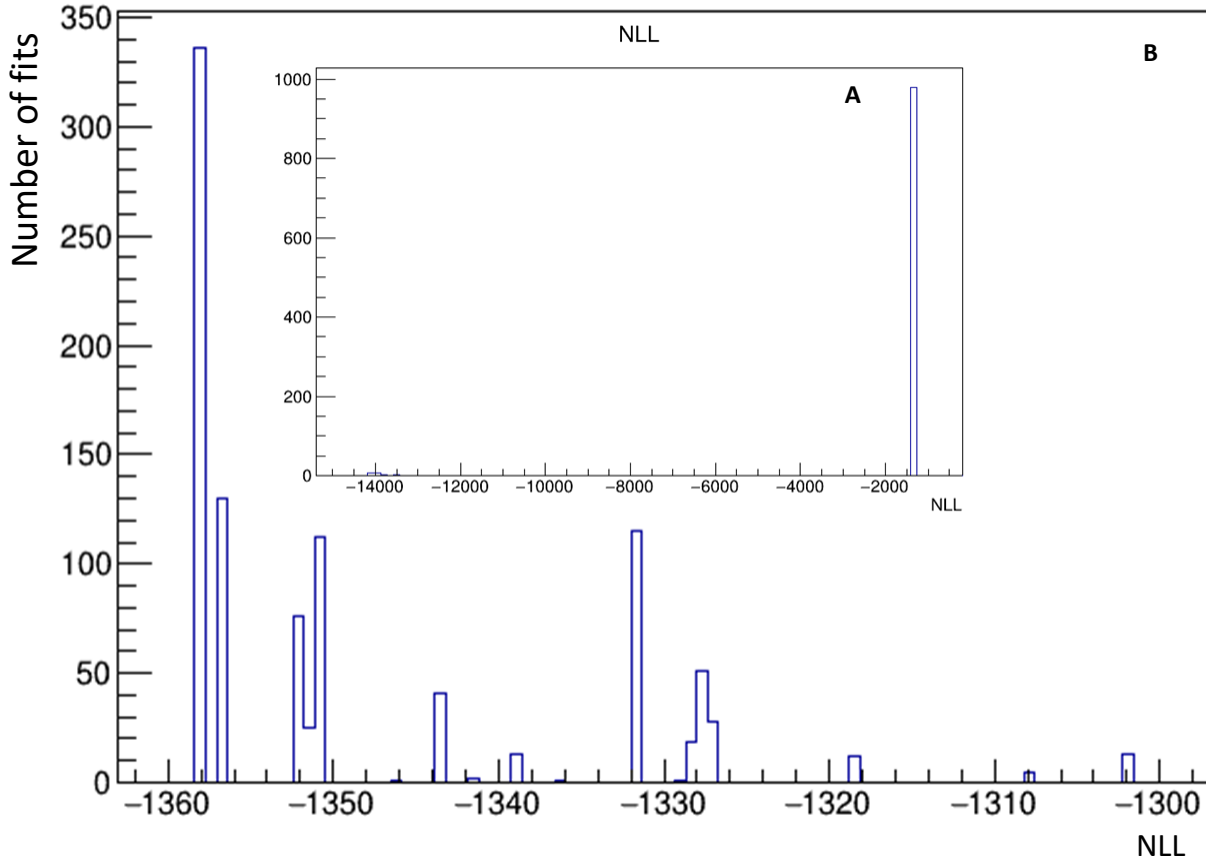


Figure 4.7: (A) shows NLL distribution and (B) shows after accept good fits.

In fitting to the full MC with “fitStatus=3”, it is important to check if I include the correct number of resonance or not. If I include all correct intermediate resonances then I expect the NLL value to have a higher negative distribution as in Figure 4.8(A). On the other hand if one or a couple of resonances is not included then I expect lower NLL distributions as in Figure 4.8(C) and (D). If I include a resonance which is not actually in the full MC, then that resonance makes very little change to the NLL distribution as in Figure 4.8(B). This case can be found as the fit amplitude and phase values are consistent with zero for resonances not in the Dalitz distribution.

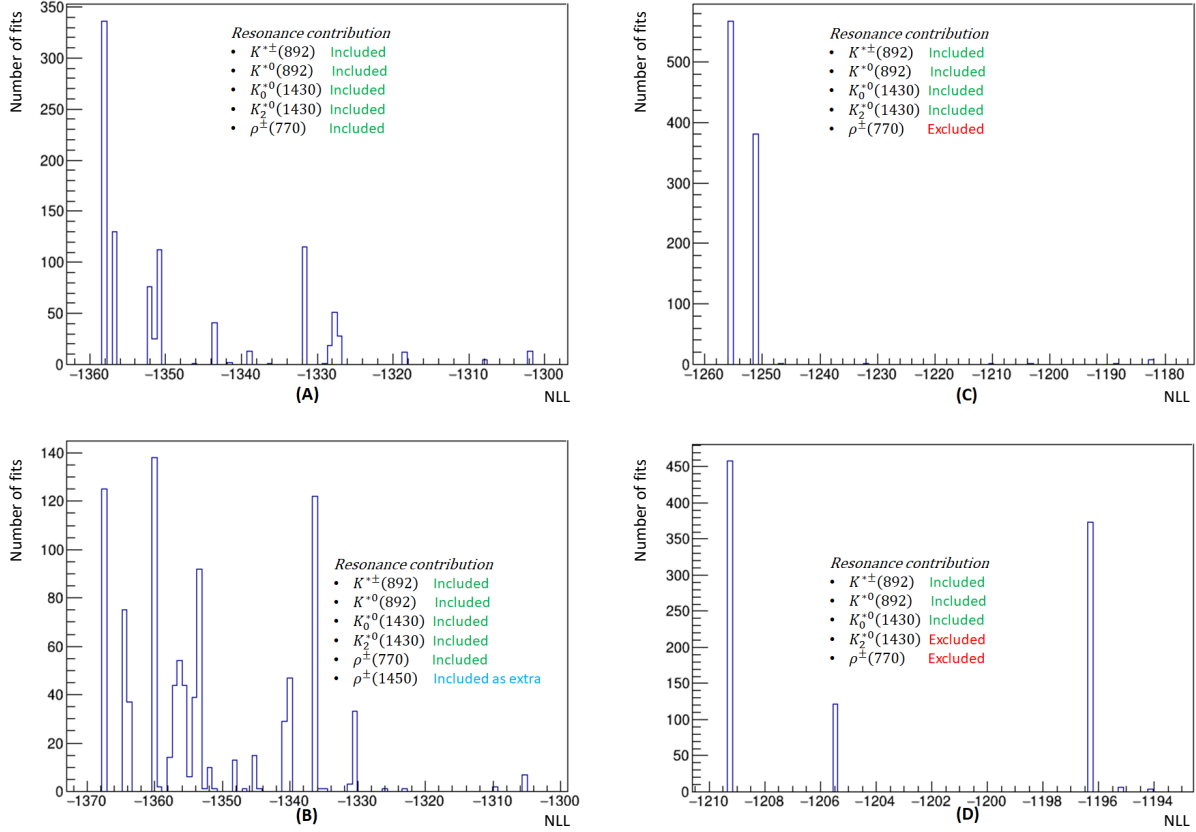


Figure 4.8: NLL distribution with include/exclude resonances. Excluded resonances show higher NLL values than included in (C) and (D). Extra included resonances in (B) do not make much difference compared to (A).

#### 4.4.2 Amplitude, Phase, FitFraction and Error study

Laura++ performs a maximum likelihood fit to the data or full MC as explained in Section 3.4.3. The likelihood function in Equation 3.11 is usually very complicated and has a large number of dimensions. The presence of secondary minima is very likely and is accounted for by running many fits with different, random initial values for the fit parameters. According to Figure 4.7 each NLL value has a corresponding amplitude, phase and fit fraction value. As an example Figure 4.9 shows the distribution of these variables according to the NLL plot for the  $K^{*0}(892)$  resonance.

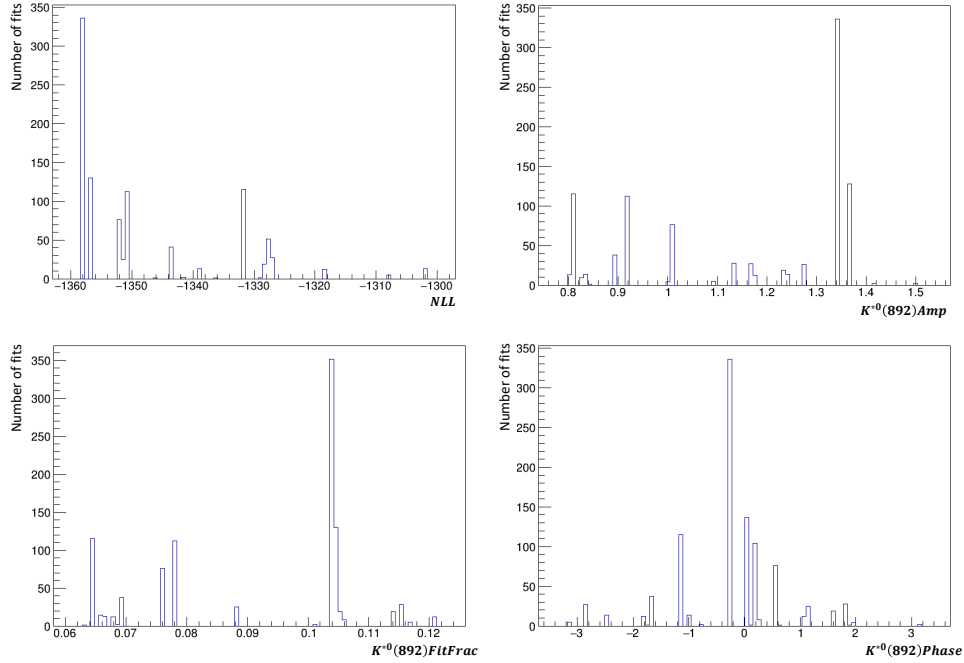


Figure 4.9: NLL distribution with different resonance contributions.

I can only measure the amplitudes and phases relative to other resonances as mentioned in Sections 3.4.3 and 4.4.1. To extract the best fit amplitude and phase values, I have to look at the highest peaks in the NLL distribution in Figure 4.7. After selecting a range of NLL,  $-1360 < NLL < -1354$  in this example, I look at the fit parameters of amplitude, phase and fit fraction. I also have the uncertainty parameters and other parameters such as individual and global correlation coefficients available from the fit. Using these extracted parameter values, I can re-generate toy MC using Laura++ and compare it with the full MC sample. If re-generated toy MC does not agree well with the full MC then I have to try another range of NLL such as  $-1354 < NLL < -1350$ . After going through this procedure the best fit parameter values I found are listed in Table 4.8.

Table 4.8: Fit parameter values after fitting full MC with Laura++.

Resonance	Amplitude	Phase	Fit Fraction
$K^{*+}(892)$	$1.3 \pm 0.0695$	$-1.831 \pm 0.1645$	$0.1774 \pm 0.02093$
$K^{*0}(892)$	$0.803 \pm 0.1034$	$-1.776 \pm 0.3235$	$0.06927 \pm 0.01691$
$K_0^{*0}(1430)$	$1.266 \pm 0.1729$	$0.3427 \pm 0.2073$	$0.1681 \pm 0.04329$
$K_2^{*0}(1430)$	$1.8789 \pm 0.1558$	$-1.391 \pm 0.2122$	$0.3797 \pm 0.04513$
$\rho^+(770)$	$1.4716 \pm 0.1269$	$-0.771 \pm 0.2459$	$0.2275 \pm 0.03306$
NR	1 (fixed)	0 (fixed)	$0.105 \pm 0.00853$

According to Table 4.8,  $K_2^{*0}(1430)$  has the highest amplitude and fit fraction value. Figure 3.21 shows the highest peak among the resonances. This means there is a higher chance for the  $B$  meson to decay via the channel of  $B^\pm \rightarrow K_2^{*0}(1430)\pi^\pm$  and  $K_2^{*0}(1430)\pi^\pm \rightarrow K_S^0\pi^\pm\pi^0$ . The fit fraction value is the most important parameter in this table because by using this fractional value, I can calculate the branching fraction (BF) of each resonance contribution. The fit fraction is a function of the amplitude and phase values. The uncertainty estimation of this fit fraction is done by generating Gaussian distributed random values between the upper and lower limits of the amplitudes and phase values similarly as in Section 4.2.1. Figure 4.10 shows an example fit fraction uncertainty distribution for the  $\rho^+(770)$  resonance contribution.

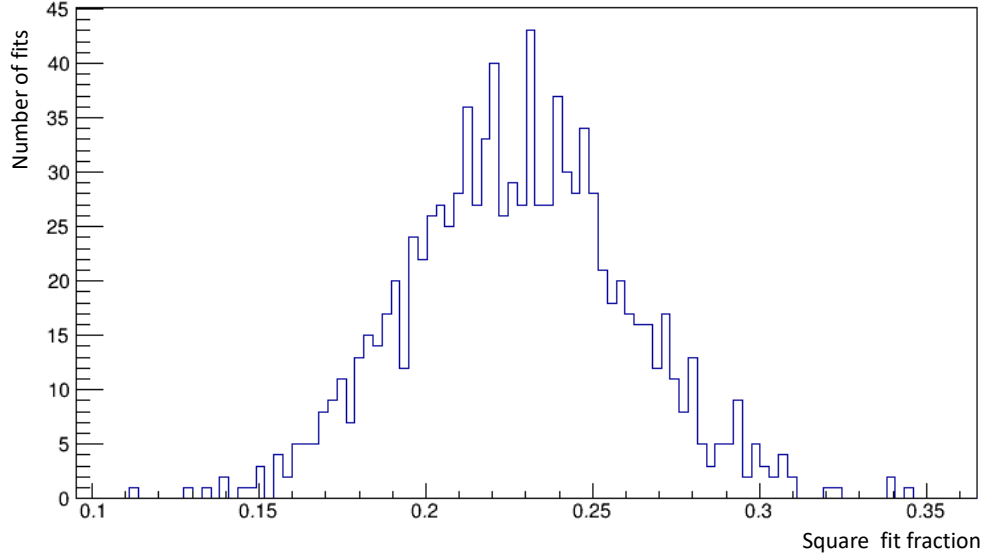


Figure 4.10: Square fit fraction distribution generated by using upper and lower limits of amplitude and phase parameters for  $\rho^+(770)$ .

Finally to validate these amplitude and phase values, it is important to re-generate events according to the extracted values. Therefore extracted amplitudes, phases and all input Dalitz maps in Section 4.4.1 are used to re-generate toy MC using Laura++ and compare with the initial full MC sample. Figure 4.11 shows a comparison of the generated toy MC and full MC samples. This plot includes toy MC signal, continuum, SCF and B-related contributions using different colours and cross lines showing full MC points with all types of backgrounds.

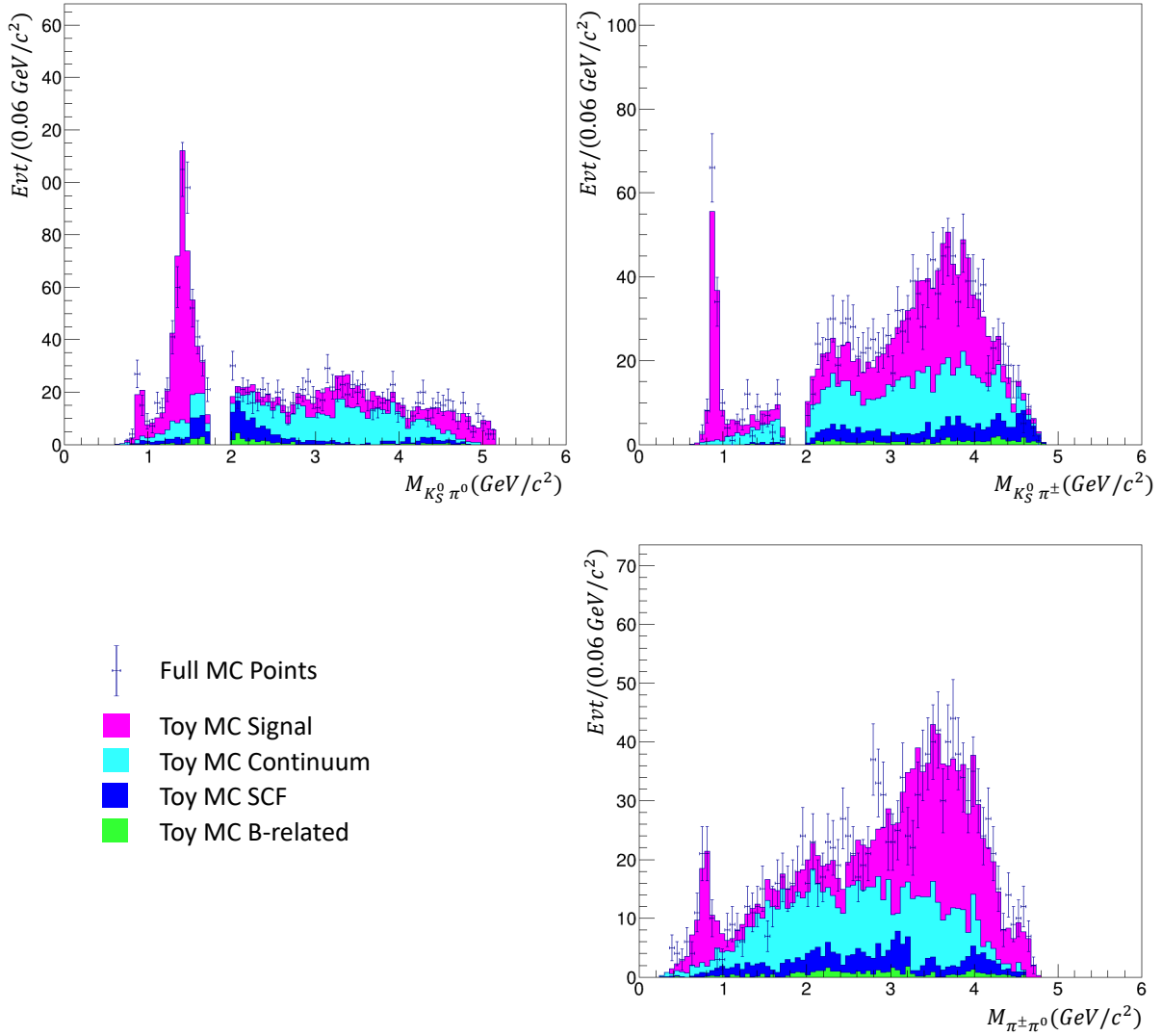


Figure 4.11: Stack plots of generated toy MC mass distribution compared with the full MC.

After calculating the BF for full MC, I use that value to calculate the BF for each intermediate resonance. For this calculation I take the fractional amount of these resonances as the fit fraction in Table 4.8. The final BF calculation for each resonance contribution are shown in Table 4.9.

Table 4.9: Branching fraction of each resonance contribution

Resonance	Fit Fraction	Branching Fraction ( $10^{-6}$ )
$K^{*+}(892)$	$0.1774 \pm 0.02093$	$8.554 \pm 2.829$
$K^{*0}(892)$	$0.06927 \pm 0.01691$	$3.340 \pm 1.315$
$K_0^{*0}(1430)$	$0.1681 \pm 0.04329$	$8.106 \pm 3.261$
$K_2^{*0}(1430)$	$0.3797 \pm 0.04513$	$17.830 \pm 5.923$
$\rho^+(770)$	$0.2275 \pm 0.03306$	$10.970 \pm 3.746$
Non-Resonance	$0.105 \pm 0.00853$	$5.063 \pm 1.618$

## CHAPTER 5 SUMMARY AND CONCLUSION

In this chapter I summarize my analysis of the  $B^\pm \rightarrow K_s^0 \pi^\pm \pi^0$  decay in the full MC and Belle data. I recap my selection criteria, data driven background estimation, estimating the signal yield, fit fraction in the Dalitz analysis and, branching fraction with uncertainty calculation.

### 5.1 Summary of Results

In the full MC signal and background events I used the selection procedure described previously to minimize and eliminate badly-reconstructed signal and background events to optimize the signal to background ratio. In Tables 4.1 and 4.2 I find in the full MC a signal to background ratio of to 1:3 given the assumed branching fraction. Table 5.1 summarizes the selection in full MC and data.

Table 5.1: Selection criteria summary of both full MC and data corresponding to 571  $fb^{-1}$  of luminosity

Variable (X)	Range	MC Signal Events	MC Background Events	Data Events
Candidate	$X = 0$	4110	8206368	4111983
Good $K_s^0$	$X = 1$	3040	1605868	908295
$M_{BC}$	$5.275 < X < 5.29$	1564	288234	151608
$\Delta E$	$-0.1 < X < 0.05$	980	39157	22998
ChiProb	$0.5 < X$	693	24236	13267
$M_{K_s^0}$	$0.49 < X < 0.51$	677	22375	12101
$E_{\pi^0}$	$0.7 < X$	503	16960	9225
BDT	$0.13 < X$	174	1603	660
$M_{K_s^0 \pi^+}$	$X < 1.70788$ or $1.9924 < X$	168	1549	647
$M_{K_s^0 \pi^0}$	$X < 1.70788$ or $1.9924 < X$	152	479	647

After applying the selection criteria I combine both generated full MC signal and background events to make a full MC sample corresponding to  $571 \text{ fb}^{-1}$  of integrated luminosity which matches the size of the data sample. To calculate the branching fraction, I extract the signal yield using various fitting methods. I use four different methods to estimate the number of background events in the signal region by fitting background and signal events using a combination of ARGUS and double GAUSS functions. Among these four methods, the last method, Method 4, shows the best agreement with the known number of background events. It does not rely on fitting the signal as well as the SCF events. Table 5.2 shows the final outcome of all the fitting methods summarized in Table 4.4.

Table 5.2: Summary of the number of events for full MC and data according to different fitting methods

Method	Input evts	Bkgnd evts	Bkgnd pct error	Signal evts	Signal pct error
Method 1	631	$511 \pm 49$	9.59%	$120 \pm 49$	40.83%
Method 2	631	$465 \pm 37$	7.95%	$166 \pm 37$	22.29%
Method 3	631	$438 \pm 35$	7.99%	$193 \pm 35$	18.13%
Method 4	631	$484 \pm 45$	9.29%	$147 \pm 45$	30.61%
Data	647	$514 \pm 49$	9.53%	$133 \pm 49$	36.84%

I calculate the branching fraction, MC efficiency, and uncertainties calculated according to Equations 3.2 and 4.2. The number of  $B\bar{B}$  events and its error is taken from [58]. Finally I calculate the full MC and data branching fraction using Equations 3.13 and 4.4 based on the background estimation method 4. Table 5.3 shows the summary of the branching fraction results based on Tables 4.5, 4.6, and 4.7. In this table it is clear the uncertainty on the branching fraction is dominated by the uncertainty on the signal yield.

Table 5.3: Summary of branching fraction for full MC and data

Source	Num of $B\bar{B}$ pair	Efficiency	Signal yield	BF ( $10^{-5}$ )
Full MC	$309810000 \pm 1.52\%$	$0.00984 \pm 3.1\%$	$147 \pm 30.61\%$	$4.822 \pm 30.8\%$
Data	$309810000 \pm 1.52\%$	$0.00984 \pm 3.1\%$	$133 \pm 36.84\%$	$4.363 \pm 37.0\%$

## 5.2 Comparison of Results with BaBar and PDG

A similar study was done by the *BABAR* collaboration in an unpublished result. *BABAR* was a detector built at the Stanford Linear Accelerator Center (SLAC) to study B mesons [59] [60]. Here I compare their study with my analysis and also with the Particle Data Group (PDG) [61] upper limits in Tables 5.4 and 5.5.

Table 5.4: Branching Fraction Comparison

Source	Branching Fraction ( $\mathcal{B} \times 10^{-6}$ )
Belle data	$43.63 \pm 16.1$
BABAR [62]	$45.90 \pm 2.6 \pm 3.0^{+8.6}_{-0.0}$
PDG	$< 66$ at 90% C.L.

Table 5.5: Intermediate resonance comparison

Decay Channel	Branching Fraction ( $\mathcal{B} \times 10^{-6}$ )		
	Belle full MC	BABAR	PDG
$K^{*+}(892) \pi^0$	$8.554 \pm 2.829$	$9.2 \pm 1.3 \pm 0.6_{-0.5}^{+0.3}$	$6.8 \pm 0.9$
$K^{*0}(892) \pi^+$	$3.340 \pm 1.315$	$14.6 \pm 2.4 \pm 1.4_{-0.4}^{+0.3}$	$10.1 \pm 0.8$
$K_0^{*0}(1430) \pi^+$	$8.106 \pm 3.261$	$50.0 \pm 4.8 \pm 6.1_{-2.6}^{+2.7}$	$39.0_{-5.0}^{+6.0}$
$K_0^{*+}(1430) \pi^0$	Unknown	$17.2 \pm 2.4 \pm 1.5_{-1.8}^{+0.0}$	$11.9_{-2.3}^{+2.0}$
$K_2^{*0}(1430) \pi^+$	$17.830 \pm 5.923$	Unknown	$5.6_{-1.5}^{+2.2}$
$\rho^+(770) K_S^0$	$10.970 \pm 3.746$	$9.4 \pm 1.6 \pm 1.1_{-2.6}^{+0.0}$	$7.3_{-1.2}^{+1.0}$
Non-Resonance	$5.063 \pm 1.618$	Unknown	Unknown

The BF value from the BABAR experiment in Table 5.4 is between what I used in the Belle full MC and the value I find in the Belle data. The uncertainty with the Belle data is higher than found by BABAR due to a smaller signal yield. The Belle data BF value is a  $2.71\sigma$  result, consistent with the PDG upper limit.

### 5.3 Conclusion and Discussion

Here I report my Dalitz plot analysis of the charmless three-body decay  $B^\pm \rightarrow K_S^0 \pi^\pm \pi^0$  using data at the  $\Upsilon(4S)$ . The full MC samples generated use EvtGen for the simulation of B meson decays and GSIM (GEANT3) for the simulation of the Belle detector. The reconstruction process of the generated full MC sample is done by the Belle II basf2 software. The signal selection criteria use  $M_{BC}$ ,  $\Delta E$ , mass of  $K_S^0$ , and others as described in Section 3.2 and my MVA analysis using TMVA in root removes large amount of continuum background.

After event selection I estimate backgrounds in the  $M_{BC}$  distribution with four methods using ARGUS function for background and a double GAUSSIAN function for signal. Among these methods, Method 4 is chosen to obtain background events in the signal region. Finally

I calculate the branching fraction in full MC using the signal *efficiency*, *number of  $B\bar{B}$  pairs*, and *signal yield*. I apply this entire procedure to the Belle data. The full MC calculated BF for  $B^\pm \rightarrow K_s^0 \pi^\pm \pi^0$  is  $\mathcal{B}(B^\pm \rightarrow K_s^0 \pi^\pm \pi^0) = (4.82 \pm 1.49) \times 10^{-5}$  and for data

$$\mathcal{B}(B^\pm \rightarrow K_s^0 \pi^\pm \pi^0) = (4.36 \pm 1.61) \times 10^{-5} \quad (5.1)$$

In this BF calculation, the uncertainty is dominated by the signal yield. According to Table 5.1 and Figure 4.5 I observe a small number of signal events. Therefore it is hard to extract signal yield using a signal fit. My approach here is simple and naive leading to a conservative result.

#### 5.4 Future analysis

For future analysis of this mode it is important to have higher integrated luminosity. This can be achieved with the Belle II experiment which plans to collect  $50 \text{ ab}^{-1}$  of luminosity. From my study of the signal full MC analysis, SCF events are problematic in the signal region. Mainly these SCF events are due to misidentified  $\pi^0$ s. One of the main differences between Belle and Belle II is a large reduction of material in front of the calorimeter, leading to cleaner and more efficient identification of  $\pi^0$ s.

In my background estimation, I need to reduce the uncertainty. There are multiple ways to calculate uncertainty using different fit functions with high statistics. All uncertainty calculations in this analysis are basically statistical. With the higher statistics in a Belle II analysis, systematic effects will be important to consider.

An unrealized goal of this analysis, from Section 1.4, is the search for charge and parity validation (CP) in this decay mode. This can be done using a measure of  $A_{CP}$  as in the Equation 1.11, comparing the  $B^+$  and  $B^-$  decays.

## 5.5 Super KEKB and Belle II detector

SuperKEKB, the upgrade of KEKB mentioned in Section 2.1, is the particle accelerator used for the Belle-II experiment. SuperKEKB features a 7  $GeV$  electron storage ring, the High Energy Ring (HER) and positron storage ring with an energy of 4  $GeV$ , the Low Energy Ring (LER). The energy of the electrons and positrons is asymmetric which helps to measure the B meson decay times via its flight distance from the measured collision point [63].

The Belle-II experiment will record data from SuperKEKB, which is projected to be the world's highest luminosity collider. Its instantaneous luminosity goal is 40 times that of KEKB. The increase in luminosity will be achieved by increasing the beam current and improved focusing of the beams at the interaction point. Belle-II contains several sub-detectors; a diagram is shown in Figure 5.1. Many parts are re-used from the Belle detector. There is a new vertex detector, new charged particle identification system Time of Propagation detector (iTOP) in the barrel, and an Aerogel RICH detector in the end caps. Also a new Central Drift Chamber (CDC) for charged particle tracking. Notably the new detector has better resolution of the Interaction Point(IP), improved  $K/\pi$  separation, and higher  $K_S$ ,  $\pi^0$  and slow Pion reconstruction efficiency as compared with Belle. Improved  $\pi^0$ s would be very helpful for my analysis. Data taking started in 2018 for Belle-II and the goal is to record an integrated luminosity of 50  $ab^{-1}$  [12].

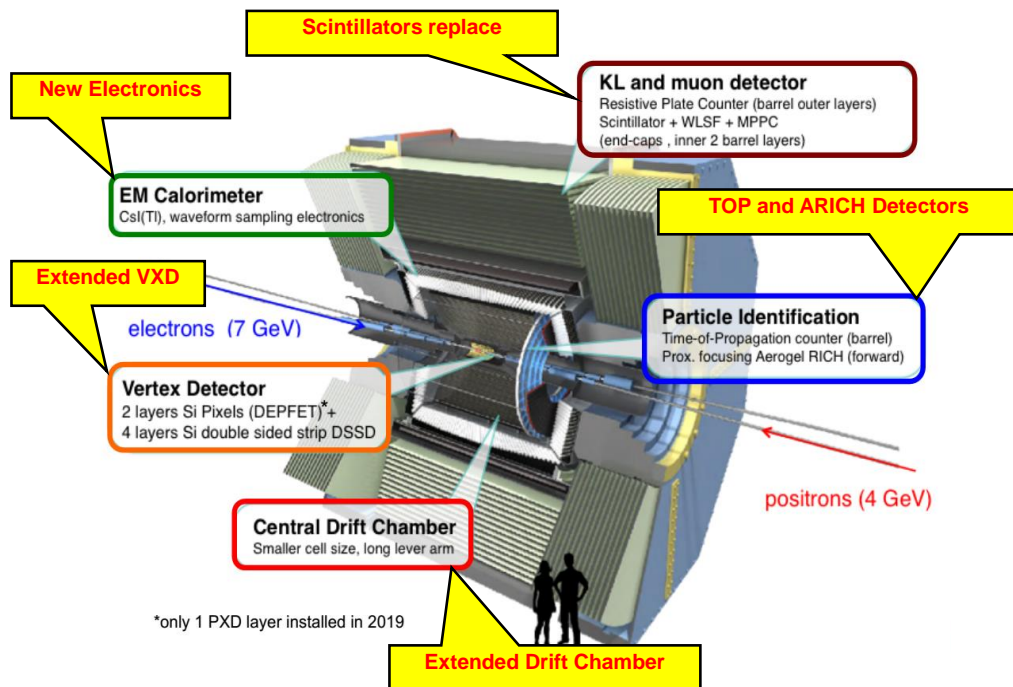


Figure 5.1: Belle II detector with new sub detectors [12]

**BIBLIOGRAPHY**

- [1] P. A. Zyla et al.(Particle Data Group). PDG particle physics. *Prog. Theor. Exp. Phys*, 083C01, 2020.
- [2] Sebastien Descotes Genon and Patrick Koppenburg. The CKM Parameters. *arXiv:1702.08834v4*.
- [3] O. Deschamps et al J. Charles. Current status of the Standard Model CKM fit and constraints on Delta F=2 New Physics. *Phys. Rev. D* 91, 073007, 2015.
- [4] Belle experiment observes a difference in direct CP-asymmetry between charged and neutral B meson decays. *High Energy Accelerator Research Organization (KEK), Press release*, March 21, 2008.
- [5] Brian Lindquist. Dalitz Plots. <https://www.slac.stanford.edu/slac/sass/talks/BrianL.pdf>, 2010.
- [6] [https://en.wikipedia.org/wiki/KEKB\\_accelerator](https://en.wikipedia.org/wiki/KEKB_accelerator). .
- [7] <https://www.belle2.org/research/detector/>. .
- [8] A. Abashian and et al Belle Collaboration. The Belle Detector. *Nuclear Instruments and Methods in Physics Research*, A 479:117–232, 2002.
- [9] I. Adachi et al T. Iijima. Aerogel Cherenkov counter for the BELLE detector. *Nuclear Instruments and Methods in Physics Research*, A 453:321–325, 2000.
- [10] A. Abashian et al (Belle Collaboration). . *Nuclear Instruments and Methods in Physics Research*, A 479:117–232, 2002.
- [11] D.R. Tovey (Sheffield) D. Miller (Glasgow). 47. Kinematics. 2000.
- [12] T. Abe et al. (Belle Collaboration). Belle II Technical Design Report. 2010.
- [13] [http://bweb3.cc.kek.jp/index\\_m.php](http://bweb3.cc.kek.jp/index_m.php). .
- [14] Emily P. Wang. Rutherford scattering of alpha particles. 2004.

- [15] Jean-Philippe Uzan. The Big Bang Theory: Construction, Evolution and Status. *Seminaire Poincare*, 2015.
- [16] Griffiths David. Introduction to elementary particles. ISBN 0-471-60386-4, 1987.
- [17] <https://en.wikipedia.org/wiki/Proton>. .
- [18] Peter W. Higgs. Broken symmetries and the masses of gauge bosons. *American Physical Society*, 1964.
- [19] A. D. Sakharov. *Pisma Zh. Eksp. Teor. Fiz*, 5:32, 1967.
- [20] <http://hyperphysics.phy-astr.gsu.edu/hbase/Particles/cpt.html>.
- [21] C.S. Wu , E. Ambler et al. *Phys. Rev.*,105:1413, 1414, 1957.
- [22] Anca Tureanu. Cpt and lorentz invariance: Their relation and violation. *Journal of Physics*, 2013.
- [23] Christenson and J. H. et al. *Phys. Rev. Lett.*,13:138, 140, 1964.
- [24] B Aubert et al. (B A B A R Collaboration). *Phys. Rev. Lett.*, 87:091801, 2001.
- [25] N. Cabibbo. . *Phys. Rev. Lett.*, 10:531, 1963.
- [26] G et al Dattoli. Ckm matrix exponential parametrization and euler angles. *Nuovo Cimento. A*, pages 487–496, 1997.
- [27] Y. H et al Ahn. Wolfenstein parametrization at higher order: Seeming discrepancies and their resolution. *arXiv:1106.0935*, 2018.
- [28] <https://en.wikipedia.org/wiki/Cabibbo>.
- [29] James G. Smith Hai-Yang Cheng. Charmless Hadronic B Meson Decays. *arXiv:0901.4396v1*, 2009.
- [30] Tim Gershon (LHCb Collaboration). Introduction to Dalitz Plot Analysis. <https://warwick.ac.uk/fac/sci/physics/staff/academic/gershon/talks/gershon-BadHonnef.pdf>, 2011.

- [31] <https://belle.kek.jp/>. .
- [32] S. Kurokawa and E. Kikutani. . *Nucl. Instrum Methods Phys. Res., Sect. A* 499, 1, (2003).
- [33] <https://www.kek.jp/en/Facility/ACCL/ElectronPositronLinac/>. .
- [34] <https://www.kek.jp/en/Facility/ACCL/KEKBRing/>.
- [35] <https://www.kek.jp/en/Facility/ACCL/KEKBRing/>. .
- [36] M. Tanabashi et al. (Particle Data Group). . *Phys. Rev, D* 98, 030001, 2018.
- [37] Y. Makida et al. Development of a superconducting solenoid magnet system for the B-Factory detector (BELLE). *Advances in Cryogenic Engineering*, 43, 1998.
- [38] KEK accelerator group. KEKB B factory design report. *KEK Report*, 95:7, 1995.
- [39] Soh Yamagata Suzuki et al. The BELLE DAQ system. *Nuclear Instruments and Methods in Physics Research, A* 453:440–444, 2000.
- [40] Y. Ushiroda et al. *Nucl. Instrum. Meth.* A438:460, 1999.
- [41] M. Tanaka et al. A control and readout system for the BELLE silicon vertex detector. *Nucl. Instr. and Meth*, A432:422, 1999.
- [42] R. Itoh. Computer farm for KEK B-factory. *Proceedings of the International Conference on Computing in High Energy Physics*, page 475, 1992.
- [43] D. J. Lange. . *Nucl. Instrum. Methods Phys. Res., A* 462:152, 2001.
- [44] T. Sjostrand. High-energy physics event generation with PYTHIA 5.7 and JETSET 7.4. *Comput. Phys. Commun*, 82:74–90, 1994.
- [45] Jolanta Brodzicka et al. (Belle Collaboration). Physics achievements from the Belle experiment. *PTEP*, Prog. Theor. Exp. Phys. 2012, 04D001:110, 2012.
- [46] [http://bweb3.cc.kek.jp](http://bweb3.cc.kek.jp/). .
- [47] *Nucl. Instrum D. J. Lange.* . *Methods Phys. Res., Sect, A* 462:152, 2001.

- [48] T. Sjostrand. High-energy physics event generation with PYTHIA 5.7 and JETSET 7.4. *Comput. Phys. Commun.*, 82:74–90, 1994.
- [49] I. Adachi et al. sBelle Design Study Report. *KEK Report*, 2008.
- [50] <https://confluence.desy.de/display/BI/Physics+NtupleTool>. Belle II internal wiki: Physics NtupleTool. 2017.
- [51] <https://b2master.belle2.org/software/development/sphinx/analysis/doc/Variables.html>. Belle II software home page.
- [52] C. Patrignani and Particle Data Group. Review of Particle Physics. *Chin. Phys.*, C40:100001, 2016.
- [53] R. Brun and F. Rademakers. ROOT: An object oriented data analysis framework. *Nucl. Instrum. Meth.*, A389:81–86, 1997.
- [54] Ji Zhu Hai-Jun Yang, Byron P. Roe. Studies of Boosted Decision Trees for MiniBooNE Particle Identification. 2005.
- [55] <https://en.wikipedia.org/wiki/ARGUSdistribution>.
- [56] Matthew Barrett. Dalitz Plot Analysis of the Charmless Threebody Decay Utilising Data Recorded by the BABAR Experiment. 2006.
- [57] Thomas Latham et al. Laura a Dalitz plot fitter. *arXiv:1711.09854v4[hep-ex]*, 2018.
- [58] <https://belle.kek.jp/secured/nbb/nbb.html>. .
- [59] <https://www6.slac.stanford.edu/>.
- [60] Others(The BaBar Collaboration) B. Aubert. The BABAR detector. *Nuclear Instruments and Methods in Physics Research Section A*, 479:1–116, 2002.
- [61] <https://pdg.lbl.gov/>.
- [62] Others(The BaBar Collaboration) J. P. Lees. Evidence for CP violation in  $B^+ \rightarrow K^*(892)^+\pi^0$  from a Dalitz plot analysis of  $B^+ \rightarrow K_S^0\pi^+\pi^0$  decays. *Phys. Rev. D* 96, 072001, 2015.

- [63] Th. Mannel A. J. Bevan, B. Golob. The Physics of the B Factories. *Eur. Phys.*, C74:3026, 2014.

**ABSTRACT****Study of the Decay  $B^\pm \rightarrow K_s^0 \pi^\pm \pi^0$  at the Belle Experiment**

by

**Suravinda Kospalage****May 2022****Advisor:** Prof. David Cinabro**Major:** Physics**Degree:** Doctor of Philosophy

Belle is a particle physics experiment based at the KEK laboratory in Tsukuba Japan which ran from 1999 to 2010 and collected  $1ab^{-1}$  of data. The Belle experiment is focused on studying the properties of particles called  $B$  mesons which are produced by accelerating and colliding electron and positron beams. These  $B$  mesons show the biggest differences between the properties of matter and anti-matter of any known particles. One of the main goals of the Belle experiments is to understand the differences between matter and anti-matter, specifically violations of charge-parity symmetry (CP violation) and how anti-matter vanished and we come to live in a matter dominated universe.

In this dissertation, I explore the charmless  $B$  decay  $B^\pm \rightarrow K_s^0 \pi^\pm \pi^0$  with the Belle full Monte-Carlo (full MC) simulation and Belle data corresponding to  $571fb^{-1}$  of luminosity and measure the decay's branching fraction(BF). Charmless transitions can proceed by a  $b \rightarrow u$  transition via a tree level diagram or  $b \rightarrow s$  or  $d$  transition via the so-called penguin diagram. Both decay types are highly suppressed compared to the  $b \rightarrow c$  transition and we expect a small branching fraction, smaller than  $10^{-5}$ . Penguin processes are important in  $B$ -meson charmless decays, thus it is possible to have contributions of unknown particles in the loop process leading to CP-violation contribution from Beyond Standard Model. Charmless  $B$  decays are sensitive to the angle  $\gamma$  (aka  $\phi_3$ ) in the unitary triangle and open a new window

to analyze the CP violation process.

I use the innovative Belle II software (basf2) for the initial reconstruction process. The challenge in observing the  $B^\pm \rightarrow K_s^0 \pi^\pm \pi^0$  decay is to suppress backgrounds from continuum events, which do not contain  $b$  quarks, and background from other  $B$  meson decays. I use direct selections such as beam-energy constrained mass ( $M_{bc}$ ), energy difference ( $\Delta E$ ), probability of the vertex fit result (ChiProb), and others, on several variables to remove background from  $B^\pm \rightarrow K_s^0 \pi^\pm \pi^0$  events. I find such an approach is insufficient. I found it was necessary to use a multi-variate analysis (MVA) machine learning/artificial intelligence technique called a boosted decision tree (BDT) to reduce the backgrounds to the level to allow me to clearly observe the decay and measure the BF. I compare my results with unpublished results from the BaBar experiment.

Additionally I use the Dalitz plot (DP) technique to study the intermediate resonance contributions in this decay. I use the Laura++ software to generate and fit toy Monte Carlo(toy MC), full Monte Carlo simulated data, and, based on the techniques developed on these simulations, the experimental data to study the resonance sub-structure of this decay.

## AUTOBIOGRAPHICAL STATEMENT

**Name:** Suravinda Kospalage

**Education:**

M.Sc. Physics, Wayne state University, Detroit, Michigan, USA, 2018

BSc. Physics, University of Kelaniya, Kelaniya, Srilanka, 2014

**Professional Experience:**

Teaching Assistant, Wayne State University, Dept. of Physics and Astronomy, Detroit, MI, 2021-Current

Research Assistant, Wayne State University, Dept. of Physics and Astronomy, Detroit, MI, 2020-2021

Research Assistant, High Energy Accelerator Research Organization, Tsukuba, Japan, 2019-2020

Research Assistant, Wayne State University, Dept. of Physics and Astronomy, Detroit, MI, 2016-2019

Teaching Assistant, Wayne State University, Dept. of Physics and Astronomy, Detroit, MI, 2015-2016

Teaching Assistant, University of Kelaniya, Dept. of Astronomy and Physics, Kelaniya, Srilanka, 2014-2015

**Publications:**

A. Abdesselam et al. [Belle Collaboration], “Search for the Decay  $B_S^0 \rightarrow \eta' \eta$ ”, arXiv:2009.06052 [hep-ex]

F. Abudinén et al. [Belle-II Collaboration], “Measurement of Hadronic Mass Moments  $M_n^X$  in  $B \rightarrow X_C l \nu$  Decays at Belle II”, arXiv:2009.04493 [hep-ex]

J. Yelton et al. [Belle Collaboration], “Study of Electromagnetic Decays of Orbitally Excited  $\Xi_C$  Baryons”, arXiv:2009.03951 [hep-ex]

INSPIRE: K.Kumara